南大洋の上層における季節変動と力学

Doctoral Dissertation

SEASONAL VARIATION AND GOVERNING DYNAMICS OF THE UPPER LAYER IN THE SOUTHERN OCEAN

September 2022

Graduate School of Marine Science and Technology
Tokyo University of Marine Science and Technology
Doctoral Course of Applied Marine Environmental Studies

FERREIRA AZEVEDO MATHEUS

Doctoral Dissertation

SEASONAL VARIATION AND GOVERNING DYNAMICS OF THE UPPER LAYER IN THE SOUTHERN OCEAN

September 2022

Graduate School of Marine Science and Technology
Tokyo University of Marine Science and Technology
Doctoral Course of Applied Marine Environmental Studies

FERREIRA AZEVEDO MATHEUS

Table of Contents

List of figures

Chapter 1:

Chapter 2:

Chapter 3:

Chapter 4:

Chapter 5:

Special Thanks

I would like to show my gratitude to my supervisor, Kitade Yujiro, for his support, enthusiasm, and guidance during the entire period of my PhD. I'm glad to have you as a mentor and feel I learned a lot not only as a scientist but also as a human being. The quality of the thesis was severely improved with the assistance of Assistant Professor and co-advisor Dr. Mizobata and co-advisor Dr.Nagai, which raised important questions, suggested methodology and engaged in enthusiastic discussion. Professor Aoki, from Hokkaido University was also fundamental to this work, directly advising chapter 2, co-authoring the related publication, and handling the deployment and recovery of the mooring, together with the crew of R/V Umitakamaru.

I dedicate this work to my family, especially my loving wife, Ana, and my brother Vinicius. Their constant support was for me a lighthouse during the dark sleepless nights I so often spent in the laboratory. The good friends I made through this journey helped tremendously in facing the challenges of starting life in a new country. I thank my labmates Kazuho, Shintaro and Minami for their cheerfulness and making me feel welcome in Japan.

I sincerely thank all the colleagues, professors, and curious souls which exceeded their role and became precious friends. If there is any merit to be had in this work, it is also yours to share. Finally, I thank whoever is reading this thesis, and I hope whatever it is you seek, these pages are of use to you.

Chapter 1: Introduction

1.1 On the importance of studying the Southern Ocean

The Southern Ocean is of global significance in the sense that it is in this region that waters from all major oceans converge through the Antarctic Circumpolar Current (ACC), which flows eastward without being ever bounded by land, forming the world's strongest current system. It is in this region where, induced by the easterly winds, upwelling occurs in considerable scale, causing the deep and intermediate water masses formed northward to emerge and oxygenate. On the other hand, new water masses are formed, rich in nutrients, which sink in processes unique to the South pole: At the Antarctic Convergence, the Antarctic Intermediate water sinks to a thousand meters deep, led by its, cold, dense properties, even though it is relatively fresh (34.2-34.4 psu). Closer to the continent, in the polynyas, the Antarctic Bottom Water (AABW) is formed, and flows at the bottom of all ocean basins until upwelling again at the Equator. It is by these water masses that the Southern Ocean connects the world's ocean to form a global system of currents that transfers heat and CO_2 from the atmosphere to the deep ocean, and according to Kennicutt et al. (2014), the nutrients carried north by this system support the base of the ocean's food web. However, as the ocean is becoming more acidic, cold southern waters are estimated to be the first to exhibit the impacts.

When writing on the importance of the Southern Ocean, it is imperative to talk about its role on the deep circulation pattern known as the Meridional Overturning Circulation (MOC). In it, surface currents transport hot and light water towards high latitudes, then these waters are cooled in regions of deepwater formation regions and sink. The cycle is completed by deep currents inducing transport towards the equator, where upwelling processes close the cycle. The Southern Ocean has a

pivotal role in this process as not only the upwelling caused by the westerly circumpolar winds induce northward Ekman transport near the surface, being seen as a major engine of the AMOC (Toggweiler and Samuels, 1993, 1995, 1998), but the formation of AABW is also seen as the major forcing of the thermohaline circulation responsible for the abyssal overturning cell.

Meanwhile, Munk and Wunsch (1998) have argued that without deep mixing, in the span of a few thousand years the ocean would become, with the exception of the equatorial zone, homogeneous, cold and salty. Although some of the assumptions and estimations were made from the Sandstrom Theorem that differential heating and cooling cannot drive a sustained circulation when the source of heating is at or above the level of the cooling source, theory recently put in check by Coman et al. (2006) and Kuhlbrodt (2008), the general aspect still holds and is considered qualitatively right. To get into detail, Sandstrom did not consider diffusivity driven circulation patterns. Molecular diffusivity is known to warm the fluid at high pressure and cool it down at low pressure; therefore, the heating experienced by a stratified fluid will always happen at a higher pressure than the total cooling due to diabatic molecular/turbulent diffusion. However, such diffusivity driven circulations imply in the transport of light water downwards and heavy water upwards, increasing potential energy and therefore requiring an external source of energy. Therefore, Sandstrom's theorem and its main inference appear to be at least qualitatively correct in observing the energy requirements of the MOC. In fact, the mixing rates in most of the ocean seem to be one order of magnitude too small to sustain the overturning circulation (Ledwell et al., 1998). And other sources of diapycnal mixing, such as the breaking of internal waves are necessary (Nikurashin and Ferrari, 2013).

1.2 Why is studying upper layer convection in the Southern Ocean necessary?

In most of the ocean, the strong vertical density gradients of the thermocline inhibit the vertical exchange between the upper and deep layers. At high latitudes, however, the weak stratification and exposure during winter to buoyancy loss to the atmosphere generates deep-reaching convection columns (Clarke and Gascard 1983, Cheon et al. 2014). These convective cells push surface waters downward, effectively enhancing communication between the upper and deep layers of the high latitude oceans, driving homogeneization and creating a deep mixed layer (Marshall and Schott 1999).

The mixed layer (also referred to here as a mixed patch) plays a role in modulating the properties of dense overflows in the Southern Ocean and therefore the downwelling branch of the global meridional overturning circulation (MOC), including the Atlantic meridional overturning circulation (AMOC) (Talley 1999; Danabasoglu et al. 2012). The AMOC has widespread consequences on the global climate, such as modulating global ocean heat content (Kostov et al. 2014), global marine biological activity (Schmittner, 2005) and carbon uptake (Sallée et al. 2012). Therefore, open-ocean convection (and the deep mixed layer that forms because of the process) plays a major role in regulating the global climate (Sohail et al., 2020).

Two aspects make ocean convection interesting from a theoretical point of view. First, the timescales of the convective process in the ocean are sufficiently long that it may be modified by the Earth's rotation; second, the convective process is localized in space so that vertical buoyancy transfer by upright convection can give way to slantwise transfer by baroclinic instability. Laboratory and numerical studies such as Jones and Marshall (1993) and Maxworthy and Narimousa (1992) of

rotating convection motivated by the oceanographic problem have led to advances in our understanding of the general problem.

However, despite the importance of upper layer convection in the surface-deep interactions, most ocean general circulation models (OGCMs) parametrize convection by adjustment schemes (Rahmstorf, 1993; Klinger et al., 1996). These schemes remove static instability in the water column at each time step by mixing vertically adjacent grid cells. However, the mixed layer response to daily-averaged fluxes is not necessarily the same as the average response to the diurnal cycle. Neglecting the diurnal cycle replaces periodic nightly convective pulses with chronic mixing that does not reach as deep. (Soloviev and Klinger, 2008).

It is therefore, imperative to study the effects of convection in the Southern Ocean's mixed layer in order to properly understand, reproduce and forecast the interaction between the oceanic surface and the deeper layers. This interaction might be one of the key missing factors to understand how atmospheric-forced climate change might interact with the deep and bottom water masses which regulate the global ecosystem.

1.3 General characteristics of the Southern Ocean

The horizontal boundaries of the Southern Ocean are not well defined. A geo-political definition of the Southern Oceans' northern limit is given by the Antarctic Treaty (United Nations, 1959) as 60°S, but there is little physical meaning to this boundary. The ACC extends up to 38°S (Orsi et al., 1995, Figure 1.1) but the influence of Southern Ocean phenomena extends up to the Subtropical Front (Talley, 2011).

Assuming uniform mixing, Munk (1966) used an advective and diffusive model of heat transfer to estimate that the scalar diffusivity of density $\mathrm{K}_\rho = 10^{-4}$ m^2 s^{-1} was required to close the global meridional overturning circulation. This value became the canonical value for diffusivity in the ocean interior. However, empirical observations done by releasing tracers in the water (Ledwell et al. 1993, 1998) and by microstructure profilers such as Gregg (1988) found values of K_ρ one order of magnitude lower than what Munk's model predicted.

Additional Studies have shown a strong spatial and temporal diffusivity variability (Naveira Garabato et al., 2004; Sloyan 2005, among many others). Notably, Meyer et al. (2015) found diffusivity values for the Southern Ocean ranging from $O(10^{-6})$ to $O(10^{-3})$ m^2s^{-1}, and especially high values were attributed to the frontal regions of the ACC and to the dissipation of internal waves due to the interaction between the ACC and the bottom topography of the Kerguelen Plateau. A general characterization scheme is given by Figure 1.2. Providing important background to this thesis, Waterman et al. (2013) uses the same dataset to complement this relation by finding evidence of enhanced turbulent dissipation and mixing associated with downward-propagating near-inertial internal waves (NIW) in the upper 1.5 km of the water column, and postulates that turbulent dissipation in the ocean interior is associated with breaking internal waves. A depth-integrated dissipation rate of O(1-10) mW^{-2} for this upper layer was calculated, coinciding with the estimates of energy flux from the wind to near-inertial motion in the region (Alford 2001, 2003). Generally, turbulent dissipation in the ocean interior appears to be underpinned by breaking internal waves, as evidenced by the correspondence of spatial patterns of dissipation and internal wave energy.

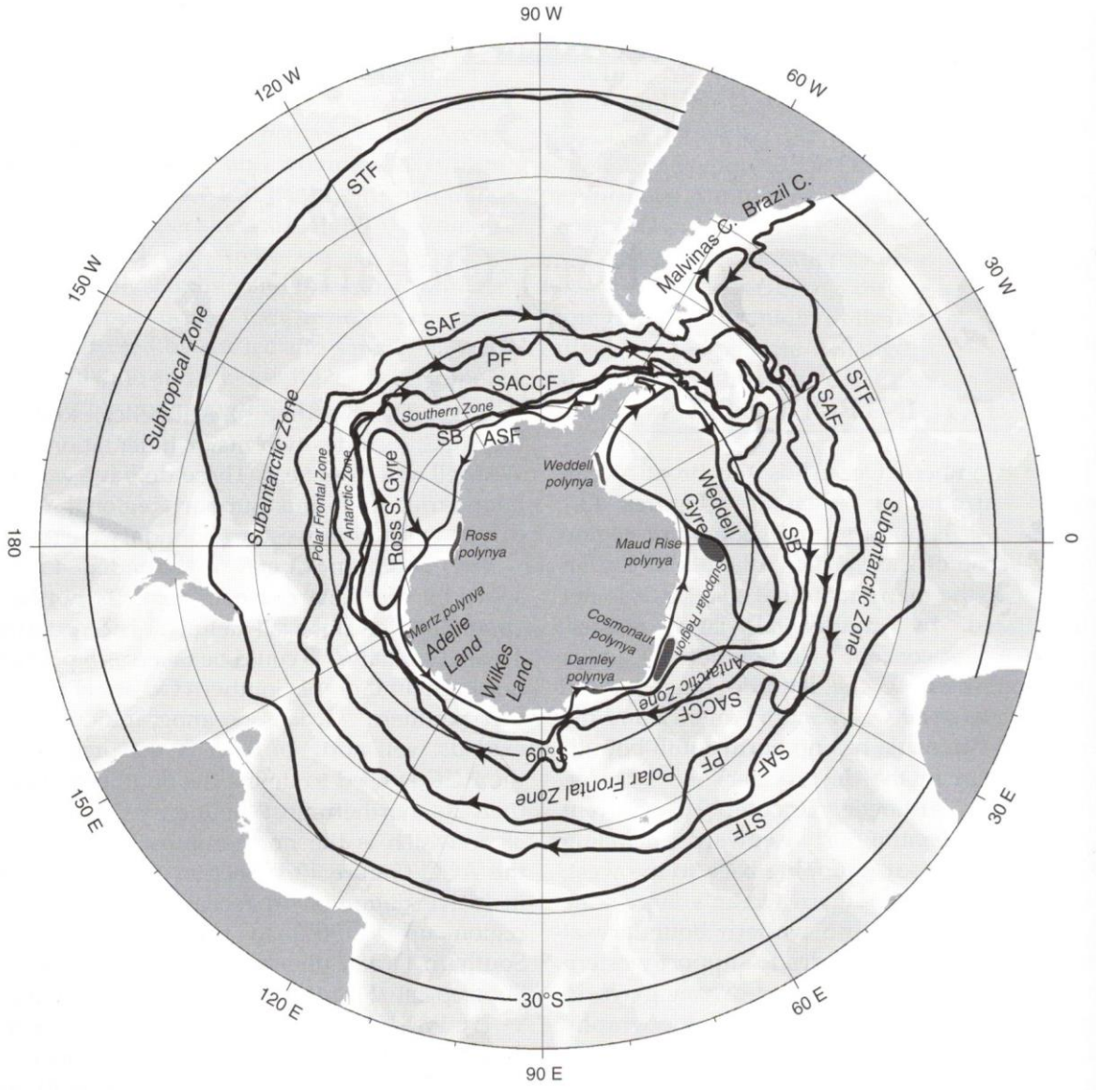

Figure 1.1. Southern Ocean principal features. Fronts and the largest gyres are given by black lines and arrows, while the biggest polynyas are indicated by dark patches. The extension of the fronts is taken from Orsi et al. (1995). Figure adapted from Talley (2011).

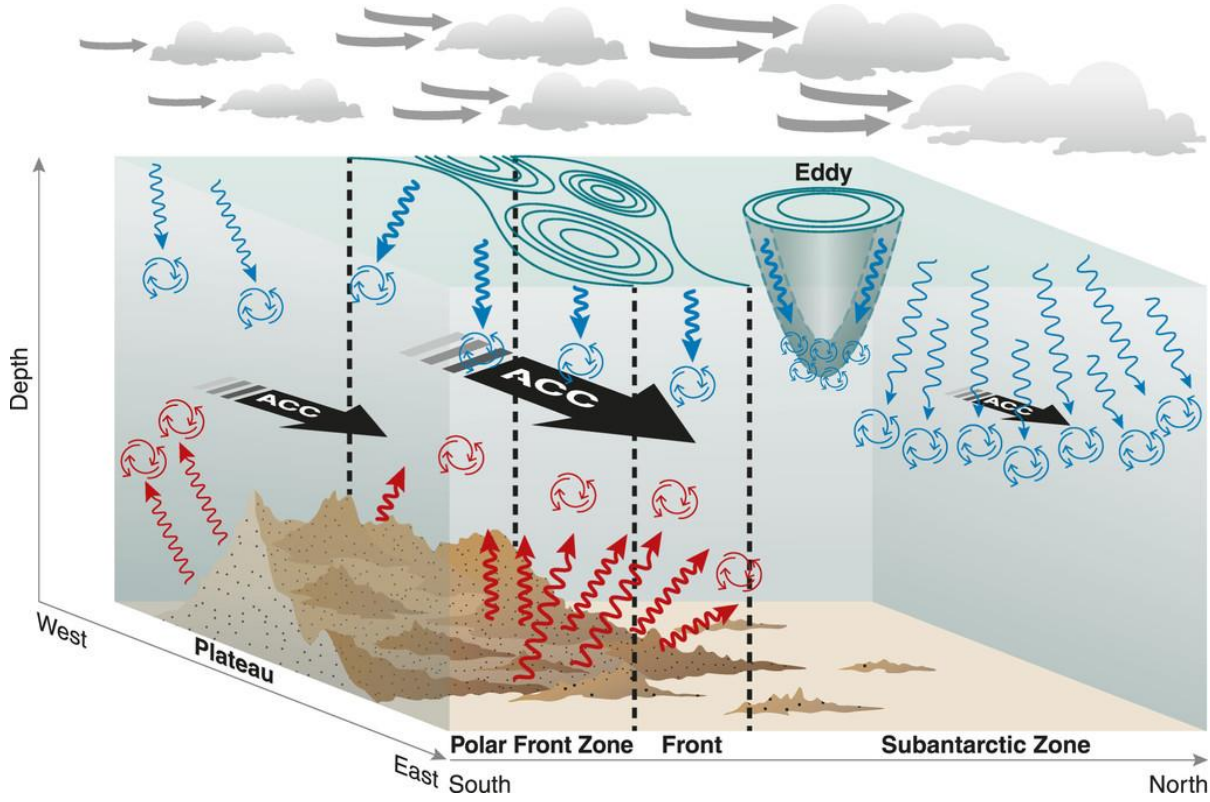

Figure 1.2. Meyer et al. (2015) schematic of the spatial distribution of internal waves, mixing and associated processes north of the Kerguelen Plateau. Two regions can be observed: South of the Subantarctic Front (SAF) the mixing is seen to be controlled by topographic roughness generating upward-propagating internal waves (red arrows). North of the SAF stronger wind forcing generates downward propagating NIWs (blue arrows). Mesoscale eddy activity was also observed north of the SAF region.

1.4 Aims of the thesis and questions addressed

With this thesis, we aim to elucidate the dynamics pertaining to the Southern Ocean's upper layer and investigate if and in which way energy might be transported downwards from the mixed layer. The thesis has 3 result chapters which intend to answer the following questions:

- What are the main patterns of upper layer variability in the Indian sector of the Southern Ocean?
- How deep does the local surface variability reach?
- What are the main drivers of upper layer variability in the Indian sector of the Southern Ocean?
- In which manner is the Southern Ocean's upper layer energy distributed in frequency space?
- In what way do the different forcing mechanisms of the upper layer interact with each other?
- Can this interaction be reproduced?

1.5 Thesis Outline

Some of the results presented in this thesis were published or are in review in scientific journals. Therefore, the thesis is structured in a brief review of internal wave theory, in Chapter 2, and independent chapters addressing the questions raised in subsection 1.4.

In Chapter 3, we aim for the characterization of the mixed layer in terms of its physical properties, seasonal variabilities, and dynamics through data obtained from

a mooring deployed during the year of 2012 at 60 °S, 140 °E, in the Indian sector of the Southern Ocean. Besides description, a box model was employed to visualize from the estimated bulk diffusivity of temperature, salinity, and density, how far does local surface variability penetrate downward and how much of the seasonal patterns at each layer are explained by it.

In Chapter 4, we investigate the mechanisms behind the phenomena observed in Chapter 3 by exploring non-linear theory, spectral analysis, and statistic tools. An analytic wavelet function is built and employed in a continuous wavelet analysis to analyze current velocity data in its time-frequency variability. A damped slab model is also employed to study how much of the near-inertial signal can be reproduced by wind forcing alone.

In Chapter 5, validation of our previous hypothesis and conclusions is done by building a 2-D non-hydrostatic numerical model and reproducing a simplified version of the ocean surface cooling mechanism. The phenomenon observed in Chapter 4 is reproduced and the transport of energy is quantified both in terms of its vertical distribution, frequency representation and propagation from the area of forcing.

At last, in Chapter 6 a summary of the main results is provided. Besides the summary, method limitation as well as recommendations for future studies and concluding remarks are included.

Chapter 2: A short revision on internal wave theory

As internal waves (IWs) are central to the understanding of this thesis, a short explanation of the background theory is provided below, largely following the didactics of Sutherland (2005).

Internal waves are a special class of waves which propagate on the interface of fluids of different density. They are diverse in both space and period, with the movement scale ranging from a couple meters to thousands of kilometers, and the period varies between minutes to weeks. Like surface waves, IWs have gravity and buoyancy as restoring forces, however, while surface haves are confined to the sea-air interface IWs propagate both horizontally and vertically (Sutherland, 2005).

The starting point for describing the motion of internal waves is the Navier-Stokes equations:

$$\rho_T \frac{DV}{Dt} = -\nabla p_t + \rho_T g + F_{rot} + \mu \nabla^2 V, \tag{2.1}$$

where ρ_T is the fluid density in Kg m^{-3}, ***V*** = *(u,v,w)* denotes the west-east(u), south-north(v) and vertical (w) components of velocity (m s^{-1}) which correspond to the $\hat{x}$, $\hat{y}$ and $\hat{z}$ axis respectively. The pressure is given by p_t (Pa) and *g = -g* ***ẑ*** denotes the gravity acceleration (m s^{-2}). μ indicates the molecular viscosity of the fluid (m^2 s^{-1}) and F_{rot} indicates the external forces derived from the rotation of the background flow such as the Coriolis force.

For oceanic motion it is reasonable to assume the fluid incompressible so $\frac{D\rho_T}{Dt} = 0$, which implies the total divergence of the fluid parcel to be also zero: $\nabla \cdot V = 0$.

Equation 2.1 can be further simplified by Reynolds decomposing the pressure and density fields in a background field $\bar{p}$ (z) and $\bar{\rho}$ (z) and a perturbation field $p(\boldsymbol{x}, t), \rho(\boldsymbol{x}, t)$ and then assuming the background field to be in hydrostatic equilibrium, That is:

$$\frac{d\bar{p}}{dz} = -\bar{\rho} g, \tag{2.2}$$

in these equations the material derivative (Equation 2.3) introduces non-linearity on the advective term, the second term on the right side of the equation:

$$\frac{D}{Dt} = \frac{\partial}{\partial t} + V \cdot \nabla, \tag{2.3}$$

more approximations can be done depending on the type of movement we're studying: If we assume the flux to be hydrostatic, then $\partial \mathrm{p} / \partial \mathrm{z} = -\rho \mathrm{g}$, further simplifying Equation 2.1. Internal waves are hydrostatic if their frequency of propagation is significantly smaller than than the "natural" oscillation frequency of a stratified fluid, N. Waves with frequency closer to N are said to be non-hydrostatic.

If a Boussinesq flow is assumed, variations of density are considered significant only when they are in the buoyancy terms, that is, when multiplied by the gravity g. Thus, $\rho_T = \rho_0$, which being a constant can be taken out of the derivatives of Equation 2.1. The Boussinesq approximation is valid for most types of oceanic flows since the variation of density with depth is too small when compared to its absolute value, varying less than 10% from surface to bottom (Sutherland, 2005).

A useful approximation for the study of atmospheric waves is to consider the flux anelastic, which means approximating $\rho_T \rightarrow \bar{\rho}$. This is a useful approximation for the cases where the wave amplitude increases with height due to the significant decrease of the fluid density (i.e.: from the troposphere to the upper layers of the atmosphere).

Finally, if the waves being studied have a small amplitude, the non-linear terms can de disconsidered. Therefore, the flux of the mean field is considered to be negligible and $D/Dt = \partial/\partial t$.

Starting from the simplest case, where the effect of viscosity is considered negligible $(\mu = 0)$and assuming the Boussinesq approximation for a uniformly stratified (N does not vary) incompressible fluid without fluxes of the average field, the linearized form of the equations describing the conservation of momentum is given by

$$\rho_0 \frac{\partial u}{\partial t} = -\frac{\partial p}{\partial x}$$

$$\rho_0 \frac{\partial v}{\partial t} = -\frac{\partial p}{\partial y} \qquad (2.4)$$

$$\rho_0 \frac{\partial w}{\partial t} = -\frac{\partial p}{\partial z} - \boldsymbol{g}\rho,$$

which, together with the continuity equation $\nabla \cdot \mathrm{V} = 0$, form a system of 5 equations with 5 unknowns. Therefore, a solution can be derived if the derivatives are defined. these equations can be written in a matrix form, where the subscript denotes the independent variable (i.e.: $\partial_t \equiv \partial/\partial t, \partial_x \equiv \partial/\partial_x$, etc.):

$$\begin{pmatrix} \partial_t & 0 & 0 & 0 & \frac{1}{\rho_0}\partial_x \\ 0 & \partial_t & 0 & 0 & \frac{1}{\rho_0}\partial_y \\ 0 & 0 & \partial_t & \frac{g}{\rho_0} & \frac{1}{\rho_0}\partial_z \\ 0 & 0 & -\frac{\rho_0}{g}N^2 & \partial_t & 0 \\ \partial_x & \partial_y & \partial_z & 0 & 0 \end{pmatrix} \begin{pmatrix} u \\ v \\ w \\ \rho \\ p \end{pmatrix} = 0 \qquad (2.5)$$

For non-trivial solutions the determinant of the matrix should be zero:

$$\left[\partial_{ttt}\nabla^2 + N^2{\nabla_H}^2\partial_t\right]b = 0 \qquad (2.6)$$

In which b is one of the basic state fields (u,v,w,ρ,p) and $\nabla_H \equiv (\partial_x, \partial_y)$ is the horizontal component of the nabla operator.

The Fourier transform gives the dispersion relation for internal waves in an incompressible and uniformly stratified field. Assuming periodic solutions of the form $b(x,y,z,t) = A_b e^{i(kx+ly+mz-\omega t)}$ and substituting it into equation 2.6 we get

$-\mathrm{i}\omega^3|\mathbf{k}^2| + \mathrm{N}^2\mathrm{i}\omega\left|\mathbf{k_H}^2\right| = 0$, for $\mathbf{k_H} = \mathrm{k} + \mathrm{l}$. The non-stationary solutions give the dispersion relation

$$\omega^2 = N^2\frac{\left|\boldsymbol{k}_H{}^2\right|}{|\boldsymbol{k}^2|}, \qquad (2.7)$$

which can be written in terms of the angle of propagation relative to the vertical φ, as $\omega = \mathrm{N}\cos\Theta$. Propagation is associated with the phase velocity $\boldsymbol{c_p} = \omega/\mathbf{k}$ and the group velocity $\boldsymbol{c_g} = \partial\omega/\partial\mathbf{k}$. Plugging the ω expression from Equation 2.7, the velocities with respect to the vertical angle of propagation Θ and the horizontal angle ϕ (implicitly defined as $\tan\phi = (\mathrm{l}/\mathrm{k})$ is then

$$\mathrm{c_p} \equiv \frac{\omega}{|\mathbf{k}|}\frac{\mathbf{k}}{|\mathbf{k}|} = \frac{\mathrm{N}}{|\mathbf{k}|}\cos\Theta\,(\cos\phi\cos\Theta, \sin\phi\,\cos\Theta, \sin\Theta) \tag{2.8}$$

and

$$c_g \equiv \frac{\partial\omega}{\partial k}, \frac{\partial\omega}{\partial l}, \frac{\partial\omega}{\partial m} = \frac{N}{|\boldsymbol{k}|} sin\Theta(\cos\phi\sin\Theta, \sin\phi\,\sin\Theta, -\cos\Theta) \tag{2.9}$$

From the equations above, it is shown that the group and phase velocities are orthogonal to each other. Another interesting consequence of Equation 2.7 is that the maximum group velocity occurs at an intermediate vertical angle $\Theta = \arctan(1/\sqrt{2}) \approx 35°$.

In algebraic terms, the dispersion relation is the eigenvalue of the differential matrix described in Equation (2.5), and the corresponding eigenvectors give a relation between the field properties. In the literature, these relations are known as "polarization relations". Implicitly defining the vertical displacement field ξ as $\mathrm{w} = \partial\xi/\partial\mathrm{t}$, the amplitude of the eigenfunctions $\mathrm{A_b}$ can each be written in terms of the vertical displacement field $\mathrm{A_\xi}$, as shown in Table 2.1. An important property shown in the table is that the vertical and horizontal velocity fields are in phase. A logical

conclusion from that is that fluid parcels oscillate linearly in this system, meaning these parcels have their movement restricted to a line in angle θ with the vertical axis.

The vertical transport of horizontal momentum in the x axis per unit mass is given by the cross correlation $\langle uw \rangle$ between the fields of u and w. This quantity is determined by multiplying the average values over the oscillation period of the real part of both variables. This can be done by integrating either over time $\left(\frac{1}{T}\int_0^T \mathbb{R}(u)\mathbb{R}(w)dt\right)$, space $\left(\frac{1}{\lambda_x}\int_0^{\lambda_x} \mathbb{R}(u)\mathbb{R}(w)dx\right)$ or in relation to phase, by inferring $\phi = k \cdot x - \omega t$:

$$\langle uw \rangle \equiv \frac{1}{2\pi}\int_0^{2\pi} \mathbb{R}(A_u e^{i\phi})\,\mathbb{R}(A_w e^{i\phi})d\phi$$

$$\equiv \frac{1}{2\pi}\int_0^{2\pi} \left[\frac{1}{2}\left(A_u e^{i\phi} + {A_u}^* e^{-i\phi}\right)\right]\left[\frac{1}{2}\left(A_w e^{i\phi} + {A_w}^* e^{-i\phi}\right)\right] \qquad (2.10)$$

$$\equiv \frac{1}{2}\mathbb{R}(A_u {A_w}^*)$$

$$= \frac{1}{4}N^2 \sin 2\Theta \left|A_\xi\right|^2$$

Table 2.1: Polarization relations for internal waves.

Equation	Relation to vertical displacement
Vertical displacement: ξ	Complex amplitude: A_ξ
$\boldsymbol{\rho = -\frac{d\bar{\rho}}{dz}\xi}$	$A_\rho = \left(-\frac{d\bar{\rho}}{dz}\right)A_\xi \quad = \frac{\rho_0}{g}N^2 A_\xi$
$\boldsymbol{V = \nabla \times (\psi \hat{y})}$	$A_\psi = -\frac{\omega}{k}A_\xi \quad = -\frac{N}{k}\cos\Theta A_\xi$
$\boldsymbol{w = \frac{\partial \xi}{\partial t}}$	$A_w = -i\omega A_\xi \quad = -iN\cos\Theta A_\xi$
$u = -\frac{\partial \psi}{\partial z}$	$A_u = i\frac{m\omega}{k}A_\xi \quad = iN sin\Theta A_\xi$
$\boldsymbol{\zeta = -\nabla^2 \psi}$	$A_\zeta = -\frac{\omega}{k}\left\|\vec{k}^2\right\|A_\xi \quad = -Nk\sec\Theta A_\xi$
$\boldsymbol{\Delta N^2 = -\frac{g}{\rho_0}\frac{\partial \rho}{\partial z}}$	$A_{\Delta N^2} = imN^2 A_\xi \quad = -iN^2 k\tan\Theta A_\xi$
$\boldsymbol{N^2{}_t = \frac{\partial \Delta N^2}{\partial t}}$	$A_{N^2{}_t} = m\omega N^2 A_\xi \quad = -N^3 k\sin\Theta A_\xi$
Transport of momentum	$\boldsymbol{\rho_0\langle uw\rangle = \frac{1}{4}\rho_0 N^2 sin2\Theta\left\|A_\xi\right\|^2}$
Wave-induced mean flow	$\boldsymbol{-\langle\zeta\xi\rangle = \frac{1}{2}Nk\sec\Theta\left\|A_\xi\right\|^2}$

In these equations the star denotes the complex conjugate of the variables and $\mathbb{R}$ is the real part of the values. An important consequence is that waves with $\Theta = 0$ or $\Theta = 90°$ do not transport momentum in the vertical axis. Considering waves with the same vertical displacement amplitude A_ξ, those with $\Theta = 45°$ transport the momentum at most. Another implication from the polarization relations is that the density field is $\pi/2$ out of phase with the velocity fields. This can be demonstrated by repeating the procedure used in Equation 2.10:

$$\langle \rho w \rangle \equiv \frac{1}{2}\mathbb{R}(A_\rho {A_w}^*) = 0 \tag{2.11}$$

Yet another useful quantity is the Stokes drift, the mean wave-induced flux which is continuous and directed towards wave propagation. This current is usually a lot smaller than the phase velocity of the waves which generated it and is proportional to their squared amplitude. For internal waves, the stokes drift is given by the cross-correlation between the vertical displacement field (ξ) and the remaining orthogonal component (($\hat{y} = \hat{z} \times \hat{x}$), if we wish to calculate the stokes drift along the x axis) of the vorticity field $\zeta = (\nabla \times u) \cdot \hat{y}$ (Scinocca and Shepherd, 1992) (Sutherland, 1996):

$$-\langle \zeta \xi \rangle \equiv \frac{1}{2}\mathbb{R}(A_\zeta {A_\xi}^*) = \frac{1}{2} N k \sec\Theta \left|A_\xi\right|^2 \tag{2.12}$$

The elegance of the matrix notation is that a rotational force can easily be added into the system. For internal waves occurring in time scales comparable to the period of earth rotation the Coriolis force cannot be neglected. For such we return to the Boussinesq approximation and add the Coriolis force to Equation 2.5:

$$\begin{pmatrix} \partial_t & -f & 0 & 0 & \frac{1}{\rho_0}\partial_x \\ f & \partial_t & 0 & 0 & \frac{1}{\rho_0}\partial_y \\ 0 & 0 & \partial_t & \frac{g}{\rho_0} & \frac{1}{\rho_0}\partial_z \\ 0 & 0 & -\frac{\rho_0}{g}N^2 & \partial_t & 0 \\ \partial_x & \partial_y & \partial_z & 0 & 0 \end{pmatrix} \begin{pmatrix} u \\ v \\ w \\ \rho \\ p \end{pmatrix} = 0 \quad (2.13)$$

Where $f = 2\Omega sin\phi_0$ is the Coriolis parameter (also called inertial frequency), which depends upon the rotational frequency of earth Ω and the local latitude ϕ_0. Assuming plane wave solutions of the form of Equation 2.6, the matrix eigenvalue problem gives am adjusted dispersion relation

$$\omega^2 = N^2 \cos^2\Theta + f^2 sen^2\Theta \quad (2.14)$$

The equation above establishes *f* as the lower frequency cut-off and waves with frequency close to it are called near-inertial waves otherwise inertia-gravity waves. Phase lines for these waves are close to horizontal ($\Theta \sim 90°$) and their polarization relations indicate u and v to be 90° out of phase, which imply fluid parcels draw near-horizontal elliptic paths during the passage of the waves.

Sometimes it is useful to track the propagation of internal waves simply in terms of rays, their diffraction and reflection. This means tracking their vertical coordinate z in relation to the horizontal coordinate x. The rays can be described by an analytical theory contemplating a non-uniform mean background field $\overline{U}(z)$ and a non-uniform stratification $N^2(z)$ as long as we consider the vertical extension of the wave to be

on a much smaller scale than the variation of the background field variables. This is called the WKB approximation, which also means

$$\frac{1}{m} \ll \left|\frac{1}{m}\frac{dm}{dz}\right|^{-1}$$

$$\left|\frac{1}{m^2}\frac{dm}{dz}\right| \ll 1 \tag{2.15}$$

$$\left|\frac{d(m)^{-1}}{dz}\right| \ll 1$$

Under such assumptions the wave trajectory over a plane (x, z) can be described by the function $z(x)$ from

$$\frac{dz}{dx} = \frac{C_{gz}}{C_{gz} + \bar{U}} \tag{2.16}$$

Where the group velocity is given by Equation 2.9.

Weakly nonlinear theory describes the dynamics of waves with non-negligible amplitudes, but still sufficiently small to derive analytic solutions from perturbation theory. Such considerations are usually interesting when considering cases where the superposition principle does not hold, such as wave-wave interactions and interactions between waves and the wave-induced mean flow.

Weakly nonlinear dynamics modify the dispersion relation by adding a nonlinear component A such that $\omega_{NL} = \omega_L(\vec{k}) + \omega_2(\vec{k})A^2$, where $\omega_L(\vec{k})$ is the linearized dispersion relation as determined by Equation 2.7 or 2.14. Constraining motion to

the x-axis, then a periodic wave train can be said to be modulationally stable, that is remaining periodic over an indefinite amount of time, if

$$\omega_2 \frac{\partial^2 \omega}{\partial k^2} > 0 \qquad 2.17$$

For deep water waves, it has been shown that waves are always modulationally unstable, even for water waves of infinitesimally small amplitude. Nevertheless, the instability is unlikely to manifest during the life cycle of very small amplitude waves, since the growth rate of the instability is proportional to the amplitude itself. Benjamin and Feir (1967) analyzed this problem and observed that energy in the spectrum repeatedly transfers to harmonically complementary wavenumbers then transfers back to the original wavenumber, following the Fermi-Pasta-Ulam-Tsingou (FPUT) recurrence phenomena.

For the case of Boussinesq-approximated, non-rotating internal waves, Grimshaw (1975) and Sutherland (2001) have made the analytical consideration that horizontally periodic, vertically compact waves are modulationally unstable to the growth of the vertical sideband wavenumbers if their frequency is higher than that of the waves with the fastest vertical group velocity, such that $\Theta < \Theta_c = tan^{-1}(2^{-1/2}) \approx 35°$.

Sutherland's (2001) weakly nonlinear numerical analysis agreed with these results, but a fully nonlinear simulation further predicting horizontally compact internal waves to be modulationally unstable to the growth of horizontal sideband wavenumber if $\Theta < \Theta > \Theta_c = sin^{-1}(2^{-1/3}) \approx 53°$.

Note that modulational instability does not imply wave breaking, only non-steadiness of a periodic wave train. Nonetheless, the nonlinear interactions associated with the instability may result in overturning and breaking of internal waves.

In general, three waves of wavenumber vector $\overrightarrow{k_i}$ and frequencies $\omega_i \forall\, i \in \{1,2,3\}$ may interact as a "resonant triad" if $\overrightarrow{k_3} = \overrightarrow{k_1} \pm \overrightarrow{k_2}$ and $\omega_3 = \omega_1 \pm \omega_2$. The previous statements are equivalent to requiring $\cos(\Theta_3) = \cos(\Theta_1) \pm \cos(\Theta_2)$ in which Θ is implicitly given by Equation 2.7, as $\cos\Theta = (k + l)/m$. Three possible resonant couplings are interesting in a realistic sense: elastic scattering, in which energy in a high frequency wave is transported to another wave with nearly equal and opposite wavenumber vector; induced diffusion, in which energy in a low frequency wave is transported to a high frequency wave; and parametric harmonic instability, in which energy is extracted from a low wavenumber mode and deposited into high frequency waves with nearly equal and opposite wave numbers. For internal waves that are periodic everywhere in space, internal waves are found to be parametrically unstable even at infinitesimally small amplitudes (Klostermeyer, 1991; Lombard & Riley, 1996). The instability grows through resonant coupling between the initial waves and their superharmonics (whose horizontal wavenumbers are multiple integers of the initial waves.). Through this coupling, the superharmonic waves extract energy from the initial waves and grow in amplitude until the break point.

Internal waves become unstable and break if their temperature is large enough to imply $\partial\rho_T/\partial t \equiv d\bar{\rho}/dz + d\rho/dz > 1$. Using the polarization relation in Table 2.1, the overturning condition can be derived as $A_\xi > A_{OT}$ for

$$A_{OT} = \frac{1}{2\pi} cot\ \Theta \tag{2.18}$$

Numerical experiments exploring interaction between waves and the wave-induced mean flow indicate internal waves are unstable at much smaller amplitudes unless Θ is close to 90°. The criterion for instability, also called the self-acceleration condition, states that wave become unstable if the wave-induced mean flow exceeds the horizontal group velocity. Considering Equation 2.12 and Equation 2.9, waves are unstable if

$$A_\xi > A_{SA} \equiv \frac{\lambda_x}{2\pi\sqrt{2}} \sin 2\Theta \tag{2.19}$$

For $\lambda_x = 2\pi/k$ being the horizontal wavelength. A consequence of Equation 2.19 is that waves with $\Theta \cong 0$ (implying $\omega \cong N$) are unstable to overturning and breaking even at infinitesimally small amplitudes.

The theory briefly described in this Chapter will be of fundamental importance to interpret the results from later sections. Especially important to take in consideration is the orthogonality of phase and energy, along with the principles behind the weakly non-linear internal wave theory.

Chapter 3: Seasonal Variation and Governing Dynamics of the Mixed Layer in the Indian Sector of the Southern Ocean

Partially published as Ferreira Azevedo, M., Aoki, S. & Kitade, Y. (2022), Seasonal variation and governing dynamics of the mixed layer in the Indian sector of the Southern Ocean. *Journal of Geophysical Research: Oceans,* 127, e202IJC017838.

3.1 Introduction

The Southern Ocean is essential for the Earth's climate and ecosystem, as it is the region where water from all oceans converges and mixes, unbounded by land, under the influence of westerly winds. This ocean-water mixing in the Southern Ocean leads to oxygenated surface water with a unique combination of temperature, salinity, and nutrients, which is characteristic of the austral conditions that formed it. The wider region offshore of the Adélie Land near 140 °E is particularly important for the Southern Ocean system, characterized by strong wind stress curl (Trenberth et al., 1989), increased sea-ice production (Tamura et al., 2008, 2012), and bottom-water formation (Rintoul, 1998; Williams et al., 2010). The mixed layer is an integral part of this ocean system, as it links the atmosphere to the deep ocean; its depth indicates the water volume directly interacting with the atmosphere.

Temperature, salinity, and depth of the mixed layer (ML) in the Southern Ocean follow a pronounced seasonal cycle, which is largely attributed to the air–sea heat fluxes, while an Ekman-dominated advection plays a secondary role (Dong et al., 2007). Acting upon the seasonal variability, submesoscale processes such as

Ekman buoyancy fluxes and mixed layer eddies have been shown to modulate the ML properties on the scale of hours to days, either enhancing or weakening stratification (Bachman et al., 2017). Furthermore, du Plessis et al., (2019) have also shown that these processes are fundamental on larger time scales such as the transitional period of spring restratification, possibly arresting the seasonal restratification by up to two months after the surface heat flux becomes positive.

However, because only limited Southern Hemisphere data are available for reanalysis products, fluxes derived based on these data are considered to be highly uncertain, while the air–sea heat flux is considered to be the largest contributor to the surface heat-budget error (Dong et al. 2007).

Mixing observations are sparse, and our limited understanding of the physical processes behind turbulent mixing leads to inaccurate representations of mixing in ocean general circulation models (Wunsch and Ferrari, 2004). Meyer et al. (2015) characterized the spatial and temporal variability of density diffusivity (K_ρ) on the Kerguelen Plateau using profiling floats and estimated a two-order increase of the density diffusivity related to internal wave propagation; nevertheless, they also found strong spatial and temporal variability ranging from $O(10^{-6})$ to $O(10^{-3})$ $m^2\ s^{-1}$. Observed enhanced turbulent mixing near the Antarctic Slope Front at 140 °E was associated with an interaction between the M_2 tidal harmonic and the shelf-break bathymetry, while generating events with $K_\rho > 10^{-3}$ $m^2\ s^{-1}$ (Hirano et al., 2010). Furthermore, Waterman et al. (2013), utilizing coupled Conductivity-Temperature-Depth (CTD), Lowered Acoustic Doppler Current Profiler (LADCP) and microstructure profilers, found evidence of a local relation between near-inertial internal wave energy and turbulent dissipation in the upper 1000 m of the water

column in the Kerguelen Plateau. However, while ship and buoy measurements have elucidated Southern Ocean dynamics, the lack of continuous, year-round, high temporal resolution data is still a limitation. Intercomparisons of a number of turbulent heat-flux climatologies (Smith et al., 2011; Yu et al., 2011) revealed large discrepancies among them, with uncertainties comparable to the mean values in the Southern Ocean.

Although mooring systems from projects such as the Southern Ocean Observing System (SOOS) (Rintoul et al., 2012; Schulz et al., 2012; Newman et al., 2019) and the Japanese IPY program (Ohshima et al., 2013; Williams et al., 2016) exist, they monitor either the sub-Antarctic Zone (i.e., 45–47 °S) or the coastal area south of 66 °S. The DIMES mooring system, deployed in the Scotia Sea, has provided valuable data on how mesoscale flow and the internal wave field interact but miss the first 400 m of the water column, where the non-barotropic, non-linear and non-hydrostatic dynamics of the mixed layer might diverge from the previously published results. Sevéllec et al. (2015) used these moorings to quantify vertical flow, identifying the barotropic component as being dominant; however, their vertical flow theory does not contemplate a hydrostatically unstable scenario, common in the Southern Ocean. Furthermore, Cusack et al. (2020) determined that eddy-internal wave interaction produce a mean negative (wave to eddy) energy transfer but predicts their energy transfer estimations to be skewed by lack of shallower sampling, since it is in the top few hundreds of meters where eddy strain rates and horizontal gradients are greatest, and dynamics become highly non-linear.

A missing aspect of the existing studies on the Southern Ocean surface is, therefore, analyses of its short-term/seasonal variability and mixing. We address this

aspect by utilizing a mooring system and analyzing time series and vertical profiles of temperature, salinity, and density, while estimating their vertical diffusivity and observing their variations according to changes in net heat flux, fronts, and eddies, as well as the passage of near-inertial internal waves. We explore how surface variability can be transported downwards and interact with deeper water masses that compose the austral ocean. Our objective is to quantitatively describe the influence of each forcing on the mixed layer, temporally constrain surface cooling, and verify whether the near-inertial internal waves detected in the region are capable of diapycnal transport of energy and salt below the mixed layer.

In this paper, we first describe the region, our sampling system, and the datasets in section 3.2. In section 3.3, we explore the seasonal evolution of the upper layer by comparing the time series of the physical properties of water, current and wind velocity, and air-ocean heat flux. In section 3.4, we use simplifications and parametrizations to estimate the upper layer vertical diffusivity of temperature, salinity and density within our data constraints. In section 3.5, we use a box model to explain how much of the observed variation is local in nature (i.e., surface cooling) and how much is caused by advection, while frontal shifts, temporal variation of nearby meanders, and the passing and/or intensification of eddies are visually mapped. Finally, in section 3.6, we discuss and contextualize our results and their implications.

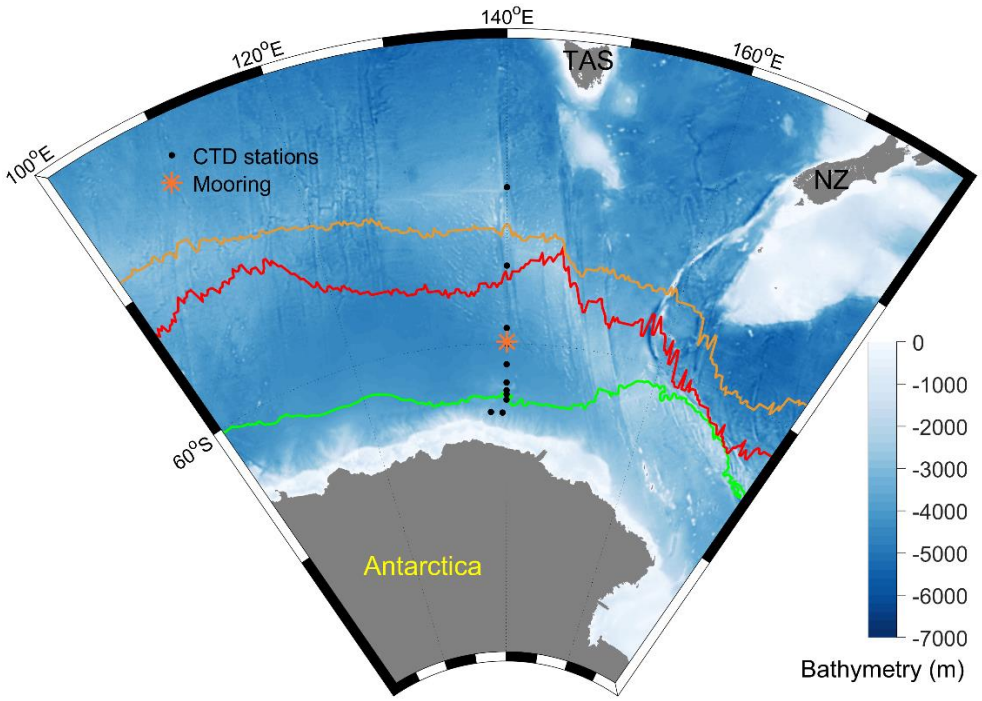

Figure 3.1. Orthographic projection map of the sampling points. CTD casts and the mooring are indicated by black dots and an orange asterisk, respectively. The orange, red, and green lines represent the sub-Antarctic (SAF), polar (PF), and southern Antarctic Circumpolar Current (SACCF) front, respectively, calculated from the climatological dataset of Shimada et al. (2017), using the potential temperature criterion established by Orsi et al. (1995) and the sea surface high (SSH) ranges proposed by Sokolov and Rintoul (2002).

3.2 Observations and datasets

A mini triangle trans-ocean buoy network (m-TRITON) mooring was deployed in January 2012 as part of the KARE-17 expedition onboard the TR/V Umitaka-maru. The mooring deployed the miniaturized version of the TRITON surface buoy (m-TRITON) developed by JAMSTEC for the Japanese contribution to the Tropical Atmosphere Ocean (TAO) project and has been detailed by Ishihara and Mizuno (2010). Our specific instrumentation is detailed in Table 3.1. CTD data were calibrated against SBE3 and SBE4 sensors in a calibration bath before deployment and post-corrected for accuracy drift.

We deployed 5993 m of cable to a 4497 m deep location, which made room for 3950 m of horizontal deviation from the original mooring position. Ballast weights amounting to 200 kg were fixed below the 1430 m CTD to keep the upper portion of the mooring straight. This setup had the advantage of easing sensor knockdown at the expense of increasing error to current velocity estimations. As a result, sensor knock down was mostly constrained to ± 5 m from nominal depth. The horizontal displacements of the CT and CTD sensors were considered to be functions of pressure variations, with the error due to depth variations of both temperature and salinity constrained to $O(10^{-4})$ of their respective units.

Table 3.1: *Mooring Placement and Sensor Specification.*

Sensor name	Brand	Measured variables	Depth	Accuracy
SBE 37-SI MicroCAT	Sea-Bird Scientific	Temperature, conductivity, pressure	10 m, 50 m, 100 m, 150 m, 400 m, 800 m, 1430 m, B-400 m, B-200 m, B-100 m, B-50 m	$\pm 2 \times 10^{-3}$ °C $\pm 5 \times 10^{-4}$ S m^{-1}
Workhorse sentinel ADCP 300kHz	Teledyne	Current velocity	1.5 m, B-100 m	$\pm 5 \times 10^{-3}$ m s^{-1}
INFINITY CTW	JFE Advantech	Temperature, conductivity	1.5 m	$\pm 2 \times 10^{-3}$ °C $\pm 5 \times 10^{-4}$ S m^{-1}
WXT520	Vaisala	Precipitation, air pressure	Surface	$\pm 5\%$
SWR PSP	JAMMET	Shortwave incoming heat flux	Surface	± 1~3%
Deployment Point: 59.9°S 140°E	Deployment date: 16 January 2012		Retrieval date: 18 December 2012	

Data for temperature, conductivity and pressure were collected every 20 minutes, while current data were collected at the same interval but in 3-second bursts of 50 samples. Bursts were subsampled as their median value and binned in 4-m cells. We define cells by their middle depth, so they include ± 2 m measurements from their nominal depth value. The most superficial cell is at 6.24 m deep.

ADCP current velocities were corrected to account for the buoy motion by estimating the buoy mean velocity from its GPS position, updated hourly, which was then added to the ADCP readings. Buoy velocity never exceeded 11.6% of the sensor values, a velocity increase on the order of 10^{-2} m s^{-1}. ADCP data were also corrected for sound speed variation, although the effect of this correction did not exceed 1.4×10^{-3} m s^{-1}. The buoy position over time highlighted the strength of the ACC over other factors, as the buoy rarely drifted toward the west side of the deployment location.

The top buoy was set at the surface equipped with atmospheric sensors, although data collection was only successful for surface pressure, downward shortwave radiation, and precipitation. The mooring recorded data at 60 °S and 140 °E over 11 months between 15 January and 19 December 2012 and additional high-resolution CTD rosette casts were done at the time of mooring deployment and retrieval. The sampling location is shown in Figure 3.1, where the relevant frontal structures associated with the Antarctic Circumpolar Current (ACC) are displayed.

By comparing the CTD profiles taken during summer, as shown in Figure 3.2, with the mooring data, it was possible to characterize the transect in terms of its principal features and understand how these features evolve over time. Mixing between the upper Circumpolar Deep Water (uCDW, defined by $27.5 < \gamma_n < 28$ kg m^{-3} ;

Abernathey et al., 2016) and the surface mixed waters above (Figure 3.2a) explained a large portion of the vertical density distribution in the upper layer. The surface layer appeared to be affected by the low salinity caused by precipitation and sea ice melting during summer (Figure 3.2b), while remnant Winter Water forming a layer with minimum temperature was identified between 75 and 150 m depth (Figure 3.2c).

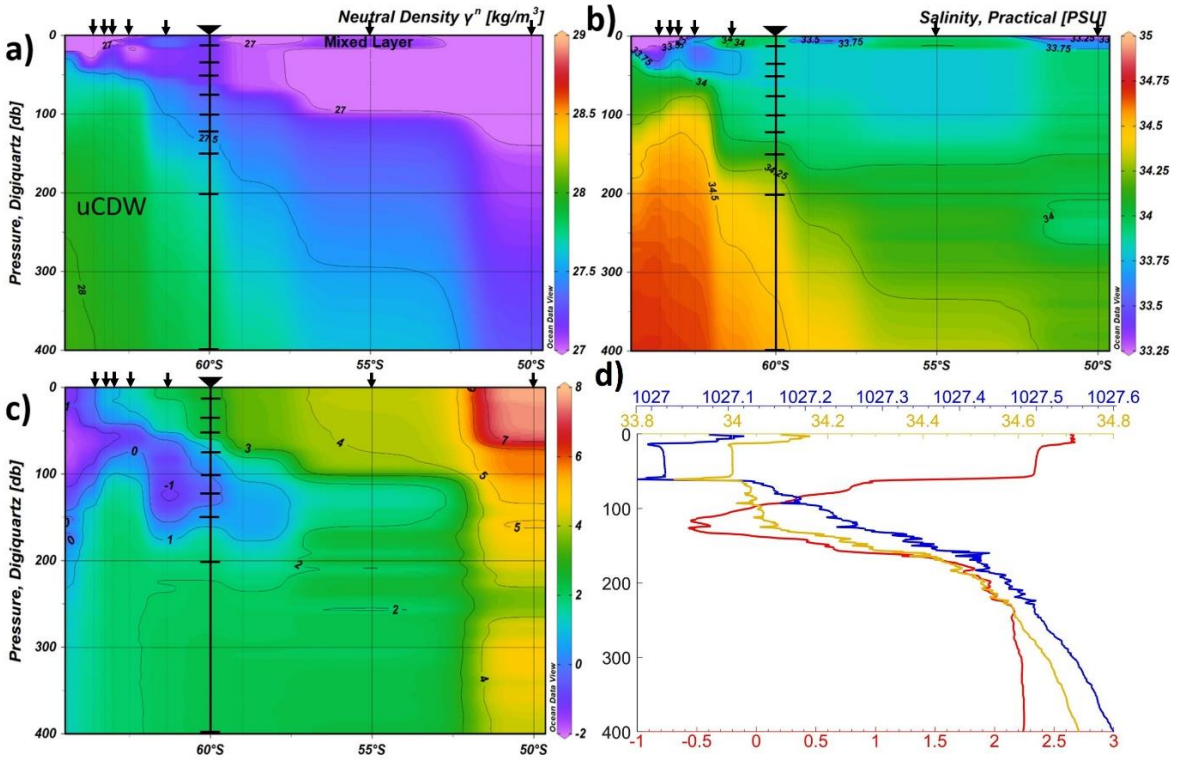

Figure 3.2. Vertical section from conductivity, temperature depth (CTD) casts along 140 °E: (a) Neutral density (γ_n (kg m^{-3})), (b) salinity, and (c) potential temperature (°C) in the upper layer; mooring sensors are indicated by thick horizontal lines, while the top arrows indicate CTD casts. (d) January vertical profiles of potential temperature, salinity and potential density in red, yellow and blue, respectively.

The upper structure of the mooring consisted of a surface, buoy-mounted, ADCP, and a temperature sensor (INFINITY-CTW, JFE Advantech), followed by a string of eleven CTs and CTD sensors (SBE37, Sea-Bird Electronics). Temperature and salinity data were filtered using a 1 hour running median to remove outliers and account for the difference in sampling rate between the temperature and salinity sensors from raw measurements. The variability around the inertial period, $2\pi/f = 13.85$ hours at 60°S, was evidenced by isolating the inertial band (between 8 and 16 h) from long period variability (>16 h) by using a 4th order Butterworth filter. The same filter was used to separate current velocity into these bands and was applied twice—first forward and subsequently backwards—to minimize phase distortion. The CTD sensor at 50 m stopped working reliably after five months of operation (i.e., at the end of May). Thus, data from this point onward were interpolated from the 30 and 75 m depth, which was deemed reasonable because during most of the interpolated period, the 50 m depth was part of the mixed layer with exception of the period after 5 November. The error, estimated by withholding data from the period where data at this depth is available and the mixed layer depth is deeper than 50m and comparing with the original series, did not exceed 0.02 °C and 0.006 PSU. MLD estimation was performed by finding the layer in which the potential density (σ_θ) exceeded the 10m deep value by 0.03 kg m^{-3}, as proposed by de Boyer Montégut et al. (2004) and Dong et al. (2008). Different ML criteria, such as those suggested by Kilbourne and Girton (2015) and Monteray and Levitus (1997), were tested and differed by at most 12 m between January and September. However, MLD calculation in the period of deep mixing between 19 September and 20 November is very sensitive to the chosen criterion, ranging from 150m (Kilbourne and Girton, 2015) to 400m (de Boyer Montégut et al., 2004). The mooring's vertical resolution

was too low to produce an accurate MLD during this period but proves that MLD extends deeper than 150m, of which the significance is explored in section 2.5.

To calculate the heat and freshwater budgets across the sea surface, information on wind velocity, atmospheric pressure, sea-surface temperature (SST), sea-surface–atmosphere heat flux, total precipitation, and evaporation estimations were taken from the European Centre for Medium-range Weather Forecasts ERA5 output (Hersbach et al., 2018) at 1 h temporal resolution. Independent buoy data were used to validate downward shortwave radiation and surface pressure from the ERA5 reanalysis. ERA5 pressure estimates have been considered reliable (Figure 3.3a), thereby supporting the representation of synoptic-scale atmospheric phenomena in the high-latitude Southern Ocean. Downward shortwave radiation from the two datasets were generally in agreement; they exhibited similar values during winter, but there was also an overestimation by ERA5 from January to May (mean: 16 W m^{-2}) and from August to December (mean: 34 W m^{-2}, but with a maximum of 127 W m^{-2}), as shown in Figure 3.3b. ERA5 represents the mean over a 0.25° square grid; thus, a possible explanation for the larger differences at these periods is the increased heterogeneity of atmospheric variables in a scale smaller than 28 km. Buoy-mounted precipitation sensors were found to disagree with ERA5 by a mean of one order of magnitude, but also by periodicity and phase (Figure 3.3c). Most precipitation data in the Southern Ocean is currently gathered using airborne methods and this is the type of data ERA5 incorporates, so the constant overestimation of our measurements attest to the challenges of setting a buoy-mounted precipitation sensor in the harsh conditions of the Southern Ocean. The 3.5 m tall sensor tower was not enough to prevent water spray interference, so a taller tower or a different method is necessary for successful direct measurements of

precipitation. Considering these factors, we decided to use the reanalysis estimates instead.

Absolute dynamic topography data were taken from the Copernicus marine service SSALTO/DUACS combined satellite dataset (Taburet et al., 2019) to observe eddies and their influence on lateral advection of heat and salt. The error of using such a dataset was constrained by comparing the ADCP data with the geostrophic velocity derived from the dynamic topography. The root-mean-square error between the two remained below 0.06 m s^{-1} over the entire analyzed period.

Heat flux was estimated as $Q_{net} = Q_{SW}(1 - a) + Q_{LW} + Q_L + Q_S$ where Q_{SW}, Q_{LW}, Q_L, and Q_S are the downward shortwave and upward longwave radiation, and latent and sensible heat fluxes, while a is the albedo of salt water. This calculation was based on ERA5 data for all parameters except for Q_{SW}, for which buoy readings were used. All parameters were considered to be positive when directed away from the sea surface, i.e., a positive net heat flux indicates flux toward the atmosphere, while the sea surface loses heat. Conversely, the ocean–atmosphere freshwater flux is expressed as $E - P$ where E and P are the evaporation and total precipitation, respectively: A negative flux implies that the surface layer receives freshwater input from the atmosphere.

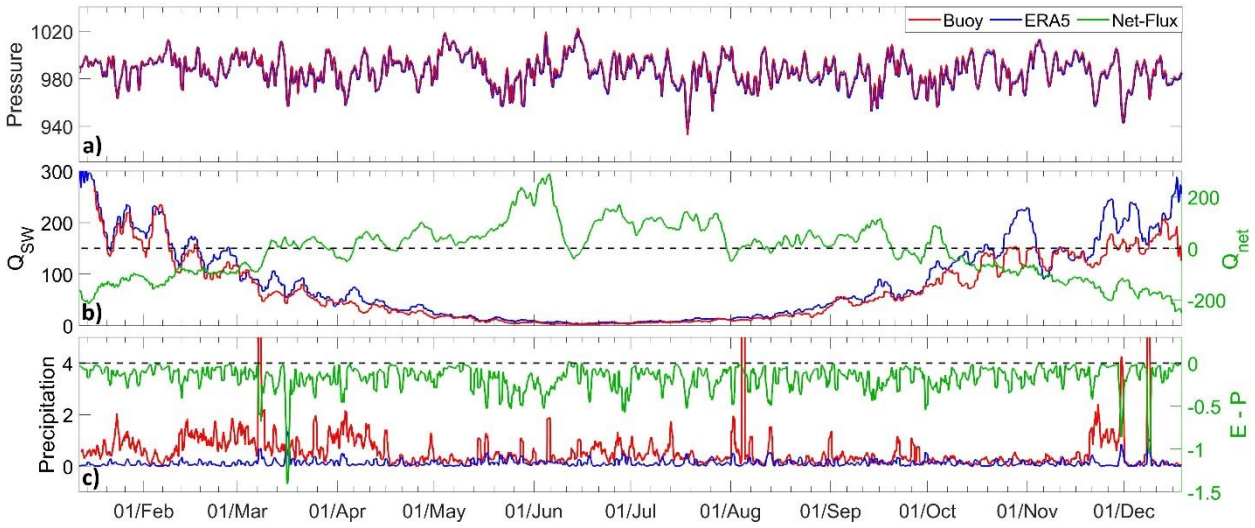

Figure 3.3. Comparison between time series of (a) surface pressure (hPa), (b) downward shortwave radiation (W m^{-2}; five-day average), and (c) total precipitation (mm h^{-1}) from the M-Triton buoy (red) and the ERA5 reanalysis (blue). Green lines in (b) and (c) indicate the net flux of these quantities; black dashed lines indicate zero.

3.3 Seasonal evolution of the upper layer

The surface layer lost significant heat to the atmosphere between 7 April and 7 October, as shown in Figure 3.3b. Although Q_{net} behaved cyclically, the freshwater flux was negative throughout the year (Figure 3.3c).

A comparative graph of the time series of the mooring data is shown in Figure 3.4. Surface cooling had pronounced effects on temperature, salinity, density, and MLD, which extended from the surface down to below 150 m depth. Surface temperature (Figure 3.4a) started decreasing in the second half of April; this instability facilitated the deepening of the MLD (Figure 3.4f, shown along with the buoyancy frequency), which reached 125 m depth in the beginning of June. Surface salinity (Figure 3.4b) was observed to increase in winter and decrease in summer, although it was relatively stable at small timescales; this contrasts the 0.0038 m day^{-1} annual mean

freshwater input from the atmosphere to the surface, which should be balanced by horizontal advection and/or vertical transport. By defining MLD by a density threshold, temperature and salinity are not always homogeneous. A weakly stratified layer often develops and it is hard to distinguish from the ML using density thresholds (Kilbourne & Girton, 2015). Therefore, we checked whether temperature or salinity was the dominant contributor to upper water stability by calculating the density ratio from mooring data, defined as defined as $\mathrm{R_\rho} = (\alpha/\beta)(\Delta\mathrm{T}/\Delta\mathrm{S})$, where α and β are the thermal expansion and haline contraction coefficients, respectively, and ΔT and ΔS are the temperature and salinity differences between adjacent sensors. A surface bulk estimate, calculated from taking the mean $\mathrm{R_\rho}$ from the upper 100 m of the water column, shows this layer to be most frequently dominated by the salinity contribution, but short and intense events of temperature dominance occur frequently, during the destratification and restratification periods, and sparsely through winter. Generally, the major increases in MLD are associated with temperature-induced instability at the lower boundary.

It is also notable how strong wind events, as seen in Figure 3.4e, were followed by sudden variations in temperature and salinity, quickly mixing the 125 m layer on 26 May when, in addition to high wind velocity, the lowest (most negative) curl of wind stress in the series was observed. During winter, large variations of temperature and salinity occurred at 150 m depth, with decreases by as much as 2.32 °C and 0.42, respectively, despite less than 5 m sensor-depth variation due to mooring motion in that period. This variation coincided with the intensification of cyclonic eddies southward of the mooring position, advecting cold subsurface waters northward, suggesting complex meandering ACC pathways exist beneath the sea-air flux

dominated superficial layers. The resulting decrease in stability allows the possibility of communication between surface variability and layers below the MLD.

At 400 m depth, salinity remained relatively constant, but had a periodic component with significant amplitude at about 85.3 days (RMS amplitude: 0.2512), 56.9–13.0 days (RMS amplitude: 0.0038), and the near-inertial band (RMS amplitude: 0.0021), as calculated from a Fourier transform of the time-series. Salinity variations in the near-inertial band were one order of magnitude higher than what could be attributed to sensor-depth variations.

While the temperature at the surface layer became lower in winter, it increased at 150 m, thereby indicating a possible intrusion of warm water in the region. In contrast to conditions in winter, surface layers return to a stratified state as the ocean surface heats during summer.

During the transition from summer to winter, near-inertial internal waves (NIWs) were identified at the base of the mixed layer, propagating both up and downwards. Strengthening of NIWs preceded deepening of the ML by around 15 days. During May, the MLD was at the limit of the ADCP detection range; hence, registering it through current speed proved to be difficult, but the NIW dynamics could be observed in March through the inertial band-filtered potential density (Figure 3.5a) and current readings (Figures *3*.5b–c). Below the homogeneous layer, vertical propagation could be observed, with 1.3×10^{-3} and 8.3×10^{-4} m s^{-1} mean vertical phase velocity during the summer and autumn event, respectively (Figures 3.5b–c). The NIW oscillatory pattern in potential density was observed at both 75 and 100 m depth.

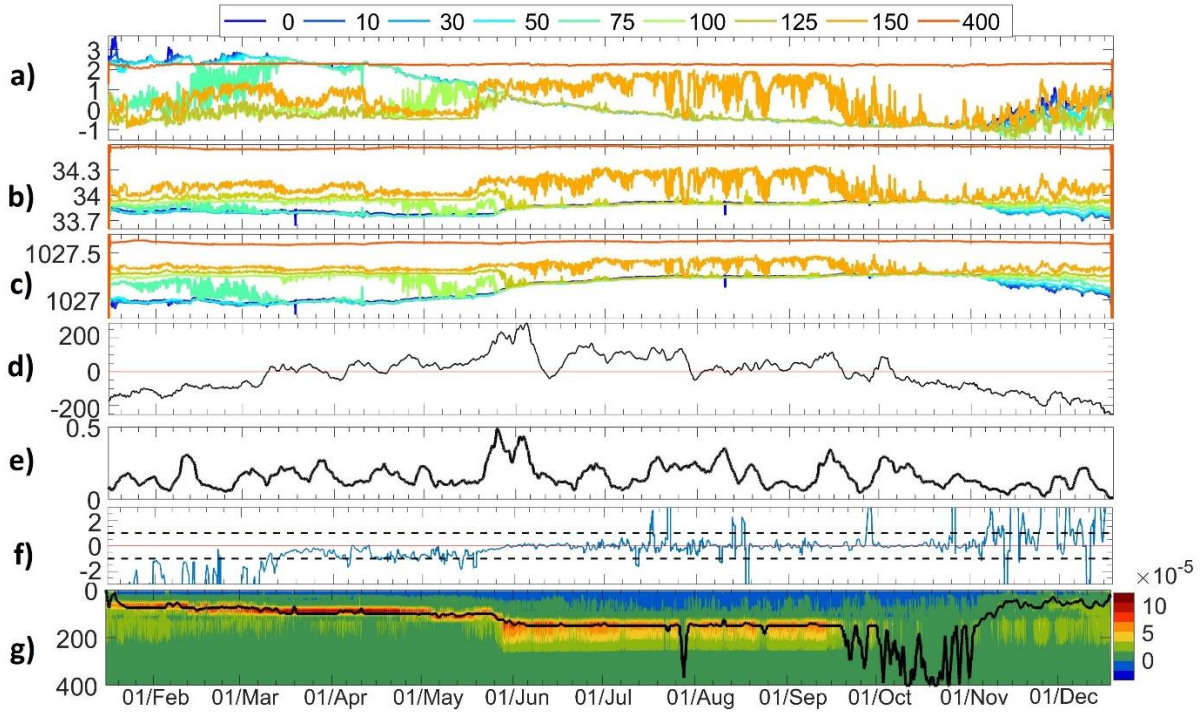

Figure 3.4. Time series of (a) potential temperature (°C), (b) salinity, (c) potential density (Kg m^{-3}), (d) net heat flux (W m^{-2}; five-day average), (e) wind stress, which is parametrized as the friction velocity $V^* = \sqrt{\tau/\rho_{air}}$ (m s^{-1}) and (f) bulk R_ρ; the black dashed lines mark the thresholds for salinity dominated stability (-1<R_ρ<1) and temperature dominated stability (R_ρ>1 or R_ρ<-1 for temperature as a destratifying or stratifying factor). Depth is color coded as shown on top of the figure, and positive net heat flux is directed away from the sea surface. (g) Temporal evolution of the vertical distribution of the buoyancy frequency squared (s^{-2}); the black line indicates the MLD.

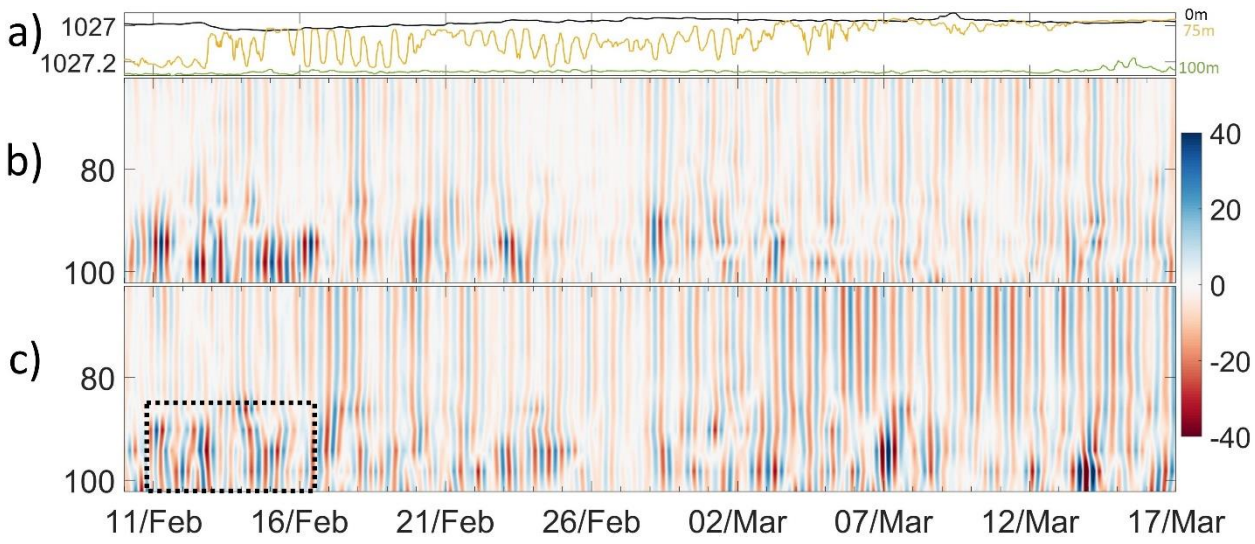

Figure 3.5. (a) Comparison between density at the surface, 75, and 100 m depth (black, orange, and green lines, respectively). (b) Meridional and (c) zonal inertial band velocity. A typical period of internal wave propagation is highlighted.

3.4 Upper layer vertical diffusivity

We expect the decrease in NIW energy content at the base of the mixed layer during summer to be caused by a turbulent energy transformation at the interface; therefore, we investigated how the vertical diffusivities of density (K_ρ), temperature (K_T), and salinity (K_S) change in response to internal wave propagation. To estimate the diffusivities from the relatively coarse vertical resolution, we assumed incompressibility of the water column, a three-dimensionally independent diffusivity tensor, and the vertical coordinate to be normal to the isopycnal to approximate the conservation of density, as shown in Equation 3.1. Temperature, salinity, and density were interpolated from pressure over a 20-m regular grid, and extreme values found during the passage of eddies were smoothed out by taking the 15-day average diffusivity, so that our estimates isolate the local superficial forcing. Our method is based on the theory proposed by Gargett (1984):

$$\frac{\partial \rho}{\partial t} + X = K_\rho \frac{\partial^2 \rho}{\partial z^2}, \tag{3.1}$$

where $X = u_i \frac{\partial \rho}{\partial x_i}$ is the lateral advection of ρ.

By taking the time average, we assume the horizontal advection term X becomes sufficiently small so that it can be disregarded and K_ρ can be approximated as

$$K_\rho \approx \frac{-\partial \rho}{\partial t} \Big/ \frac{\partial^2 \rho}{\partial z^2} \tag{3.2}$$

Note that K_ρ, as well as the posterior temperature and salinity parametrizations given in equation 3.3, are negative in the presence of double diffusive convection or horizontal advection.

This assumption is valid unless a stationary front stays near the mooring position for a time on scale comparable to that of the average window; further discussion is provided in section 3.6. During periods where inertial density variability was observed, the average K_ρ at the boundary of the mixed layer was of the order of 10^{-3}, reaching $1.8 \times 10^{-3} \pm 5 \times 10^{-3}$ and $3.1 \times 10^{-3} \pm 3.3 \times 10^{-3}$ $m^2\ s^{-1}$ at 80 and 100 m depth, respectively. These values were considerably higher than the estimated mean values during a period without this inertial variability, which were estimated at $2.1 \times 10^{-5} \pm 7.1 \times 10^{-4}$ and $-3.9 \times 10^{-6} \pm 3.3 \times 10^{-4}$ $m^2\ s^{-1}$ at the 80 and 100 m layers, respectively, as shown in Table 3.2. Inertial variation of density at the ML boundary preceded further deepening by roughly 15 days on both observations. The 15-day mean K_ρ time series is shown in Figure 3.6.

Table 3.2. *Average K_ρ During Periods of Near-inertial Wave Propagation, and Annual Mean Excluding These Periods.*

Feb 12^{th} - Mar 17^{th}		Apr 24^{th} - May 26^{th}		No IW propagation period	
Depth (m)	K_ρ (m^2 s^{-1})	Depth (m)	K_ρ (m^2 s^{-1})	Depth (m)	K_ρ (m^2 s^{-1})
20	-4.4×10^{-6}	20	-1.0×10^{-4}	20	-2.2×10^{-4}
40	1.9×10^{-5}	40	1.0×10^{-2}	40	4.9×10^{-6}
60	-1.1×10^{-5}	60	-1.3×10^{-6}	60	3.0×10^{-6}
80	5.9×10^{-4}	80	-8.6×10^{-5}	80	2.1×10^{-5}
100	-4.7×10^{-5}	100	1.0×10^{-3}	100	-3.9×10^{-6}
120	-9.6×10^{-6}	120	8.3×10^{-5}	120	4.2×10^{-4}

By approximating the diffusion of density, the diffusion of temperature and salt (T, S) could also be estimated by considering both the case of a totally turbulent layer, which implies that the respective diffusivity coefficients K_θ and K_S are equal to K_ρ, and the case of double diffusive convection (either as salt-fingering or double diffusion) by observing the density stability ratio $\mathrm{R_\rho}$. The Zhang et al. (1998) parametrization can then be applied to the following set of equations:

$$\mathrm{K_S} = \frac{1\mathrm{E}-4}{\left(1+\left(\frac{\mathrm{R_\rho}}{1.6}\right)^6\right)} + 3\mathrm{E}-5, \qquad (3.3)$$

$$\mathrm{K_T} = 1\mathrm{E}-4\frac{\frac{\gamma_{\mathrm{SF}}}{\mathrm{R_\rho}}}{\left(1+\left(\frac{\mathrm{R_\rho}}{1.6}\right)^6\right)} + 3\mathrm{E}-5.$$

For $1.0 < \mathrm{R_\rho} < 1.9$, the density ratio is characteristic of salt fingering, and utilizes a constant γ_{SF} factor of 0.7. In the case of diffusive convection (i.e., $0 < R_\rho < 1$), the Kelley (1990) parameterization is applied as follows:

$$\gamma_{DC} = \frac{\left(\mathrm{R_\rho^{-1}} + 1.4\left(\mathrm{R_\rho^{-1}} - 1\right)^{\frac{3}{2}}\right)}{\left(1 + 14\left(\mathrm{R_\rho^{-1}} - 1\right)^{\frac{3}{2}}\right.}, \tag{3.4}$$

$$\mathrm{K_T} = 0.0032\exp\left(4.8\mathrm{R_\rho^{0.72}}\right)\left(0.25 \times 10^9 \mathrm{R_\rho^{-1.1}}\right)^{\frac{1}{3}}\mathrm{K_T} + 3\mathrm{E} - 5,$$

$$\mathrm{K_S} = \mathrm{R_\rho} \cdot \gamma_{DC} \cdot (\mathrm{K_t} - 3\mathrm{E} - 5) + 3\mathrm{E} - 5.$$

The time series of the diffusivity coefficients (Figure 3.6) show enhanced diffusivity during periods of mixed layer deepening, as well as periods of intensified stratification and of hydrostatic instabilities such as between Apr 15th and May 22nd, where N^2 was negative in the ML. This indicates that in the first 100 m of the water column, $\mathrm{K_\rho} = \mathrm{K_S} = \mathrm{K_T}$, i.e., the diffusivity was mainly turbulent up until the end of June, when it became dominated by salinity and temperature diffusion. Even though these layers became homogeneous in terms of density, salinity, and temperature, diffusion was still significant, which might be an indication of diapycnal diffusion of salt and temperature from the surface. Although not shown in the graph, a consistently positive $\mathrm{R_\rho}$ was found at 125 m depth except in winter, indicating that double diffusion could be a major mixing factor at this layer. This result is consistent with the relatively cold remnant winter water at this layer, which was observed during the deployment cruise. Similar values were found at 150 m depth, indicating double diffusion, while the readings below, at 400, 800, and 1481 m depth, were found to be stable.

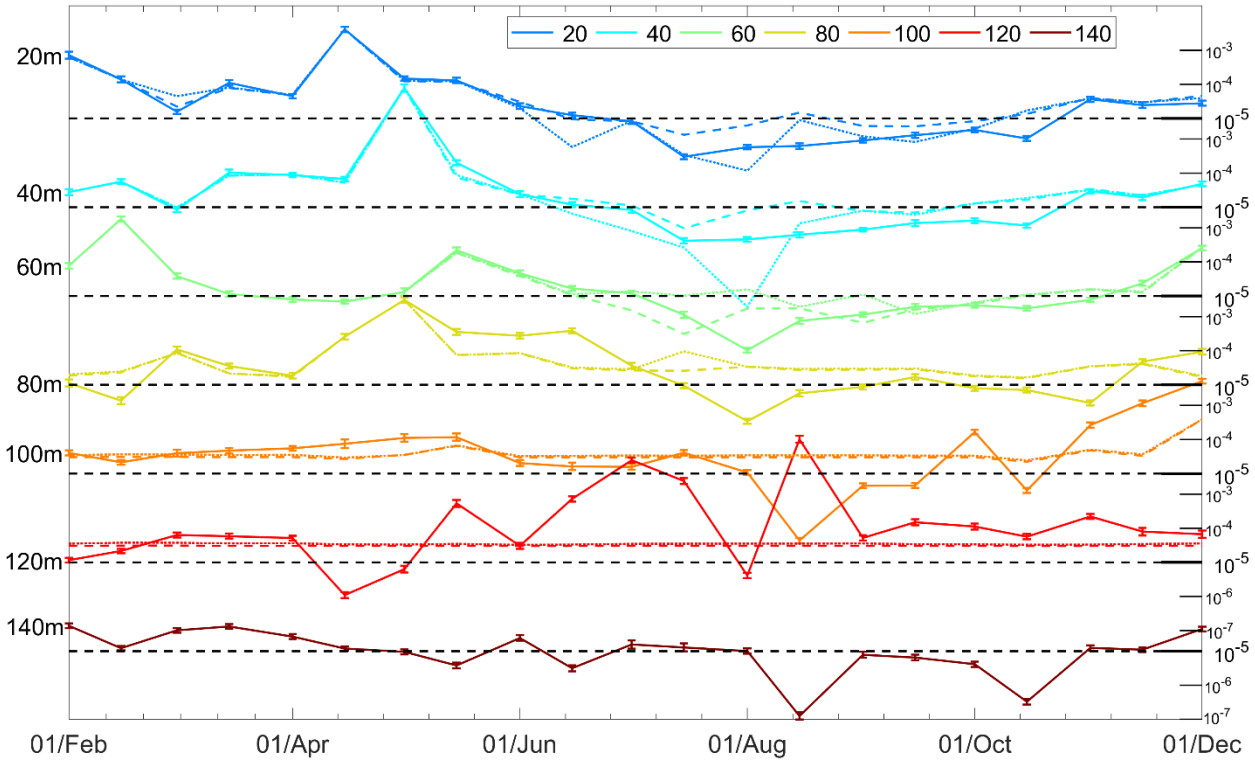

Figure 3.6. Absolute values of diffusivity coefficients between February and November according to depth; K_ρ, K_S, and K_θ are depicted as the solid, dashed, and dotted colored lines, respectively. Black dashed lines indicate 10^{-5} at each depth.

2.5 Box model of surface layer temperature and salinity

Using the previously estimated diffusivity coefficients, a box model was built considering only the vertical diffusivity, air–sea net heat flux, and freshwater balance between evaporation and precipitation; thus, the difference between the model and the sampled data were assumed to be caused by the horizontal advection factor X, which was not included in the preceding diffusivity estimations. We considered a 20 m deep regular vertical grid, under an hourly time step and a virtually infinite reservoir below 3000 m. The 20-m box size was chosen after testing many values

and was found to be both responsive to surface variability and sufficiently thick to accommodate the diffusivity fluctuations under our time-step.

The vertical flux between each box can be calculated for the temperature as $F_T = -K_T \cdot \frac{\partial \overline{T}}{\partial z}$ and for salinity as $F_S = -K_S \cdot \frac{\partial \overline{S}}{\partial z}$. The temporal variation of these properties in each box—excluding the surface box—can be discretized as an explicit scheme, as shown in equations 3.5a–b for T and S:

$$\begin{aligned} F_{T,z}^{t} &= K_{T,z}^{t} \frac{T_{z+1}^{t} - T_{z}^{t}}{\delta z}, \\ \frac{T_{z}^{t+1} - T_{z}^{t}}{\delta t} &= \frac{1}{\delta z}\left[F_{T,z}^{t} - F_{T,z+1}^{t}\right], \end{aligned} \tag{3.5a}$$

$$\begin{aligned} F_{S,z}^{t} &= K_{S,z}^{t} \frac{S_{z+1}^{t} - S_{z}^{t}}{\delta z}, \\ \frac{S_{z}^{t+1} - S_{z}^{t}}{\delta t} &= \frac{1}{\delta z}\left[F_{S,z}^{t} - F_{S,z+1}^{t}\right], \end{aligned} \tag{3.5b}$$

where z and t are the vertical and time indices, respectively, and δ denotes the discretized step. The surface variation (z=1 is taken at the surface) was modeled as equation (3.6a, b) for T and S:

$$T_{z=1}^{t+1} = T_{z=1}^{t} + \frac{F_{T,z=1}^{t}}{V} - \frac{Q_{net}^{t}}{CM}, \tag{3.6a}$$

$$S_{z=1}^{t+1} = \frac{VS_{z=1}^{t}}{V - E + P} + \frac{F_{S,z=1}^{t}}{V}, \tag{3.6b}$$

with $V(m^3)$ being the volume of the box, $C(J\ kg^{-1}\ °C^{-1})$ being its specific heat capacity, $M(kg)$ being the mass contained inside the box, E being the hourly accumulated evaporation, and P being the hourly accumulated total precipitation taken from ERA5.

Additionally, a density inversion scheme was employed, where two boxes would mix completely over the course of two hours if a density inversion was detected between them, to account for convective adjustment. The model was then initialized from the interpolated mooring values of temperature and salinity six hours after deployment.

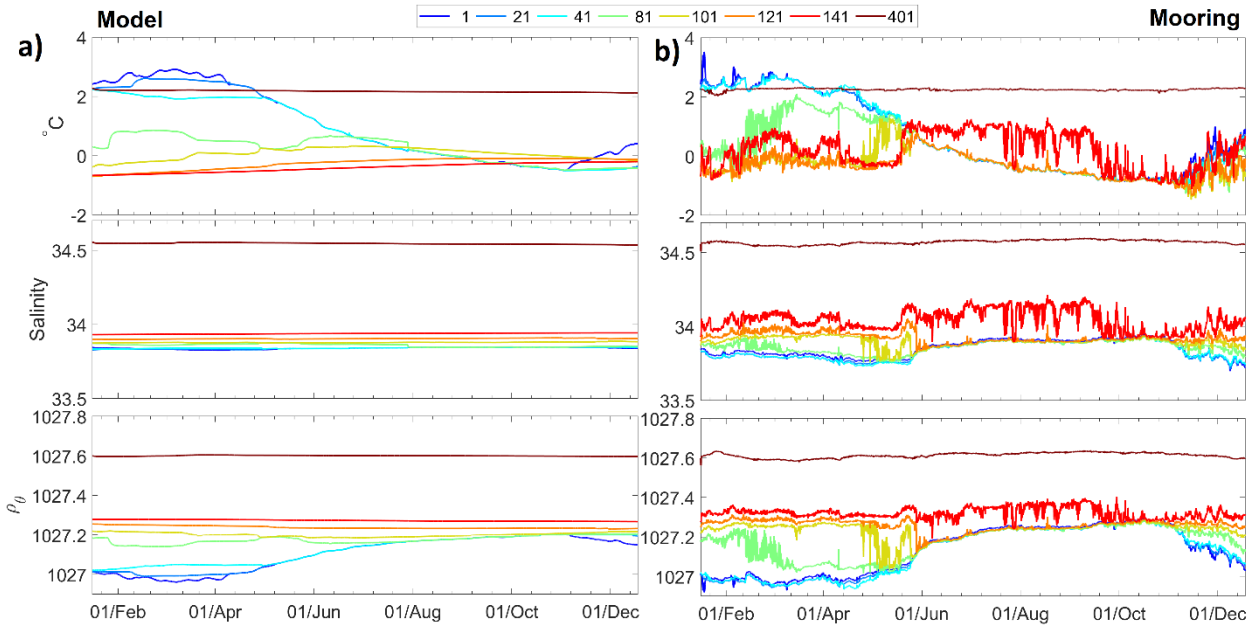

Figure 3.7. Comparison between (a) the model and (b) the mooring sampled time-series of temperature, salinity, and potential density, on the upper left and right panels, respectively. Lines are color-coded according to depth (m), as indicated above the graphs.

The model could realistically explain the long-period surface-temperature variability, where a normalized cross-correlation gave a coefficient value of r = 0.94 for the surface and a mean of 0.85 for the top 100 m of the water column. However, the

agreement of the model was significantly reduced in layers deeper than 120 m, where the local changes in net heat flux were not sufficient to explain the winter variability found in the temperature and salinity profiles. A comparison between the mooring data and model results is shown in Figure 3.7**,** and the difference between the two (X) is displayed in Figure 3.8. At these depths, frontal advection and meandering of the ACC were the most significant factors of non-local variability and were responsible for the 150 m layer presenting an upward trend of temperature and salinity during winter, while all layers above it displayed a downward trend due to surface cooling. At the 75 and 100-m depth layers, differences between model and observations were due to the passage of near-inertial internal waves, which extended the MLD to these depths on Feb 13th and May 7th, respectively, i.e., almost two months earlier than the mixing time of the model experiment, on April 2nd and July 21st.

While the upper-layer temperature data agreed well with the model, the local salinity variation as produced by the model did not adequately capture the observed salinity variation (i.e., r=0.69). Although the general annual salinity trend was preserved, the most significant salinity changes were related to horizontal variability; caused by the formation or melting of sea ice and/or changes in the zonal extension of the frontal structure at the location, which is forced predominantly by wind in the upper 82 m but seem to be more related to the absolute dynamic topography (ADT) variability at deeper layers.

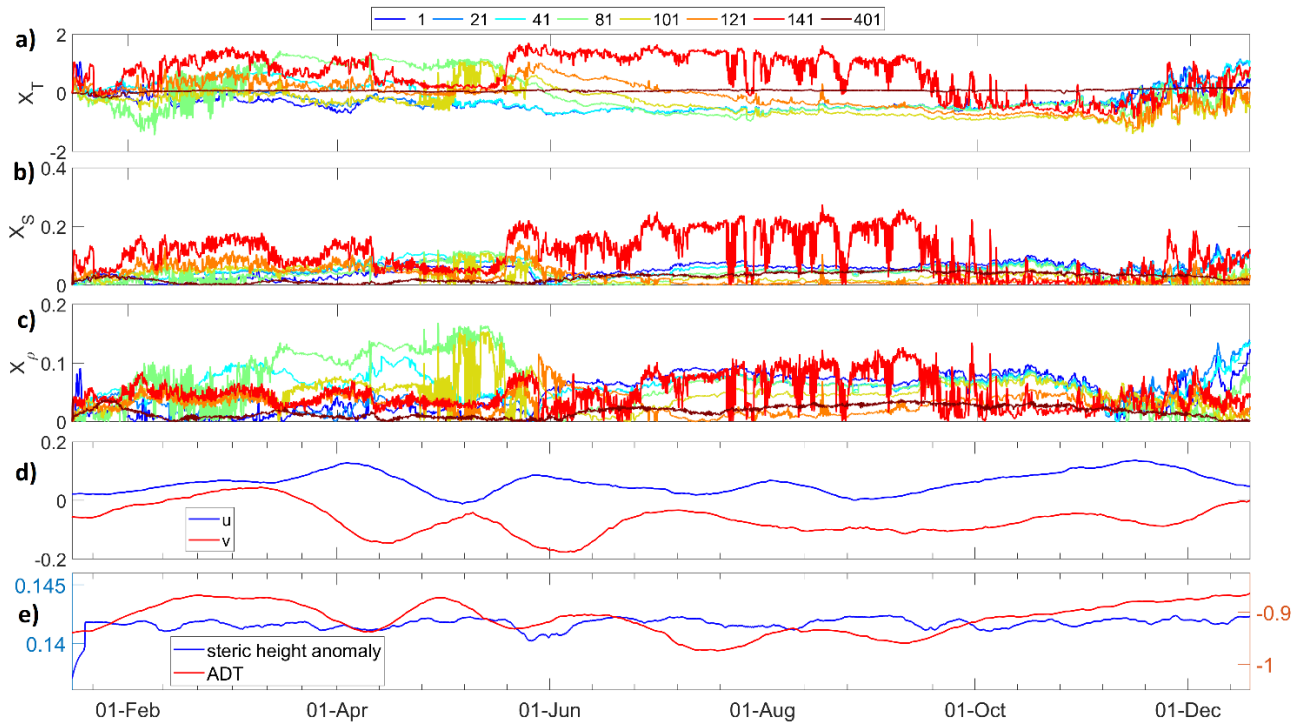

Figure 3.8. Lateral advection components for (a) temperature, (b) salinity, and (c) density; (d) zonal and meridional component of the geostrophic velocity calculated from ADCP data at the mooring point; and (e) ADT and steric height anomaly (m) calculated from mooring data as the pressure integral of specific volume anomaly.

Possible sources of horizontal advection of temperature and salinity at deeper layers could be traced by analyzing the ADT and deriving geostrophic current velocity fields from the merged SSALTO/DUACS altimetry dataset (see section 3.2) cross-referencing them to SST. In this way, the main events of horizontal advection affecting these layers could be visualized as frontal shifts and temporal variations of nearby meanders. From these events, the most likely source of deviation from the model at the end of May is shown in Figure 3.9. The mooring is shown to be between a cold-core long-standing cyclonic eddy in the southwest and a warm-core anti-cyclonic eddy in the northeast.

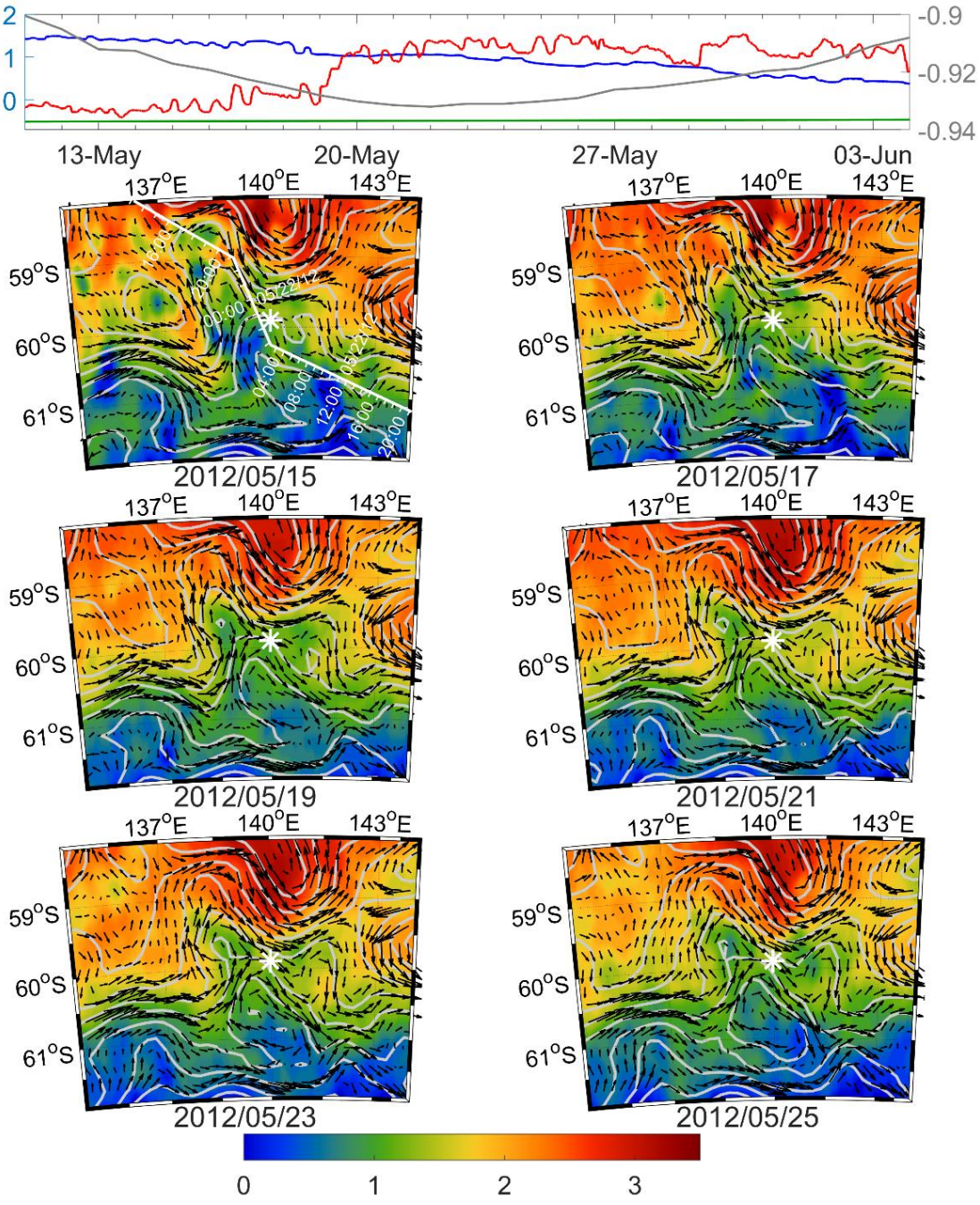

Figure 3.9. Satellite confirmation of the period of high estimated advection from the model which starts on May 21st. The red, blue, green, and gray lines in the upper panel represent advection contribution to temperature at 150 m depth, temperature at the surface, model-estimated 150-m depth temperature (°C, left axis), and ADT (m, right axis), respectively. The color bar in the surface maps indicate SST, the gray contours indicate ADT, and the arrows represent the geostrophic velocity. On the first surface map, the passage of the most significant cyclonic storm is shown as a white line.

3.6 Discussion and conclusion

The results constitute one of the few open ocean long term observations in the Southern Ocean. Although limited by vertical resolution of the mooring, local and advective contributions to mixed layer variability could be derived, introducing new questions about the additional forcing necessary to drive the observed seasonal variability in the region.

The diffusivity parameters K_ρ, K_T, and K_S were observed to increase above the background levels by about two orders of magnitude during the two periods where near inertial oscillations of density were detected. During these periods, mixing was found to be predominantly turbulent, and the MLD increased by 20 m over 20 days. Vertical energy transport was also observed between February 12th and March 17th, i.e., the first period where NIWs were observed. Comparing our estimation of MLD with the energy integrated over the near-inertial frequency band, as much as about 40% (i.e., 12.1 J m^{-3}) of the energy could reach deeper than the MLD, in agreement with Johnston and Rudnick (2009) who showed that momentum travels deeper than the MLD, suggesting a possible pathway for deeper penetration of surface variability.

These results provide a new dimension for studies on the impact of wind intensification in the Southern Ocean, such as that by Hogg et al. (2017), who demonstrated that stronger westerly winds increase the energy available for internal wave mixing. The present study shows that enhanced internal wave mixing likely increases the diffusivities of temperature and salinity, and these increases are capable of penetrating deeper than the mixed layer. In such scenarios, it is likely

that communication between the upper and middle layers of the Southern Ocean increases.

Owing to the high horizontal NIW propagation, enhanced mixing could also affect regions where ice cover prevents direct wind interaction. This interaction might be modulated further by the increased stratification due to warming surface waters and freshwater fluxes, which modulate this communication since a higher stratification implies in NIWs reaching further horizontally at the expense of vertical range.

Diffusive convection was observed throughout the year at 125 m depth (Figure 3.6), although it became less significant in winter. The diffusive convection mechanism might be important in exchanging heat and salinity between the cold remnant winter waters and the relatively warmer waters below, and likely creates convective cells below the mixed layer between 150 and 200 m depth. Future high-resolution measurements would be important for investigating the accurate extension of these cells.

The box model approach could reasonably explain seasonal variability of temperature, while quantifying the influence of horizontal advection on the density balance at 60 °S; however, one of the major differences between model and observations was the behavior of the 75-m deep layer at the time when the internal wave propagation occurred. Although the model incorporated the high diffusivity caused by their passage, it was not enough to explain the sudden density decrease, indicating that another forcing is needed for the layer to mix with the surface at the observed scale. Submesoscale processes such as Ekman frontal advection and ML eddy instabilities could possibly provide the buoyancy flux necessary for the earlier MLD increase. Accurately estimating such fluxes proves to be hard from our

mooring since its position also varies on a scale comparable to these processes, but by associating the polar front typical salinity to the observed SST, the maximum submesoscale buoyancy input could be constrained to be on the same order of magnitude as the surface buoyancy flux when the front is at is closest to the mooring position. This situation likely occurs during the Autumn and Spring (the latter observed by du Plessis et al., 2019). Another finding is the importance of non-local forcing to the 150-m layer. Since the MLD was observed to extend below this depth between September and November, eddy instabilities are likely to be the major forcing on the lower ML boundary during the beginning of spring restratification. If on one hand, subsurface eddies and meanders are responsible for variability at 150-m, on the other hand this forcing is also present to some degree in the surface layer. Thus, winter air-sea fluxes can smooth out the surface horizontal gradients faster than mesoscale and submesoscale eddies can advect them.

At intermediate depths of about 400 m, although the variations were of a smaller scale, model and mooring data presented significant differences. The model indicated a lightening tendency of -2.468×10^{-7} kg m^{-3} per day, caused by a salinity freshening trend of -7.512×10^{-5} psu per day, starting from February 26th. Conversely, sampled data from the mooring, had the opposite tendency to become heavier and saltier at the same depth, with rates of $+7.222 \times 10^{-5}$ $\mathrm{kg\,m^{-3}}$ and $+8.746 \times 10^{-5}$ psu per day, respectively, implying that a mean of 1.626×10^{-4} per day was provided by lateral advection to maintain the observed values.

Our results corroborate those of Dong et al. (2007), as the wind was found to be the primary forcing of surface currents, as shown in Figure 3.10, where events of enhanced oceanic advection were also related to the passage of cyclonic storms. The noise-free current data presented a $\mathrm{r} = 0.75$ correlation with wind speed at 6 m

depth, i.e., a quantity that remains relatively constant until 82 m depth and decays quickly below that.

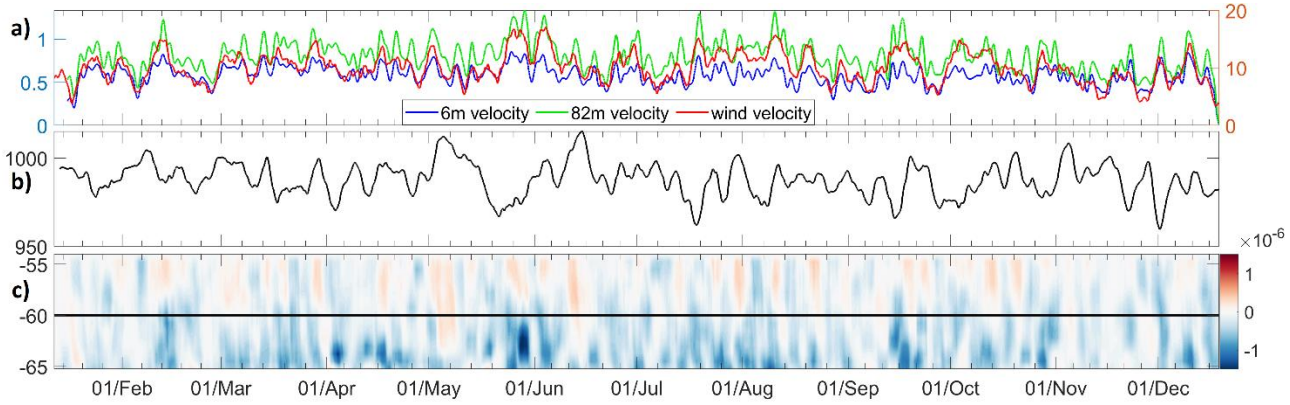

Figure 3.10. (a) Comparison of current speed and wind velocity time series (m s^{-1}), (b) atmospheric pressure (hPa), and (c) the Hovmoller diagram of zonally integrated wind stress curl (N m^3), where the Y axis represents latitude, and the black line indicates mooring latitude.

The shift in position and strength of the ACC eddies and meanders exhibited considerable correlation with the estimated non-local temperature component, particularly at 150 m depth (Figure 3.11). The figure shows the peaks of both negative and positive significant correlations. We consider it to be explained by the cyclonic and anti-cyclonic longstanding eddy advection of cold and warm water, respectively, toward the mooring site. Although these results indicate a possible pathway for warm water intrusion at the mooring position, it is clear that a study dedicated on this matter is necessary to confirm and quantify the dynamics proposed above.

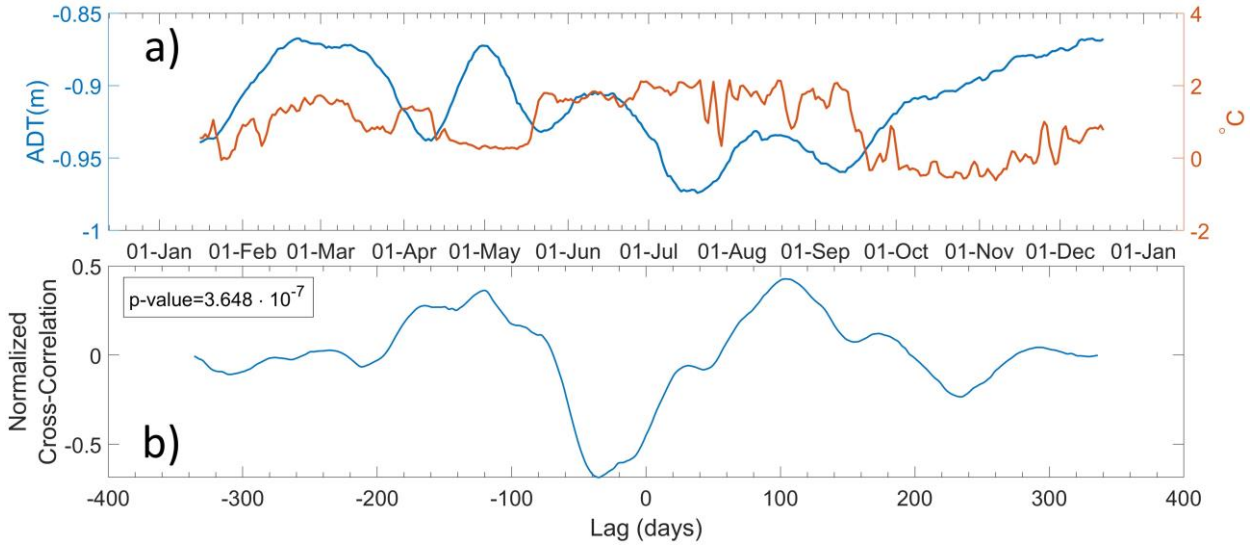

Figure 3.11. (a) Time series of ADT (meters, blue) and 150-m X_T (°C, red), and the cross correlation between them (b). The highest correlation of -0.649 is found at -25.2 days.

In conclusion, the surface mooring system clearly revealed the evolution of heat and freshwater exchange processes at the surface, the enhancement of diffusivity caused by the passage of internal waves, and the importance of lateral advection below 82 m depth. We observed the penetration range of the convection caused by heat loss at the surface, and we concluded that, although it was the most significant factor for the winter MLD increase and related to the concentration of energy at the base of the mixed layer, it was not enough to reproduce the observed variations.

These results contribute to mixed layer studies identifying the biggest contributing factors influencing the upper layer and quantify both the penetration range of the convection caused by heat loss at the surface and the importance of the zonal influx of water at deeper layers causing variability of physical properties below 150 m depth. The significant role of horizontal advection clarified in this study corroborates with Mizobata et al. (2020) regarding the existence of a relationship between eddy

intensification and deep-water transport across the shelf, even though their region of interest was 15–35° west of the mooring. This similarity invites further studies to comprehend this relationship.

Chapter 4: The oceanic surface heat loss as a mechanism of internal wave generation on the Southern Ocean.

4.1 Introduction

The ocean at high latitudes is unique in that its superficial layer loses heat to the atmosphere during considerable part of the year. This buoyancy forcing causes the water column to become hydrostatically unstable. As such, open ocean convection is thought to commonly occur in high-latitude oceans (Sohail et al., 2020) and the vertical mixing leads to the homogenization of the surface layer, thus increasing mixed layer depth (MLD) (Marshall & Schott, 1999). Open-ocean convection is particularly important in the Southern Ocean as it modulates the properties of the downwelling branch of the global meridional overturning circulation (AMOC) (Talley, 1999; Danabasoglu et al., 2012), Antarctic Bottom Water (AABW) formation in polynyas such as the Weddel Sea (Jena et al., 2019; Kurtakoti et al., 2018; Cheon et al., 2015), and facilitates deep convection (Heuzé et al., 2015).

In spite of such importance, profound understanding of open ocean convection is limited in the Southern Ocean by its harsh environmental conditions; continuous measurement methods such as moorings have a hard time covering surface and subsurface data since ice coverage and travelling icebergs are hazardous to the mooring's sensors.

As such, the role of penetrative convection in the Southern Ocean mixed layer dynamics is still poorly understood despite being of crucial importance for the improvement of ocean circulation models of both global and regional scale. The diurnal cycle is often omitted from numerical ocean models to decrease computational cost but replacing the convective pulse with time-averaged buoyancy

forcing causes underestimates of the deepness of the mixed layer (Soloviev and Klinger, 2008). Furthermore, much of our knowledge on this phenomenon in the ocean is still based on the analogy between atmospheric and oceanic boundary layers and on laboratory studies (Soloviev and Klinger, 2008).

Taking into account the importance of open ocean convection to further our understanding of the Southern Ocean, we set up a mooring in the Indian sector of the Southern Ocean to investigate the relation between the surface heat flux, the generation of shear and turbulence in the mixed layer and how the energy generated organizes in the time-frequency domain.

The importance of this study lies in the possibility these high-latitude processes might modulate the interaction between the atmosphere, the mixed layer, and the deep ocean, thus being key elements to understanding the effects of climate change on high-latitude oceans, since its anthropogenic component is forced at the atmosphere. Of no less importance, Shimada et al. (2022) found robust evidence of AABW freshening in the Eastern Indian sector of the Southern Ocean, decreasing its density and reducing supply, but the causes are still not well understood, so understanding how the upper layer might interact with the deep ocean might help elucidate bottom variability.

4.2 Methods

A triangle trans-ocean buoy network (m-TRITON) mooring was deployed in January 2012 as part of the KARE-17 expedition onboard the TR/V Umitaka-maru. Although the top buoy was set at the surface equipped with atmospheric sensors, data collection was only successful for surface pressure, downward shortwave radiation,

and precipitation. The mooring recorded data at 60 °S and 140 °E over 11 months between January 15th and December 19th, 2012, and additional high-resolution CTD rosette casts were done at the time of mooring deployment and retrieval. Details of deployment and sampling are given by (Ferreira Azevedo et al., 2022) while data is available at the databases maintained by Ferreira Azevedo and Aoki (2022a, 2022b).

We compare current, temperature and salinity data from the mooring along with the estimates of wind and heat flux obtained from the ERA5 reanalysis output. Net heat flux is estimated from the sum $Q_{net} = Q_{SW}(1-\alpha)+Q_{LW} + Q_L + Q_S$, where the subscripts SW, LW, L, and S are the short-wave incoming radiation, long wave outgoing radiation, latent and sensible fluxes, respectively, and α is the albedo of sea water. Fluxes are oriented so that in our notation a positive Q_{net} indicates upward flux (ocean loses heat to the atmosphere). Vertical shear is discretized using a centered differentiation scheme and wind stress was parametrized using its frictional velocity (V^*, m s^{-1}).

4.2.1 Continuous wavelet analysis

Utilizing the jLab (Lilly, 2021) MATLAB package we conduct a continuous wavelet transform of the meridional (v) and zonal (u) components of current velocity by expressing them in the complex domain as $u + i\mathrm{v}$. The wavelets are constructed from an analytic morse mother wavelet ψ defined in the frequency (ω) domain by Equation 4.1, where β, γ are the waveform control parameters, $a_{\beta,\gamma}$ is a normalization constant and $U(\omega)$ is the Heaviside step function.

$$\psi_{\beta,\gamma}(\omega) = \int_{-\infty}^{\infty} \psi_{\beta,\gamma}(t) e^{-i\omega t}\, dt = U(\omega) a_{\beta,\gamma}\, \omega^{\beta} e^{-i\omega\gamma} \tag{4.1}$$

To clarify, an analytic wavelet is a complex wavelet which has zero expression in frequency space for any negative frequency, thus having a singularly defined phase signal.

The current velocity can then be expressed in terms of both time and frequency by its continuous wavelet transform (CWT)

$$W_{\psi}(t,s) = \int_{-\infty}^{\infty} \frac{1}{s^{n}} \psi^{*}\left(\frac{\mathrm{T}-t}{s}\right) x(\mathrm{T}) d\mathrm{T}, \tag{4.2}$$

where s and T are the scale and translation parameters, respectively.

After numerous tests we set β and γ to 3 and 5, respectively. This choice is made to realize high time-expression accuracy in separating the diurnal, inertial and low (≤ 8 hour) periods. The accuracy of the method is tested by comparing a 24-hour period sine pulse (Figure 4.1a) against its time-frequency domain representation (Figure 4.1b). Less than 10% of the energy spills over the 12-hour frequency and most of the spill is seen to occur at the start and end of the pulse, which is caused by the boundary having undefined derivatives at the discontinuity. Since this is a purely numerical artifact, we thought reasonable to assume this inaccuracy to be absent from real observations.

The resulting wavelet families are both invertible and conserve phase information when doing so. Therefore, we are able to recompose the time-series f(t) expression

in a specific spectral band of interest defined to be given by the scale function $s_1 < s < s_2$ by taking the inverse wavelet transform:

$$f(t) = \frac{1}{C_\psi} \int_{s_1}^{s_2} \int_{\mathrm{T}}^{\infty} < f(t), \psi_{s,\mathrm{T}}(t) > \psi_{s,\mathrm{T}}(t) d\mathrm{T} \, \frac{ds}{s^2}, \qquad (4.3)$$

where $C_\psi = \int_{-\infty}^{\infty} \frac{|\psi(\omega)|^2}{|\omega|} d\omega < \infty$ is the wavelet admissibility condition and $\psi_{s,\mathrm{T}}(t) = \frac{1}{a}\psi\left(\frac{t-\mathrm{T}}{a}\right)$ is the time domain expression of the mother wavelet $\psi_{\beta,\gamma}$. The inverse wavelet transform can be rewritten in a single integral by recognizing that a two-wavelet admissibility condition can be satisfied even if one of the wavelets is not admissible. The requirements can be further relaxed by allowing one of the functions to be a distribution such as the Dirac delta function δ. A detailed explanation of the theory is given by Lilly (2012), and the inverse transform simplifies to

$$f(t) = 2\mathbb{R}\left\{\frac{1}{C_{\psi,\delta}} \int_{s_1}^{s_2} < f(t), \psi_{s,\mathrm{T}}(t) > \frac{ds}{s}\right\}, \qquad (4.4)$$

where $\mathbb{R}$ denotes the real part of the expression.

In practical terms, Equation 4.4 means that the signal can be reconstructed into its frequency-localized time-series by summing the scaled CWT coefficients over all desired scales.

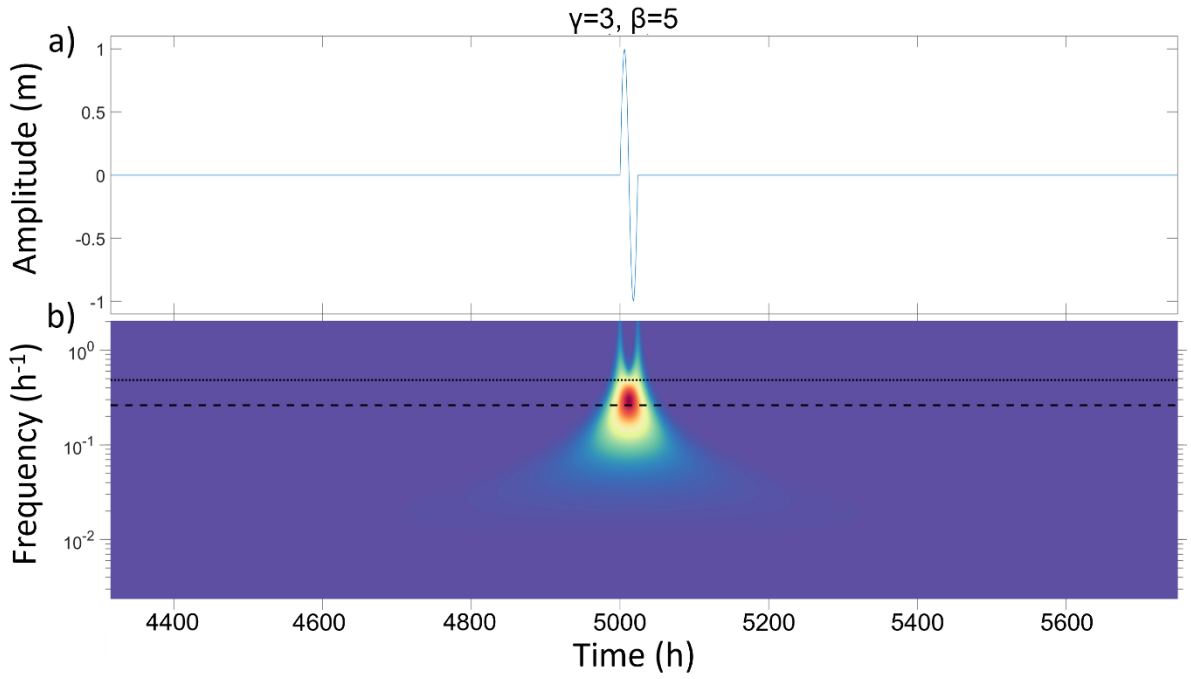

Figure 4.1. Expression of a 24h period pulse in (a) time-amplitude space and time-frequency space (b). The thick black line in b indicates the 24-hour period while the dotted line marks the 12-hour period.

4.2.2 Damped slab model

The band passed velocity data is compared to inertial velocity estimates from a damped slab model, as proposed by Pollard and Millard (1970) and further discussed by D'Asaro (1985). The model, described in Equation 4.5, relates the velocity components u and v, water density ρ, Coriolis frequency *f*, mixed layer thickness H to wind stress $\tau_{(x,y)}$, taken from the ERA5 reanalysis output, , and a dampening constant r, which gives the scale of energy dissipation.

$$\begin{cases} \dfrac{du}{dt} - fv = \dfrac{\tau_x}{H_\rho} - ru \\ \dfrac{dv}{dt} + fu = \dfrac{\tau_y}{H_\rho} - rv \end{cases} \tag{4.5}$$

Expressing u and v in a complex notation $Z = u + iv$,$T = (\tau_x + i\tau_x)/\rho$, and $\lambda = r + if$, then a single expression is reached:

$$\frac{dZ}{dt} + \lambda Z = \frac{T}{H} \tag{4.6}$$

While the simple cases of $T = 0$ and constant T give a damped inertial solution ($Z = Z_0 e^{-ift-rt}$) and the Ekman solution ($Z_E = T/(\lambda H)$), respectively, for any intermediate solution, the inertial component is given by subtracting the Ekman component from the total $Z_I = Z - Z_E$ so

$$\frac{dZ_I}{dt} + \lambda Z_I = -\frac{Z_E}{dt} = -\frac{d(T/H)}{dt}\frac{1}{\lambda} \tag{4.7}$$

$$= \frac{dT}{dt}\frac{1}{\lambda H} - \frac{d(1/H)}{dt}\frac{T}{\lambda}$$

The model was calibrated against the current time-series estimated in-situ using the minimum root mean square error (RMSE) to compare both estimates. The lowest RMSE is found when the thickness of the wind active layer is set to 20 m and r is set to 6 days.

4.3 Results

4.3.1 Energy distribution in the mixed layer

The near-inertial spectral band of velocity was isolated through analysis of current rotary power spectra using the multi-taper method first proposed by Thomson (1982), using seven tapers (i.e., 14 degrees of freedom) and a time-bandwidth product of four. This configuration provides enough frequency resolution to distinguish between the near-inertial and semidiurnal tidal bands. The method has been described in detail by Percival and Walden (1993), and algorithms incorporating modern theory are freely available within the jLab spectral package (Lilly, 2021). From the power spectral density, energy was integrated over the range of $0.90–1.15f$ to account for the modulation of effective inertial frequency by the passage of eddies.

A spectral profile was obtained for each month, and significant seasonal differences are clearly found both in the frequency domain and in the vertical structure of the energy distribution. The most striking seasonal differences are illustrated in Figure 4.2 for summer (Figures 4.2a and d), winter (Figures 4.2b and e)**,** and spring (Figures 4.6c and f).

During summer (Figures 4.2a and d), energy was observed to be predominantly in the near-inertial band with peaks around 15 to 25 m depth. Energy content does not change significantly until close to the base of the mixed layer at ~80 m depth, where a sharp decrease occurs, and with 95% confidence interval, $[21.83 – 31.30]$ J m^{-3} were estimated to leave the inertial band between 66 and 82 m depth.

During winter (Figure 4.2b and e), energy increased significantly at around 80 m deep, namely, the maximum shear depth, while remaining relatively low closer to the

surface. The energy increase coincided with the maximum shear layer depth, while the mean MLD was 150m. A seasonal frequency shift toward the diurnal band was also identified, and while comparable to the semi-diurnal energy content at the first 50 m below the surface, it becomes strikingly pronounced and the most energetic band below 60 m depth, as can be seen in Figure 4.2b. The near-inertial band energy became significant again below 80 m, but with a broader peak which also included the semidiurnal tide harmonics. During spring (Figures 4.2c and f) and autumn, an intermediate pattern was observed, where energy was dominant in the near-inertial band but more evenly distributed along the upper layer. A possible explanation is the larger variance of the MLD during these periods.

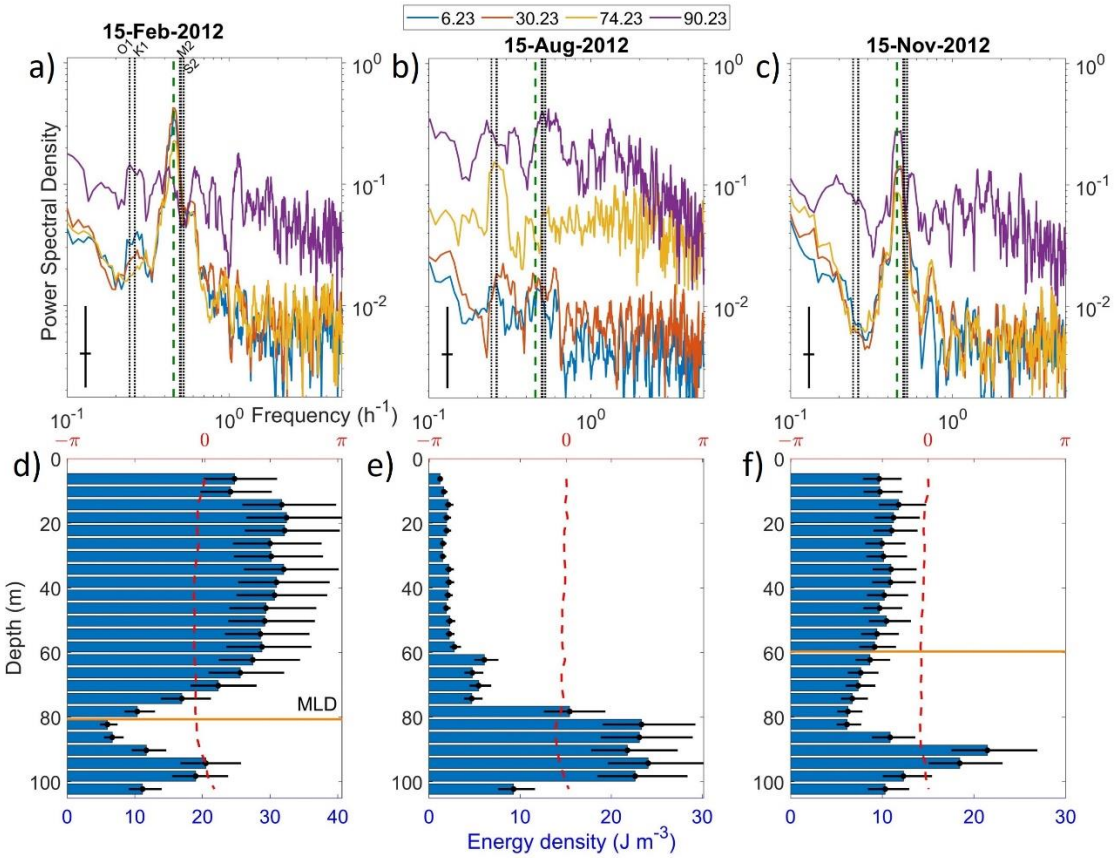

Figure 4.2. Positive (i.e., counterclockwise) monthly rotary spectra of current velocity starting on the date indicated above (a), (b), and (c), as representatives of summer, winter, and spring patterns, respectively. The inertial frequency is indicated with a green dashed line and the most significant tidal frequencies are indicated by black dotted lines. 95% confidence interval is shown as a black cross, and depth (m) of the readings is color coded according to the values indicated in the upper panels. (d), (e), and (f) are bar graphs of the energy contained in the inertial frequency band for the respective (a), (b), and (c) periods; the red dashed lines indicate the mean phase shifts from the surface.

4.3.2 Correlation between heat and shear

In Figure 4.3a to d, a comparison between the time-series of the potential density, the near-inertial current velocity, Q_{net}, V^*, and 0-100 m vertically integrated shear is given. Our results indicate that the maximum absolute shear depth (Figure 4.3b) became shallower during the period when heat flux was positive. During the same period, the average V^* was stronger and the MLD became deeper. This offers an exception to the current understanding of the peak shear variance being greater and shallower during summer while being deeper and weaker during winter (Brannigan et al., 2013). The depth of this shear enhancement was calculated as being outside of the mean winter Ekman depth of 47 m, which implies additional factors besides wind are necessary to explain this variability. Peaks of both wind and heat flux (Figure 4.3c) generally coincide with increased shear at the base of the mixed layer and overturning. In the periods where overturning was found, high shear was observed throughout the mixed layer. The cross-correlation of the 100 m integrated vertical shear with V^* and Q_{net} was calculated in 15-day windows with a 30% overlap, where the maximum correlation inside the 15-day window was picked as the representative value for that window and normalized. This procedure generated a time-series with a 5-day temporal resolution (Figure 4.3e). While winds had a significant correlation coefficient with integrated shear throughout the year, during the surface cooling period it is not sufficient to predict it. When $\mathrm{Q_{net}}$ becomes positive, the cross-correlation coefficient between shear and $\mathrm{Q_{net}}$ increases significantly (Figure 4.3e).

Closer inspection of vertical profiles during a typical winter period is given in Figure 4.4. We observed the depth of maximum vertical shear (Figure 4.4d and e) to oscillate primarily with a diurnal period, which was seen to be in phase with Q_{sw}

(Figure 4.4f). Despite the diurnal predominance, semi-diurnal variability was also evident in the vertical shear profile, although on a smaller scale. Surprisingly, further spectral analysis reveals the response of the seawater physical properties shown in Figure 4.4a-c was predominantly semi-diurnal with a higher frequency (>8 hours) component present as well.

This observation brings about an important question: If upper layer near-inertial waves are generated primarily by the wind stress over the ocean surface (Alford et al., 2012), why does our winter observation detect this frequency only below several tens of meters? One possibility is that the NIWs observed during wintertime were not generated locally and travelled towards the mooring point from an origin point in a more stably stratified environment. Coriolis frequency f increases with latitude, so the inertial period becomes smaller. For a buoyancy frequency N, and a latitude degree θ the internal wave dispersion relation $\omega^2 = \mathrm{N}^2\cos^2\theta + f^2\sin^2\theta$ implies no propagation is possible outside $f < \omega < \mathrm{N}$. Since NIWs have, by definition, propagation frequencies very close to *f*, horizontal propagation on NIWs must come from a point further south of the mooring point, but Q_{net} becomes higher at higher latitudes so that the generation problem would remain unsolved.

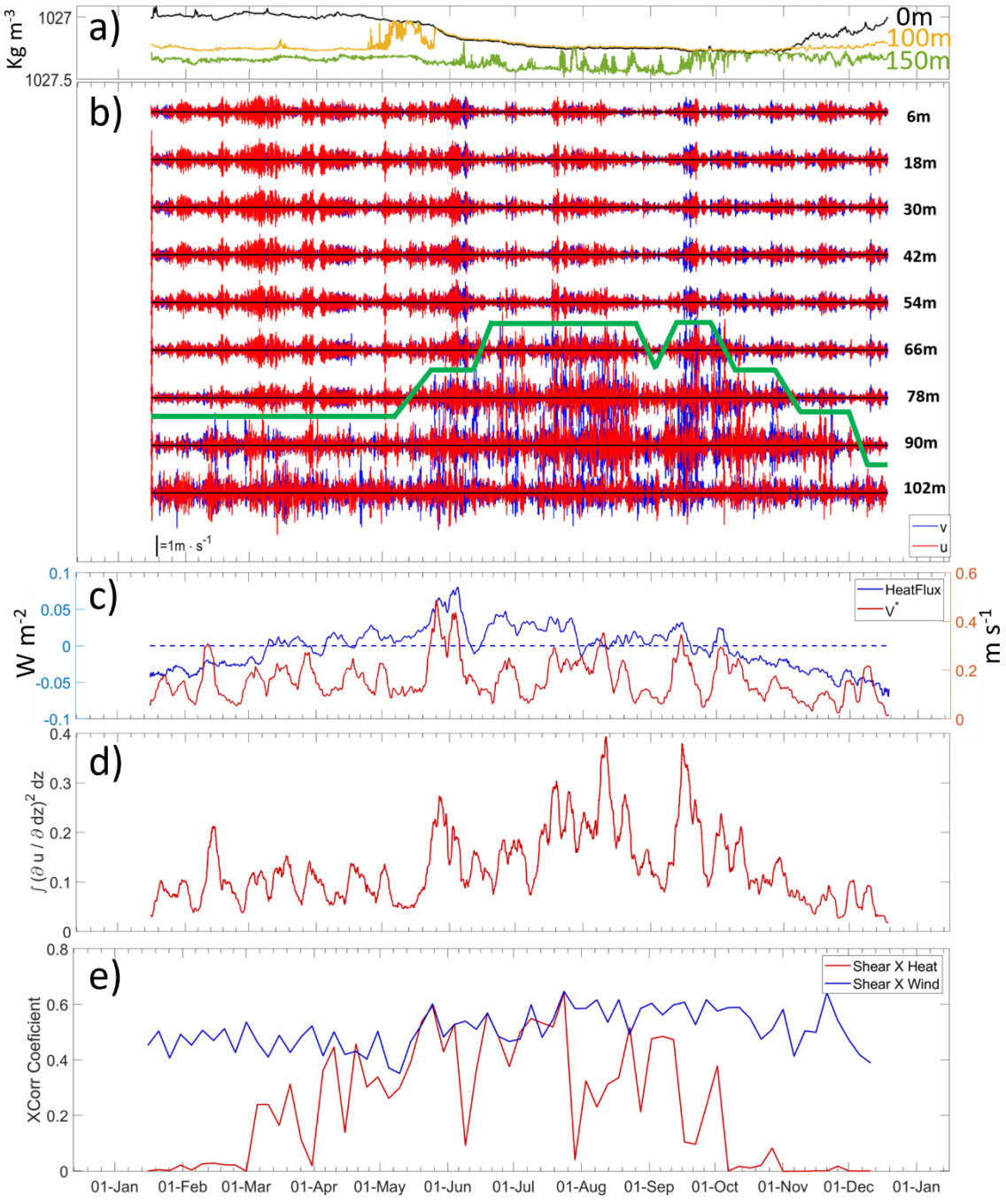

Figure 4.3. Time series of (a) potential density, where the black, orange and green lines represent the surface, 100 and 150 m respectively, (b) inertial band-passed velocity, where the maximum shear layer is indicated by the green line, (c) V* and Q_{net} time series (d) vertically integrated shear across the first 100 m of the water column and (e) cross-correlation coefficient of the vertically integrated shear with Q_{net} and V^*.

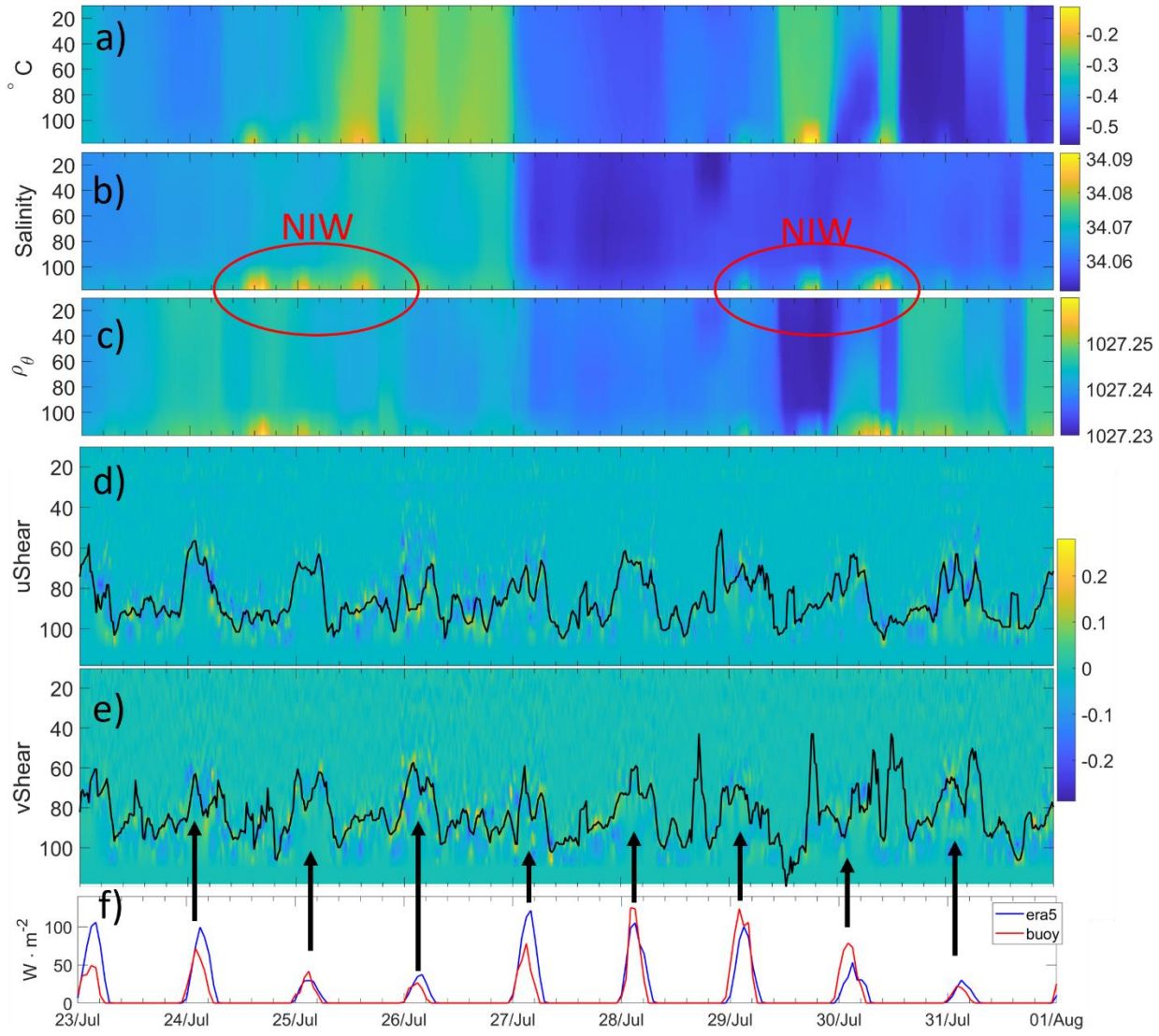

Figure 4.4. Vertical profile of (a) temperature, (b) salinity, (c) potential density, (d) shear's meridional component, (e) shear's zonal component. The black lines in panels d and e indicates the maximum shear depth and a time series of Q_{SW} is provided in (f) for comparison.

Another hypothesis is the local generation of NIWs at the surface by wind friction, as is traditionally assumed, but travelling through an unstable upper layer where $\mathrm{N}^2 < 0$ or $\mathrm{N}^2 \approx 0$ so that energy is only transmitted as evanescent modes until the boundary of the convective depth and/or $N^2 \gg 0$. A first qualitative step to assess this

hypothesis is to construct seasonal stratification profiles, provided in Figure 4.5a, and use them to estimate the ray path of the internal waves for a fixed frequency. The aspect ratio $a = \mathrm{k_H}/\mathrm{m} = \cot\theta$with the horizontal and vertical wavenumbers $\mathrm{k_H}$ and m can be found from the background stratification by rearranging the dispersion relation into $a^2 = (\omega^2 - f^2)/(\mathrm{N}^2 - \omega^2)$. The vertical ray path for a 2D plane is then, under WKB approximation, simply given by $\mathrm{dz}/\mathrm{dx} = a$ and shown in Figure 4.5b.

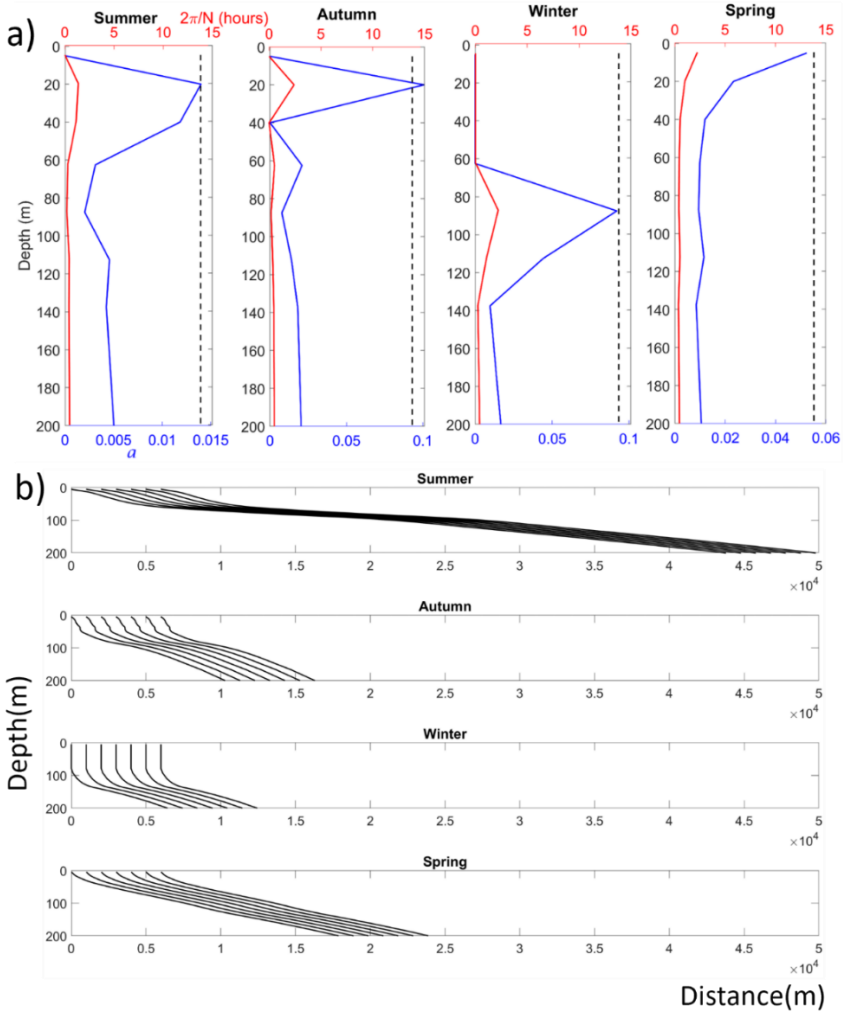

Figure 4.5. (a) Seasonal vertical profile of buoyancy period (red) and aspect ratio (blue). The inertial period $2\pi/f$ is given in hours by the dashed line. The winter profile has no aspect ratio for the first 40m because $2\pi/N \in \Im$. (b) The eastward propagating ray path of an internal wave of 1.15*f* frequency on a x-z plane.

The vertical seasonal profile clarifies how the stronger summer stratification implies in a longer horizontal range of propagation for NIWs, while the winter upper layer instability generates a surprisingly high aspect ratio considering the 1.15*f* wave frequency. On average, the winter upper layer seems to become hydrostatically stable below 60 m deep, corroborating at least qualitatively with the notion of wave energy accumulating between 60 and 140 m deep. This hypothesis , however, does not explain the spectral shift in frequency observed during winter, so a complimentary source is thought to be needed.

4.3.2 Energy variability

Although Figure 4.2 gives a good insight into the seasonal frequency composition of energy, it is also necessary to characterize how this spectrum evolves in frequency-time space. We then produced CWTs of the velocity, temperature, salinity, and density time series for all recorded depths.

The biggest differences in spectral signature were between the surface-10 m and maximum shear depth (86 m on average during winter): While the 10-m CWTs, shown for zonal velocity in Figure 4.6a, show a consistently high signal in the inertial band throughout the year, this band becomes increasingly intermittent at each deeper observation. Meanwhile, below 60 m depth, we observe a striking frequency shift towards both the diurnal period and a 6 to 8 h period band during the winter which becomes stronger until the 86m layer (Figure 4.6b). At these deeper layers the semi-diurnal band becomes especially strong when diurnal and high frequency bands are also strong. This relation suggests a relation between these three bands either by common cause or by any of the bands being generated from a non-linear interaction between the others. However, a common cause for all three bands

seems unlikely, as semi-diurnal forcing, either from wind or tides is not intermittent in nature.

We explored this relation in more detail by inverse wavelet transforming the time series in the inertial, diurnal and 8 h period bands. The resulting time-series for the 86 m depth is given in Figure 4.7a, b, and c, respectively. The inverse CWT indicates that at the 86 m depth, all three frequency bands became significantly more energetic at the same time during winter. Furthermore, peaks in one band often correspond to peaks in the other bands, albeit with different relaxation periods.

To complement our analysis, we compared the near-inertial component of the current velocity from the mooring (Figure 4.8a) with the velocity output from the damped slab model (Figure 4.8b) described in section 4.2.2. Although the slab model is too simple to capture the dynamics of the Southern Ocean, qualitative comparation still provides valuable insight: Many excitation events are common to both series, and the slab assumption of wind-excited NIWs explains a significant amount of the oscillations present in the mooring series. The squared difference between the mooring and the slab model near-inertial response (Figure 4.8c) quantify this difference, which was observed to be generally higher during the winter season. Our comparison was done after selecting mooring depth for maximum correlation (50 m), and the difference was calculated after phase-shifting the slab model response by -62 h to account for the lag between the two series, thus allowing maximum correlation between the two. However, some of the near-inertial oscillations observed at the mooring station were not present in the slab model, particularly during the winter season, indicating that wind forcing alone is not enough to produce the observed series.

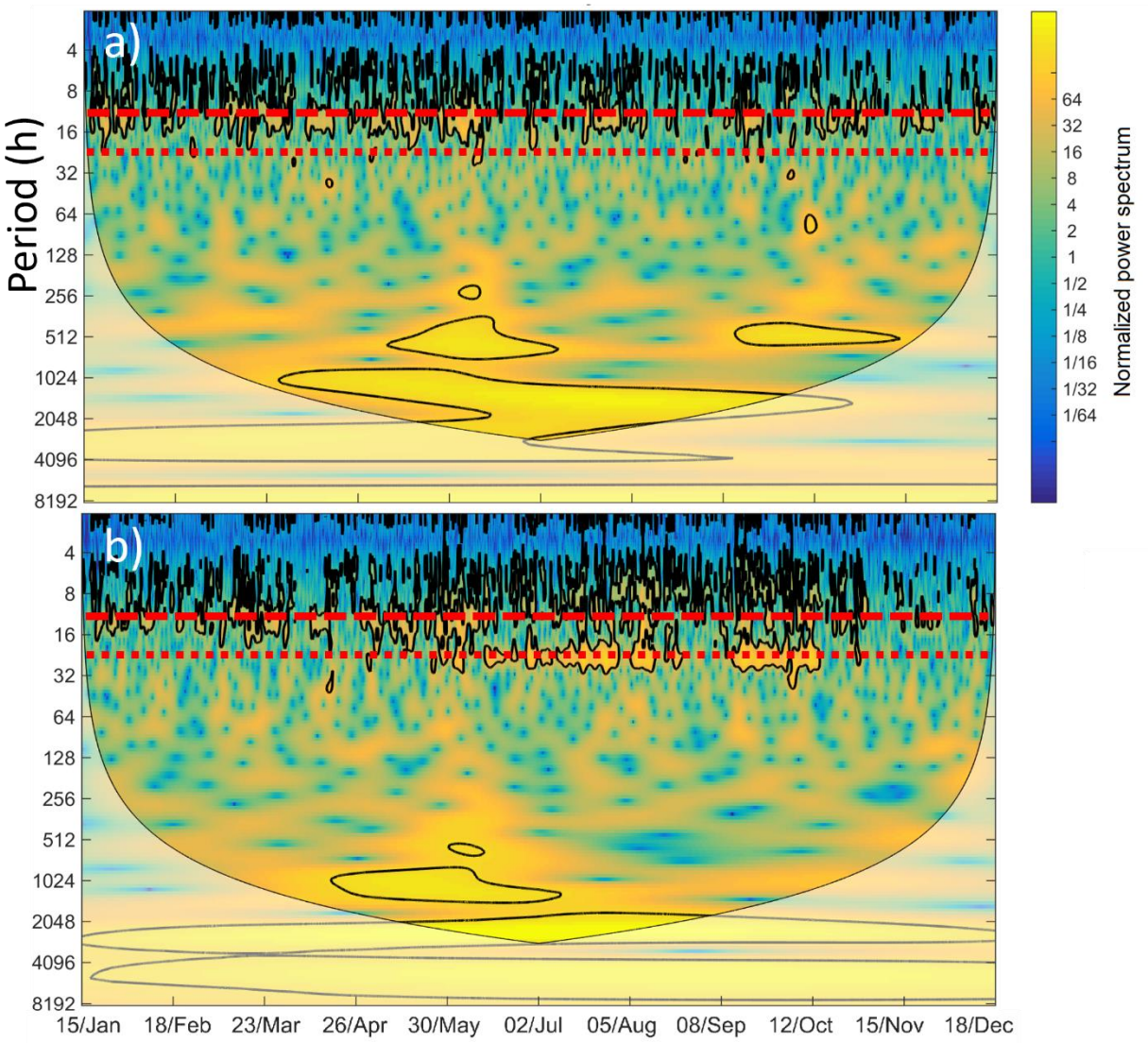

Figure 4.6. Continuous wavelet analysis of the zonal component of high-pass filtered velocity (long period has been extracted) for 10 m deep (a) and 86 m deep (b). The dashed red line indicates the inertial period, and the dotted red line indicates the diurnal period.

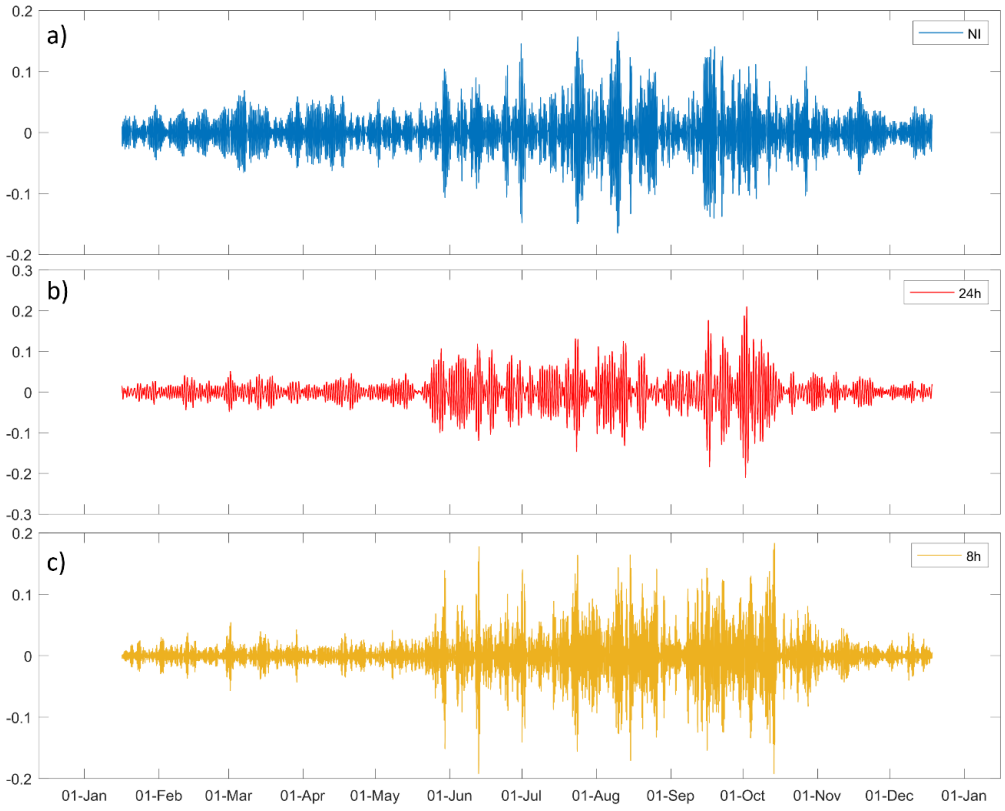

Figure 4.7. Inverse CWT derived current velocity, in m s^{-1}, for (a) the inertial band, (b) the diurnal band, and (c) the 8h period band at 82 m deep.

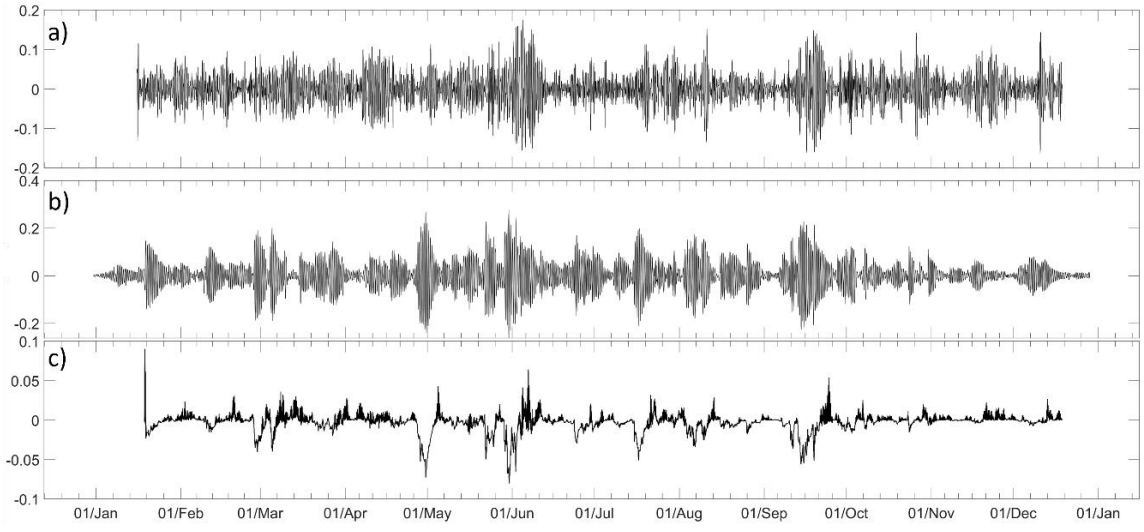

Figure 4.8. Comparison of the time-series of (a) inertial-band mooring meridional velocity at 50 m depth, (b) slab model-derived meridional velocity (m s^{-1}) and (c) the squared difference between them, after phase-shifting the slab model for maximum correlation.

4.3.4 On internal wave propagation boundaries under weakly stratified conditions

The presence of a weakly stratified layer at the base of the mixed layer in the Southern Ocean significantly alters both the energy transfer from the wind, vertical distribution of momentum and the penetration depth of wind-derived energy (Kilbourne & Girton, 2015). Instead of the usual Levitus criterium of a 0.125 kg m^{-3} from the surface, the CTD and raw mooring data better agreed with an estimation of a mixed layer based on a fine-density-threshold criterion of 0.005 kg m^{-3} , which is showcased in the Fig. 4.9, on the upper and lower panels respectively. Another estimate was done individually for each season by linearly interpolating density values into a 1m grid and rounding values to the nearest 0.001 kg m^{-3} to remove instrumental noise. At this new estimate, the best threshold values for determining the start of the weakly stratified layer were observed to be of 0.017, 0.015, 0.007 and 0.039 kg m^{-3} for summer, autumn, winter, and spring, respectively. Weakly stratified mixed layers were observed throughout all seasons, being especially prominent in the spring, where a gentle increase is observed up to 120m, where the change in stratification pattern is not as pronounced as in other seasons and as a result the difference in MLD estimate is the highest, from 50m using the fine-density-threshold to 170m using the traditional Levitus criterium, a 29.41% depth difference. The presence of a weakly stratified layer was shown to limit the downward wind energy penetration when the mixed layer is deeper, while also adding the dynamics of responding to internal waves more easily than a strongly stratified counterpart (i.e. a slab model assumption). A comparison can be seen between MLD and internal wave oscillations on Figure 4.10, where it is shown that at the first mixed layer deepening event, most of the internal oscillations are able to penetrate the fine

density threshold, being observed on the deeper and more stable boundary. However, as winter approaches and the mixed layer becomes deeper, most of the inertial period energy is seen dispersed at the fine density boundary instead.

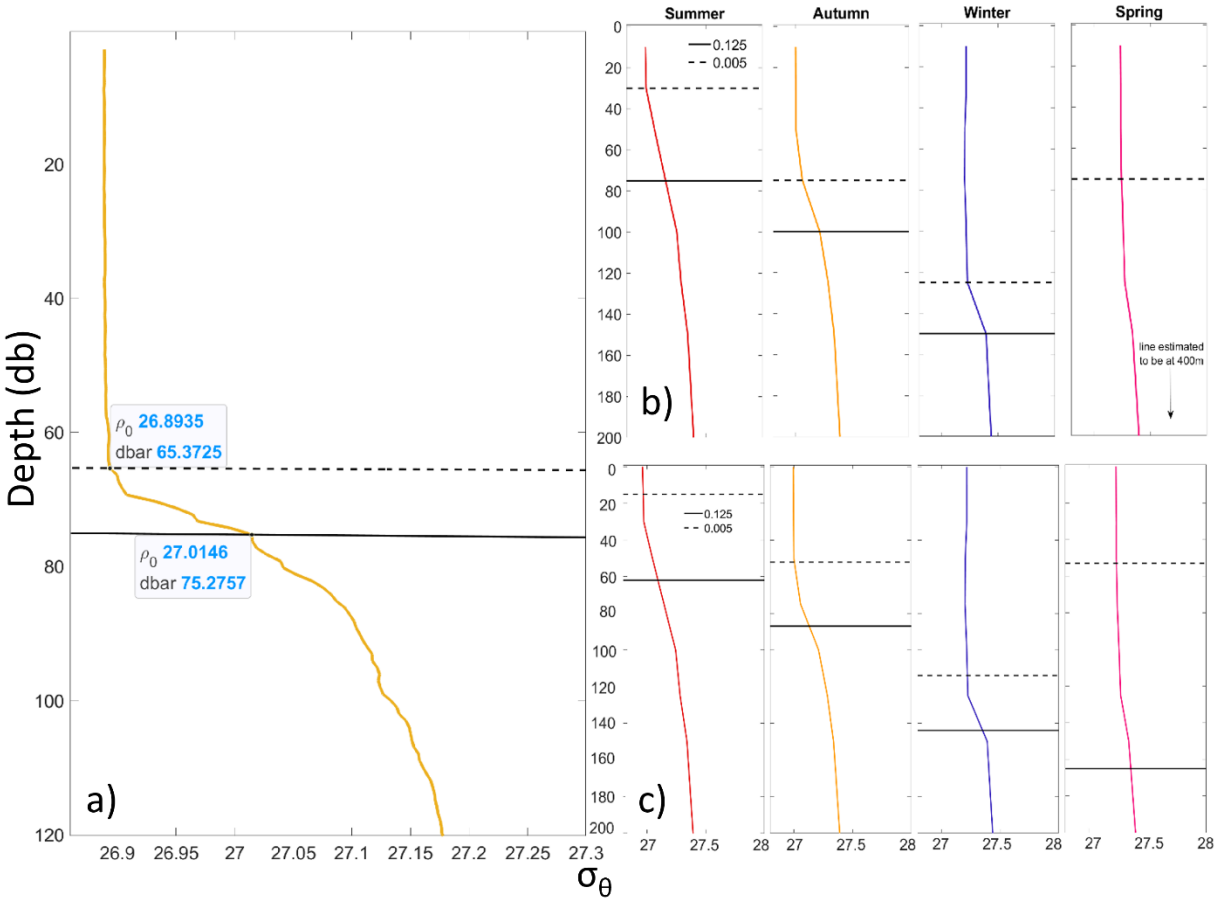

Figure 4.9. Vertical profiles of σ_θ (kg m^{-3}) by depth (m), the CTD cast in January is shown in (A) while seasonal σ_θ mean is shown in (B) and the seasonal mean of the 1 m interpolated grid of σ_θ is depicted on (C).

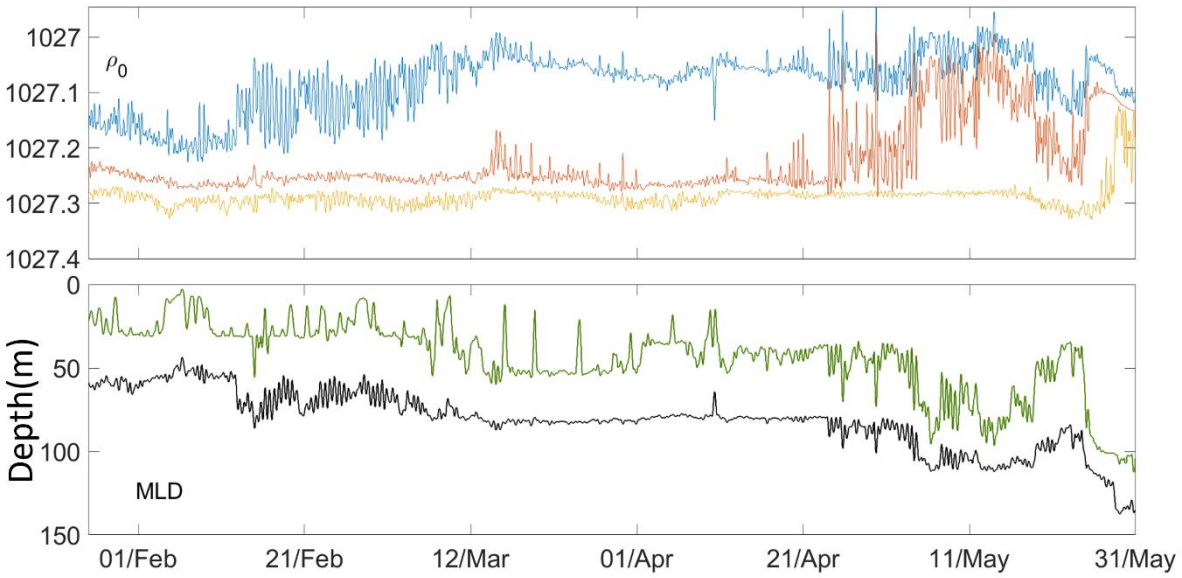

Figure 4.10. Comparison between ρ_θ (upper panel) and MLD (lower panel), calculated from the Levitus criterium (black) and the fine-density threshold (green). The high variability of the fine-density threshold can be observed throughout the year and becomes increasingly expressive during winter.

An important question to address is how the Southern Ocean's weakly stratified conditions modify internal wave dispersion. Most of the oceanographic theory employs the $\vec{f} \rightarrow f$ approximation, meaning the component of the Coriolis force proportional to the cosine of the latitude is disregarded. This approximation is thought to be reasonable since the terms proportional to the cosine of the latitude act in the vertical axis, contraposing the force of gravity. Therefore, strong vertical stratification inhibits the effect of the non-traditional terms as the reduced gravity $g' = g\Delta\rho/\rho_0$ becomes stronger. However, the validity of this approximation has been called into question in areas such as equatorial dynamics, deep convection, Ekman layers and internal waves (Gerkema et al., 2008).

Gerkerma and Exarchou (2008), showed that the non-traditional terms can be neglected if $N \gg 2\Omega$, where Ω is the Earth's angular velocity. This condition is notably not satisfied either at the deepest layers of the ocean or at high latitude sub-surface. LeBlond and Mysak (1978) showed that including the Coriolis cosine terms allows for an extended range of internal waves to propagate, higher than N and lower than f.

4.4 Discussion

We present high temporal resolution mooring data of temperature, salinity, pressure, and velocity and compare it ERA5 reanalysis output to find significant (> 0.6) correlation between heat flux and shear when the net heat flux points towards the atmosphere. We also find the spectral signature of shear and velocity to have significant near-inertial components, despite its diurnal forcing. The significance of these results is that we could observe the contribution of surface heat flux to shear in the mixed layer, factor often ignored in the current models. In fact, ocean models such as global circulation models (GCMs) are unable to resolve convection and turbulence and, instead, rely on simple convective parameterizations that result in a poor representation of convective processes and their impact on ocean circulation, air–sea exchange, and ocean biology (Vreugdenhil & Gayen, 2021). NIWs have a characteristically high aspect ratio, which ranged from a 0.0019 seasonal mean in the summer to 0.01 in winter in our data. This means small vertical propagation angles of about 1.5° when the column is stably stratified. Thus, a possible explanation for the broad near-inertial energy peak found during winter is the propagation of NIWs generated southward of the mooring position, with a lower inertial period.

Of paramount importance, we have also verified that the energy generated by the shear in the upper layer is well-structured into near-inertial and 6–8-hour period internal waves capable of propagating both horizontally and into deeper layers, where the energy they transport might enhance turbulent mixing. This finding is meaningful in light of the works by Lumpkin and Speer (2007), Zika et al. (2009), and Waterman et al. (2013), among others, which theorize that turbulent mixing is of fundamental importance to the circulation on the Southern Ocean, as it provides the dominant contribution to the downward buoyancy flux required to balance the upward diapycnal transport of deep waters implicated in the overturning circulation across the region.

The shear winter spectrum had a strong but intermittent diurnal component but also had a significative signal in the semi-diurnal band. Energy in both the diurnal and semi-diurnal (inertial) bands were enhanced by this process, which points to a non-linear energy transfer from the diurnal cycle of heating to the semi-diurnal spectrum of inertial motion. Near-inertial internal wave generation was then observed at layers deeper than 100m during these events. Weakly nonlinear theory predicts the transfer of energy between a diurnal and a semi-diurnal mode to a wave pair containing a semidiurnal mode and a diurnal mode of inverse wavenumber as the resonant triad $\omega_1 = \omega_2 \pm \omega_3$. Therefore, it is possible to have either the 8 h, near-inertial and diurnal bands interacting as the triads $\frac{1}{12} = \frac{1}{24} + \frac{1}{24}$; $\frac{1}{12} = \frac{1}{8} - \frac{1}{24}$; $\frac{1}{12} = \frac{1}{6} - \frac{1}{12}$; or $\frac{1}{12} = \frac{1}{4} - \frac{1}{6}$, if the same relation also holds for the wavenumber vectors of these waves, so $\overrightarrow{k_1} = \overrightarrow{k_2} \pm \overrightarrow{k_3}$.

Finally, we have also observed both from utilizing a cross-correlation between our wind, Q_{net}, and shear, and from comparing our data to a slab model that, although

wind forcing is a major forcing of shear and current velocity in the Southern Ocean's upper layer, it is not enough to explain the observed variability. Therefore, it is necessary to include the convective dynamics in the oceanic circulation models in order to properly represent the turbulent mixing and energy transport in the upper layer.

Chapter 5: Near-inertial waves generated by diurnal convection in the Southern Ocean as seen through a numerical experiment

5.1 Introduction

In the previous chapters we have seen how near-inertial internal wave generation in the Southern Ocean cannot be explained in terms of the established theory. During winter, the vertical distribution of energy indicated an unexplained seasonal pattern where energy in the inertial band was concentrated in the maximum shear layer, at around 85 m, without any appreciable representation in the layers above. We have also seen how at these layers, a shift during winter towards both the diurnal and high-frequency energy bands was found.

We have complemented our observations with a slab model which indicated wind is not enough to reproduce the near-inertial signal present in the mooring data. Furthermore, the three most energetic spectral bands, inertial, diurnal and 8 h period, were observed to occur synchronically, and many times respond to the same excitation events but with different relaxation times. These analyses point toward a non-linear interaction among these 3 bands.

Although some insights can be gained from weakly nonlinear theory, the dynamics of fully nonlinear finite-amplitude internal waves, with very few and trivial exceptions, can be examined only through analysis of numerical simulations in which the Navier-Stokes equations are iteratively solved in time (Sutherland, 2005).

Open-ocean convection is a strongly nonlinear dynamic phenomenon observed in a few regions of the World Ocean. Being a localized or even mesoscale phenomenon (Moore et al., 2015, Nagurnyi et al., 1985, Johannessen et al., 1991,

Johannessen et al., 2013), it is an inherent part of the Global Ocean Conveyor, affecting the global climate state over a wide range of temporal scales (Marshall and Schott, 1999, Alekseev et al., 2001a, Visbeck, 2007, Lumpkin and Speer, 2007, Buckley and Marshall, 2016, Chafik and Rossby, 2019).

A broad spectrum of approaches to the convection problem have been tried, with varying degrees of complexity: From simple conceptual models to the state-of-the-art nonhydrostatic simulations (Killworth, 1979, Androsov et al., 2005, Mikolajewicz et al., 2005, Kovalevsky et al., 2020). In a conceptually simple side of the modelling spectrum, such approaches as box models (Stommel, 1961, Stommel and Young, 1993, Cessi, 1994, Scott et al., 1999, Zickfeld et al., 2004) and one-dimensional (1D) mixed layer models (Garwood, 1991) provide interesting insights in the link between the processes of water mixing during deep convective events and upper ocean inflow in the convective regions and the deep water outflow from the regions. In particular, box models are able to provide multiple steady states, that are hypothesized to correspond to plausible states of ocean circulation under past or projected future climates (opposed to spurious multiple steady states caused by flux corrections in certain coupled primitive equation ocean–atmosphere models, see Neelin and Dijkstra (1995) for more discussions).

However, as the oscillatory behavior of the convective cell and the shear it generates cannot be described by a hydrostatic approximation, the current literature misses a nonhydrostatic experiment where the forcing conditions are simple enough to isolate the effect of each parameter. Another missing aspect of current experiments is a focus not on the convection itself but what oscillatory behavior does it cause and if/how this oscillation is able to propagate. Therefore, it is

necessary to engage in substantially more complex numerical experiments to explore this enigma and reproduce the phenomena we are concerned with.

5.2 Methods

5.2.1 Model setup

To reproduce the surface cooling-induced convection and the consequent near-inertial wave generation, we formulated a 2-D model incorporating non-hydrostatic dynamics. Usually, the most computationally intensive term to calculate in such models is the pressure, but we can exclude pressure from terms from our calculation by employing the Navier-Stokes equation with a rigid-lid, incompressible, and Boussinesq approximation, which can then be written as

$$\begin{cases} \dfrac{\partial \mathrm{u}}{\partial \mathrm{t}} + \mathrm{u}\dfrac{\partial \mathrm{u}}{\partial \mathrm{x}} + \mathrm{w}\dfrac{\partial \mathrm{u}}{\partial \mathrm{z}} = -\dfrac{1}{\rho_0}\dfrac{\partial \mathrm{p}'}{\partial \mathrm{x}} + \mathrm{A_z}\dfrac{\partial^2 \mathrm{u}}{\partial \mathrm{z}^2} + \mathrm{A_H}\boldsymbol{\nabla}_{\mathrm{H}}^2\mathrm{u} + \mathrm{fv} & (5.1a) \\ \dfrac{\partial \mathrm{w}}{\partial \mathrm{t}} + \mathrm{u}\dfrac{\partial \mathrm{w}}{\partial \mathrm{x}} + \mathrm{w}\dfrac{\partial \mathrm{w}}{\partial \mathrm{z}} = -\dfrac{1}{\rho_0}\dfrac{\partial \mathrm{p}'}{\partial \mathrm{z}} - \mathrm{g}\dfrac{\rho'}{\rho_0} + \mathrm{A_z}\dfrac{\partial^2 \mathrm{w}}{\partial \mathrm{z}^2} + \mathrm{A_H}\boldsymbol{\nabla}_{\mathrm{H}}^2\mathrm{w} & (5.1b) \\ \dfrac{\partial \mathrm{u}}{\partial \mathrm{x}} + \dfrac{\partial \mathrm{w}}{\partial \mathrm{z}} = 0, & (5.1c) \end{cases}$$

where $\boldsymbol{\nabla}^2{}_H \equiv \frac{\partial^2}{\partial x^2} + \frac{\partial^2}{\partial y^2}$ and A is the eddy viscosity coefficient.

Solving for the primary variables u, w, and p' and cross differentiating them we get

$$\frac{\partial}{\partial \mathrm{z}}\left[\frac{\partial \mathrm{u}}{\partial \mathrm{t}}\right] + \frac{\partial}{\partial \mathrm{z}}\left[\mathrm{u}\frac{\partial \mathrm{u}}{\partial \mathrm{x}}\right] + \frac{\partial}{\partial \mathrm{z}}\left[\mathrm{w}\frac{\partial \mathrm{u}}{\partial \mathrm{z}}\right] = \frac{\partial}{\partial \mathrm{z}}\left[-\frac{1}{\rho_0}\frac{\partial \mathrm{p}'}{\partial \mathrm{x}} + fv\right] + \mathrm{A_z}\frac{\partial^3 \mathrm{u}}{\partial \mathrm{z}^3} + \mathrm{A_H}\frac{\partial \boldsymbol{\nabla}_{\mathrm{H}}^2\mathrm{u}}{\partial \mathrm{z}}, \quad (5.2)$$

from differentiating Equation 5.1a with respect to z, and

$$\frac{\partial}{\partial \mathrm{x}}\left[\frac{\partial \mathrm{w}}{\partial \mathrm{t}}\right]+\frac{\partial}{\partial \mathrm{x}}\left[\mathrm{u}\frac{\partial \mathrm{w}}{\partial \mathrm{z}}\right]+\frac{\partial}{\partial \mathrm{x}}\left[\mathrm{w}\frac{\partial \mathrm{w}}{\partial \mathrm{z}}\right]$$
$$=\frac{\partial}{\partial \mathrm{x}}\left[-\frac{1}{\rho_0}\frac{\partial \mathrm{p}'}{\partial \mathrm{z}}\right]-\mathrm{g}\frac{\partial}{\partial \mathrm{x}}\left[\frac{\rho'}{\rho_0}\right]+\mathrm{A_z}\frac{\partial^3 \mathrm{w}}{\partial \mathrm{z}^2\,\partial \mathrm{x}}+\mathrm{A_H}\frac{\partial \boldsymbol{\nabla}_\mathrm{H}^2 \mathrm{w}}{\partial \mathrm{x}}, \tag{5.3}$$

from differentiating Equation 5.1b with respect to x.

Subtracting Equation 5.2 from Equation 5.3 we arrive at

$$\frac{\partial}{\partial \mathrm{t}}\left[\frac{\partial \mathrm{u}}{\partial \mathrm{z}}-\frac{\partial \mathrm{w}}{\partial \mathrm{x}}\right]+\frac{\partial}{\partial \mathrm{x}}\left[\mathrm{u}\left(\frac{\partial \mathrm{u}}{\partial \mathrm{z}}-\frac{\partial \mathrm{w}}{\partial \mathrm{x}}\right)\right]+\frac{\partial}{\partial \mathrm{z}}\left[\mathrm{w}\left(\frac{\partial \mathrm{u}}{\partial \mathrm{z}}-\frac{\partial \mathrm{w}}{\partial \mathrm{x}}\right)+fv\right]$$
$$=\frac{\mathrm{g}}{\rho_0}\frac{\partial \rho'}{\partial \mathrm{x}}+\mathrm{A_z}\frac{\partial^2}{\partial \mathrm{z}^2}\left[\frac{\partial \mathrm{u}}{\partial \mathrm{z}}-\frac{\partial \mathrm{w}}{\partial \mathrm{x}}\right]+\mathrm{A_H}\left[\frac{\partial^2}{\partial \mathrm{x}^2}\left(\frac{\partial \mathrm{u}}{\partial \mathrm{z}}-\frac{\partial \mathrm{w}}{\partial \mathrm{x}}\right)\right] \tag{5.4}$$

Substituting the 2-D definition of vorticity $\zeta=\frac{\partial w}{\partial x}-\frac{\partial u}{\partial z}$:

$$\frac{\partial \zeta}{\partial \mathrm{t}}+\frac{\partial(\mathrm{u}\zeta)}{\partial \mathrm{x}}+\frac{\partial(\mathrm{w}\zeta+f\mathrm{v})}{\partial \mathrm{z}}=-\frac{\mathrm{g}}{\rho_0}\frac{\partial \rho'}{\partial \mathrm{x}}+\mathrm{A_z}\frac{\partial^2 \zeta}{\partial \mathrm{z}^2}+\mathrm{A_H}\frac{\partial^2 \zeta}{\partial \mathrm{x}^2} \tag{5.5}$$

Even though the model is given in the meridional-vertical domain, a zonal velocity component arises from the inertial term and can be derived from the continuity requirement given by Equation 5.1c. This single equation model can then be very efficiently derived, while the current velocity can be recovered from the stream function relation

$$\frac{\partial^2 \Psi}{\partial x^2} + \frac{\partial^2 \Psi}{\partial z^2} = \zeta, \tag{5.6}$$

where the stream function is implicitly defined as $\mathrm{u} = -\frac{\partial \Psi}{\partial \mathrm{z}}$ and $\mathrm{w} = \frac{\partial \Psi}{\partial \mathrm{x}}$.

Based on these equations, we drove a model with a 1-hour time step, implemented using a leap-frog scheme, constant steps for x and z, $\Delta \mathrm{x} = 200\,\mathrm{m}$; $\Delta \mathrm{z} = 5\,\mathrm{m}$, respectively, over a 40000 x 2000 m domain, larger on the horizontal axis. The model spatial structure was discretized following the Arakawa-C grid scheme. The top boundary was an open boundary, while the bottom was a reflective non-slip boundary. Lateral boundaries were set as cyclic.

The model was initialized using a 0 field for ζ and three vertical stratification schemes: First, linearly variating profiles for temperature T and salinity S were used where $T_0 = 0.04\,°\mathrm{C}$, $S_0 = 34$ and

$$\begin{aligned} T_z &= \mathrm{T}_0 - 0.005\mathrm{z} \\ S_z &= S_0 + 0.002z, \end{aligned} \tag{5.7}$$

with the subscript indicating depth in meters. A second scheme representing a weaker and more realistic stratification was tested where $T_0 = 0.04$, $S_0 = 34$ and

$$\begin{aligned} T_z &= \mathrm{T}_0 - 0.0027\mathrm{z} \\ S_z &= S_0 + 7.87 * 10^{-4} z \end{aligned} \tag{5.8}$$

A third stratification scheme was done, introducing a homogeneous ML and a stronger discontinuity at the base . In this scheme $T_z = 0.0$; $S_z = 34$ for $0 \leq z \leq MLD$ and

$$T_z = -0.2 - 0.005z \qquad (5.9)$$
$$S_z = 34.08 + 0.002z$$

Forcing was applied at the surface by a sinusoidal wind velocity term with a period equal to the inertial period IP and amplitude W_{amp}, as described by Equation 5.10. Wind velocity is then translated into stress by the Equation 5.11, where ρ_{air} and C_d are the air density and the dimensionless drag coefficient, taken as 1 kg m^{-3} and 0.0026, respectively. A temperature response variable is introduced at the surface where $\Delta T(t,x) = -dTH * ammp(t) * axx(x)$, where dTH indicates the amplitude of the heat function in °C, the ammp term introduces a diurnal modulation through a cosine function, and axx modulates the heat variable in space through a sine function, so the transfer becomes maximum at the center of the domain. These functions are described by Equations 5.12a,b, and c, where C_w is the specific heat capacity of sea water (J Kg^{-1} C^{-1}), Δt is the model time step (s) and i is the horizontal space coordinate within the discretized model grid.

$$V_w = \frac{W_{amp} * \sin(2\pi * t)}{IP} \qquad (5.10)$$

$$\tau = \frac{0.001 * 0.0026 * V_w * |V_w|}{10} \qquad (5.11)$$

$$ammp = \begin{cases} (0.7 - \cos\left(\frac{2\pi t}{24.0 * 3600}\right) * 0.5; \text{ for } \cos\left(\frac{2\pi t}{24.0 * 3600}\right) > 0.7 \\ 0; \text{ for } \cos\left(\frac{2\pi t}{24.0 * 3600}\right) \leq 0 \end{cases} \qquad (5.12a)$$

$$\mathrm{dTH} = \mathrm{W\,m^{-2}} * \frac{\Delta \mathrm{t}}{(\rho * \mathrm{C_w} * \mathrm{dz})} = 200 * \frac{\Delta \mathrm{t}}{(1.03 * 3930 * \mathrm{dz})} \quad (5.12b)$$

$$\mathrm{axx} = \sin\left((i - 50) * \frac{\pi}{100}\right)\Big|_{50<i<150} \quad (5.12c)$$

From the equations above, the surface cools on a 24 h cycle, where the first and last 3 hours of the daily cycle are not subjected to heat forcing. Note that there is no temperature forcing component associated with the inertial period. Nevertheless, we drove the model with internal parameters of $2\pi/f = 13.81\ \mathrm{h}$, which is the inertial period at the mooring site described in Chapter 3, and $2\pi/f = 19\ h$. The two inertial parameters were used to observe if a value close to 12 h, a natural harmonic of the diurnal period present in surface heat oscillations, would lead to amplification of internal wave energy due to resonance.

5.2.3 Model Nomenclature

Many model runs were carried out testing different stratification conditions, wind and heat forcing. To reduce the space necessary to describe every setup made, the three main settings for initial vertical stratification, heat flux amplitude, and wind amplitude were incorporated into a naming convention as follows:

- The initial vertical stratification scheme is indicated as L or D for Linearly Stratified and Discontinuity at the Base schemes, respectively.
- The driving mechanism applied is indicated as WIND and/or HEAT.
- The inertial period, in hours, is mentioned in integer form as either 14 or 19

Many configurations were tested but the runs where initial MLD was 100 m, heat forcing had 200 J s^{-1} cm^{-2} and wind had 3 m s^{-1} amplitude were selected to be shown as representative of the system. So, for example, the run LHEAT13 indicates a start from a linearly stratified initial condition, a 200 J s^{-1} cm^{-2} heat flux amplitude, with $2\pi/f = 13.81$ h and no wind forcing.

5.3 Results

5.3.1 Dependance on initial stratification conditions

Model runs incorporating the effect of the stratification schemes described in Equations 5.7 and 5.9 in the model's temperature distribution are shown in Figure 5.1a and b, which depict runs LHEAT14 and DHEAT14, respectively. The initial depth of the pycnocline was set at 100m in both cases. We find that, under equal forcing, the initial stratification constrains convection depth even after 4000 hours have passed. Under an initial linear stratification scheme, the MLD was observed to reach about 400m deep, while a homogeneous mixed layer with a strong discontinuity at the base, such as described by the third scheme, constrains MLD to about 200m.

The expression of the stratification pattern on the salinity field, given by the contours in Figure 5.1, accompanies the temperature vertical reach. The general consequence of the convective motion is that cold water is pumped downwards but this water is also relatively fresher, so the density remains relatively the same. No significant differences were found in the distribution of the seawater physical properties between the cases with different inertial periods.

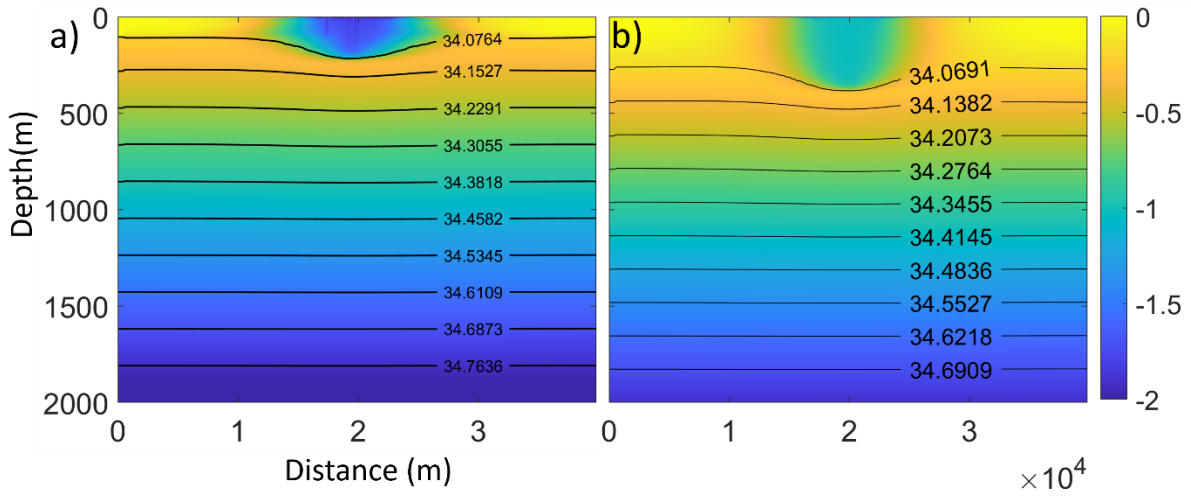

Figure 5.1. Temperature profiles after 4000 h of simulation from the stronger (a) and weaker (b) stratification patterns of runs DHEAT14 and LHEAT14, respectively, temperature is given by color-coding, while the black contours indicate salinity isolines.

The near-inertial energy increases at the maximum shear depth, previously discussed in chapter 4.4 was found both in model runs solely incorporating wind forcing and those incorporating both wind and surface cooling. However, the near-inertial energy increase was absent from setups where no initial stratification discontinuity or homogeneous ML was used. Likewise, setups using Equation 5.9 all exhibited an energy “bump” at the maximum shear layer. This result points to the hypothesis of the seasonal variability of vertical energy distribution to be a consequence of the vertical stratification. Although surface cooling during winter can cause a large discontinuity in stratification, it does not seem to be a necessary condition, and wind forcing can excite this increase if a previously established stratification profile persists. In short, the evolution of vertical stratification in time presents significant difference between a heat flux or wind surface forcing.

5.3.2 Energy spectra under wind and heat forcing

Comparing experiments where the same stratification, inertial period and boundary conditions were used but with changes in forcing revealed important aspects of the Southern Ocean upper layer. Juxtaposition of spectral analysis of the runs DHEAT14 and DWINDHEAT14, shown in Figure 5.2, indicate that the introduction of surface diurnal heat cooling in addition to wind forcing generates significant sub-harmonics of 8, 6, 4 and 3.5 hours, which are expressive down to 2000 m (distribution up to 450 m shown in Figure 5.2a). Meanwhile, under the same circumstances, wind forcing alone could not reproduce these high-frequency harmonics. These results were consistent between different inertial periods, and values for heat and wind forcing.

Another result, evident in Figure 5.2c and d, is the entrapment of near-inertial energy at the lower boundary of the ML, generating higher near-inertial energy at this layer when compared to wind forcing alone. The highest near-inertial energy peak was of 113500 and 168400 J s^{-1} cm^{-2} when considering DWIND14 and DWINDHEAT14, respectively. Therefore, heat forcing was constrained to provide 54900 J s^{-1} cm^{-2} to the near-inertial band at the base of the ML.

In terms of wavenumber spectra, described in Figures 5.3 and 5.4 for the DWINDHEAT14 and DHEAT14 setups, respectively, a common pattern was found: Outside of the convective zone, most of the energy is concentrated in the smaller horizontal wavenumbers, with a peak at the limit of 6.283×10^{-4} radians per meter, which we believe is a constraint due to the model dimensions. However, a shift towards higher wavenumbers was found inside the convective zone for both experiments. Furthermore, resonant triads were common and energy peaks shifted

in wavenumber space with depth, which suggests non-linear processes as a major contributor to the high-frequency energy inside the convective zone. The process could be verified by comparing current velocity in frequency-space (Figure 5.2), horizontal wavenumber (Figure 5.3 and 5.4) and vertical wavenumber (Figure 5.5).

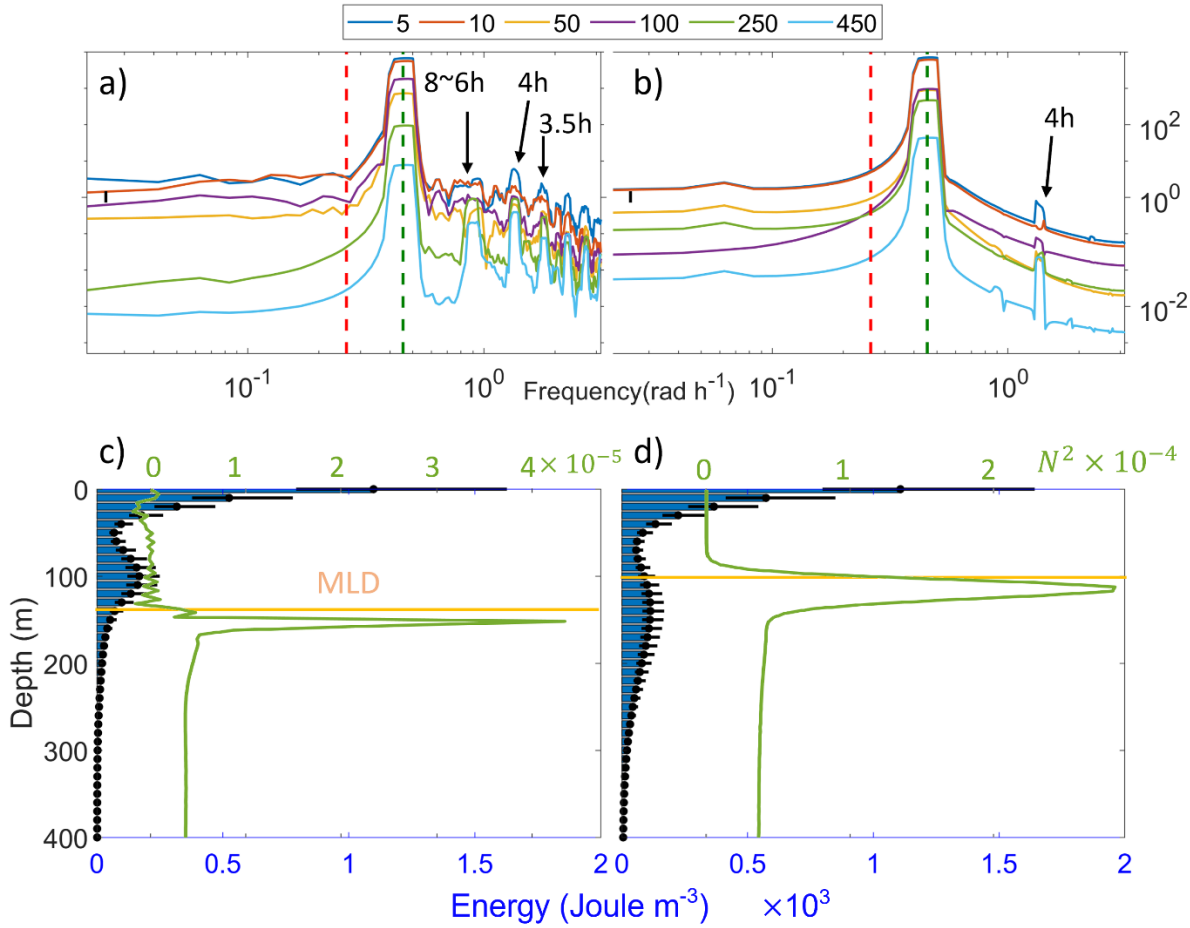

Figure 5.2. Positive (i.e., counterclockwise) 300 h rotary spectra of current velocity (a) and (b) from runs DWINDHEAT14 and DWIND14, respectively, after 1800 h of simulation time and at the center of the domain. The diurnal and semi-diurnal (inertial) frequency is indicated by red and green dashed lines, respectively. The 95% confidence interval is shown as a black cross, and depth (m) of the readings is color coded according to the values indicated in the upper panels. (c) and (d) are bar graphs of the energy contained in the inertial frequency band for the respective (a) and (b) plots and a vertical profile of N^2, given by the green line.

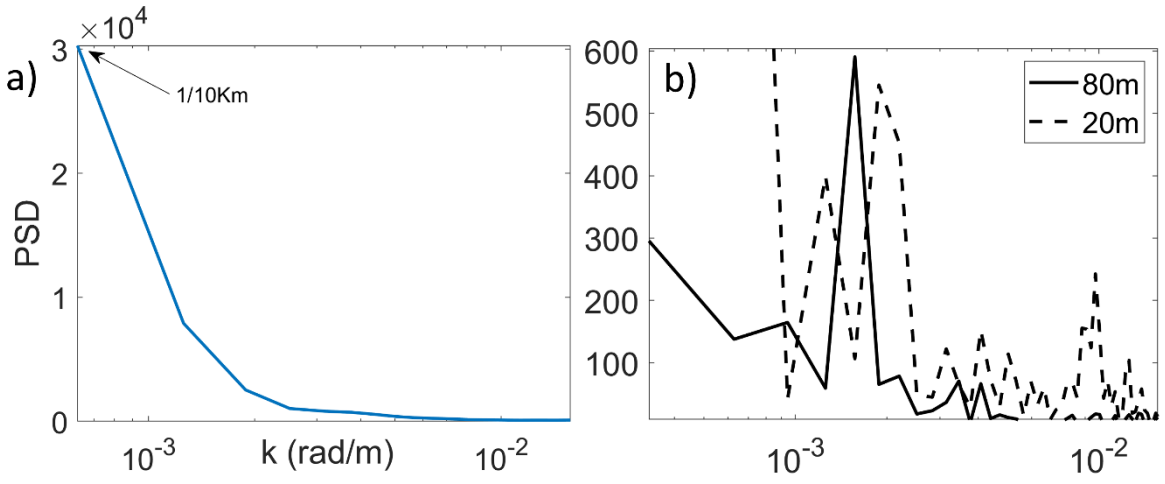

Figure 5.3. Horizontal wavenumber outside (a) and inside (b) the convection zone, for the DWINDHEAT14 experiment.

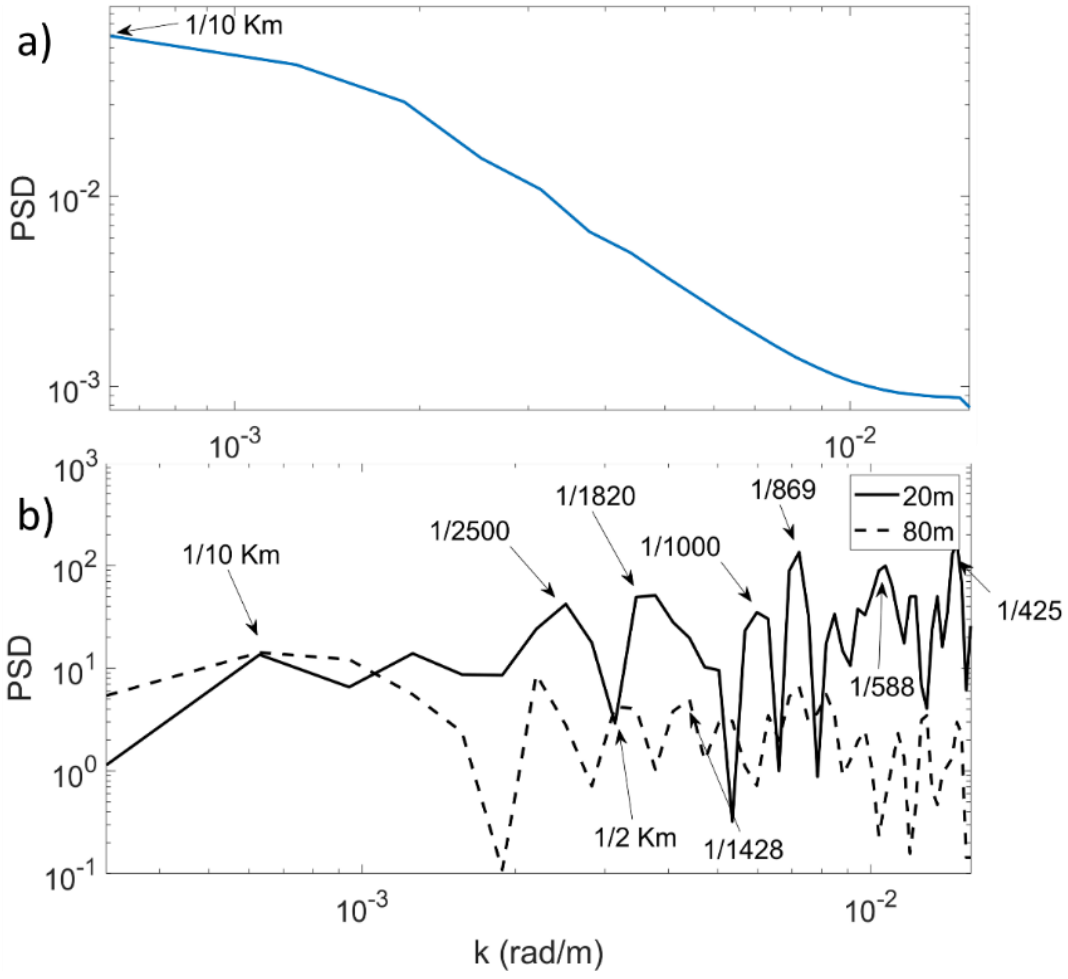

Figure 5.4. Horizontal wavenumber outside (a) and inside (b) the convection zone, for the DHEAT14 experiment.

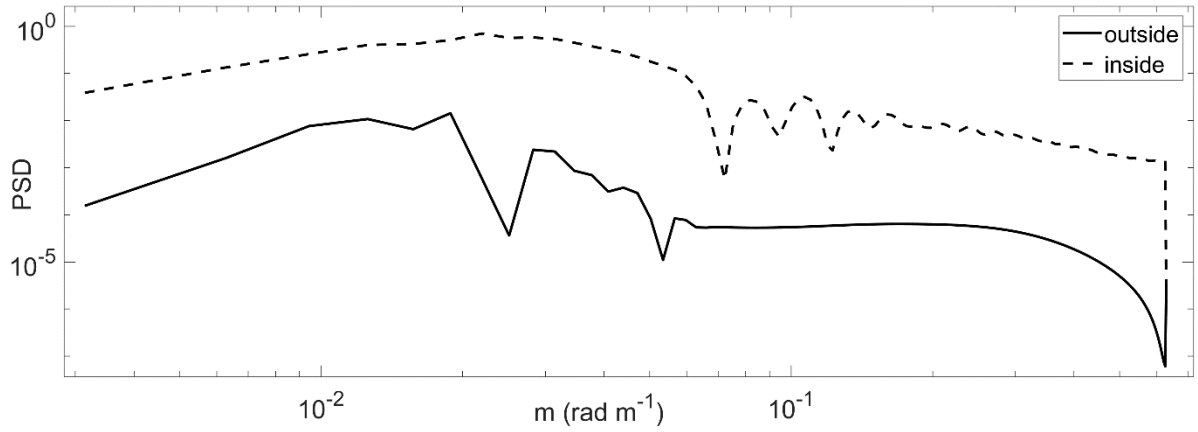

Figure 5.5. Vertical wavenumber outside and inside the convection zone, for the DHEAT14 experiment.

Another observation is that under a purely eolic forcing the MLD did not significantly change if the initial MLD is below the Ekman depth. However, heat forcing is able to quickly increase the MLD as long as the heat flux is enough to increase density at the surface. This difference can be thought to be a consequence of wind forcing having to work the entire ML to homogenize it, while surface cooling is aided by gravity, only working at the surface to cause instability. In this case, the convectional instability is enough to break stratification even if the water parcel is locally stable and the only limitations are the surface flux and the density diffusivity.

A consequence of the high-frequency harmonics generated by surface heat forcing is the smaller aspect ratio, resulting in stronger vertical propagation, as can be observed through the stream function in Figure 5.6a. In contrast, a wind-forced propagation generated mostly near-inertial waves which, due to the internal wave dispersion relation, propagate at very high aspect ratios, close to the horizontal, as can be seen in Figure 5.6b. This pattern has significant consequences for the communication between surface and deep ocean:

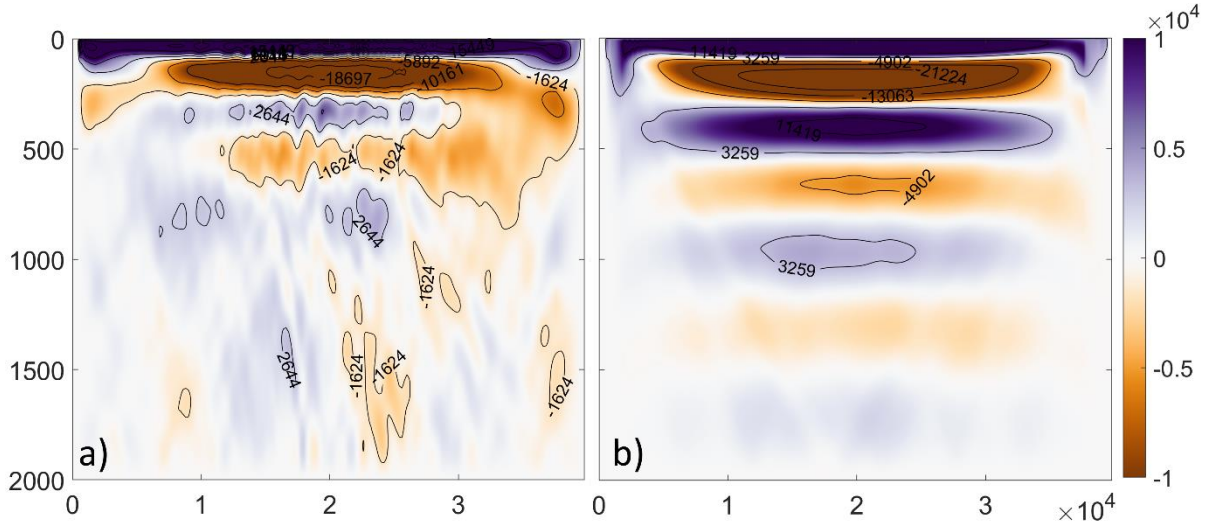

Figure 5.6. Vertical profile of the stream function ($cm^2\ s^{-1}$) of model runs DWINDHEAT14 and DWIND14, respectively, after 1800 h of simulation time.

The horizontal propagation on NIWs generates isolated circulation cells without significant connection between them. However, when a diurnal heat forcing is present, as is the case on high latitudes, higher frequency internal waves are non-linearly generated, and these waves can easily reach the deep ocean without suffering significant attenuation. As such, we predict a enhanced vertical flux at high latitudes.

5.3.3 Zonal velocity

The zonal velocity and stream functions for DWINDHEAT14 (Figure 5.7a and c) and DWINDHEAT19 (5.7b and d) illustrate how under geostrophic balance, a deep-reaching zonal circulation system is generated from the convective circulation, moving clockwise at the surface and anti-clockwise below the mixed layer. It should be noted that the smaller inertial period of 13.81 h induced a deeper circulation, and the vertical difference between contours of zonal velocity ranged from as little as 5m

at the 3.81 cm s^{-1} contour around the 300 m depth to as much as 150m at the 0.55 cm s^{-1} contour around the 1200m depth.

In terms of the meridional and vertical velocity components, implicitly given by the stream function, it was generally observed that velocity was stronger at the convection region, but significant downward propagation was observed below the convective zone. Velocity was stronger at the mixed layer when inertial period was higher, but a smaller inertial period produced deeper significant propagation.

The spectral analysis of the horizontal velocity u, found by deriving the stream function with respect to the vertical, is given in Figure 5.8. Higher inertial period (Figure 5.8b and 5.8d) was seen to reproduce higher velocity values near the surface while having comparable magnitude between 100 and 200 m. A similar vertical distribution was observed in both cases, but the lower period simulations (Figure 5.8a and 5.8c) maintained narrower and more significant peaks around the diurnal and inertial bands, while the higher T simulations exhibited a broader spectral signature around the inertial band when away from the convection zone (Figure 5.8b) or a nearly constant power density at the center of the convective zone (Figure 5.8d) until decaying above the inertial frequency.

Curiously, a phenomenon was observed at the center of the domain on the T=19 h simulation, where energy vanishes from the inertial frequency and its harmonics, as can be seen on Figure 5.8d. In all cases spectra becomes more defined below the mixed layer instabilities, at 200 m and below.

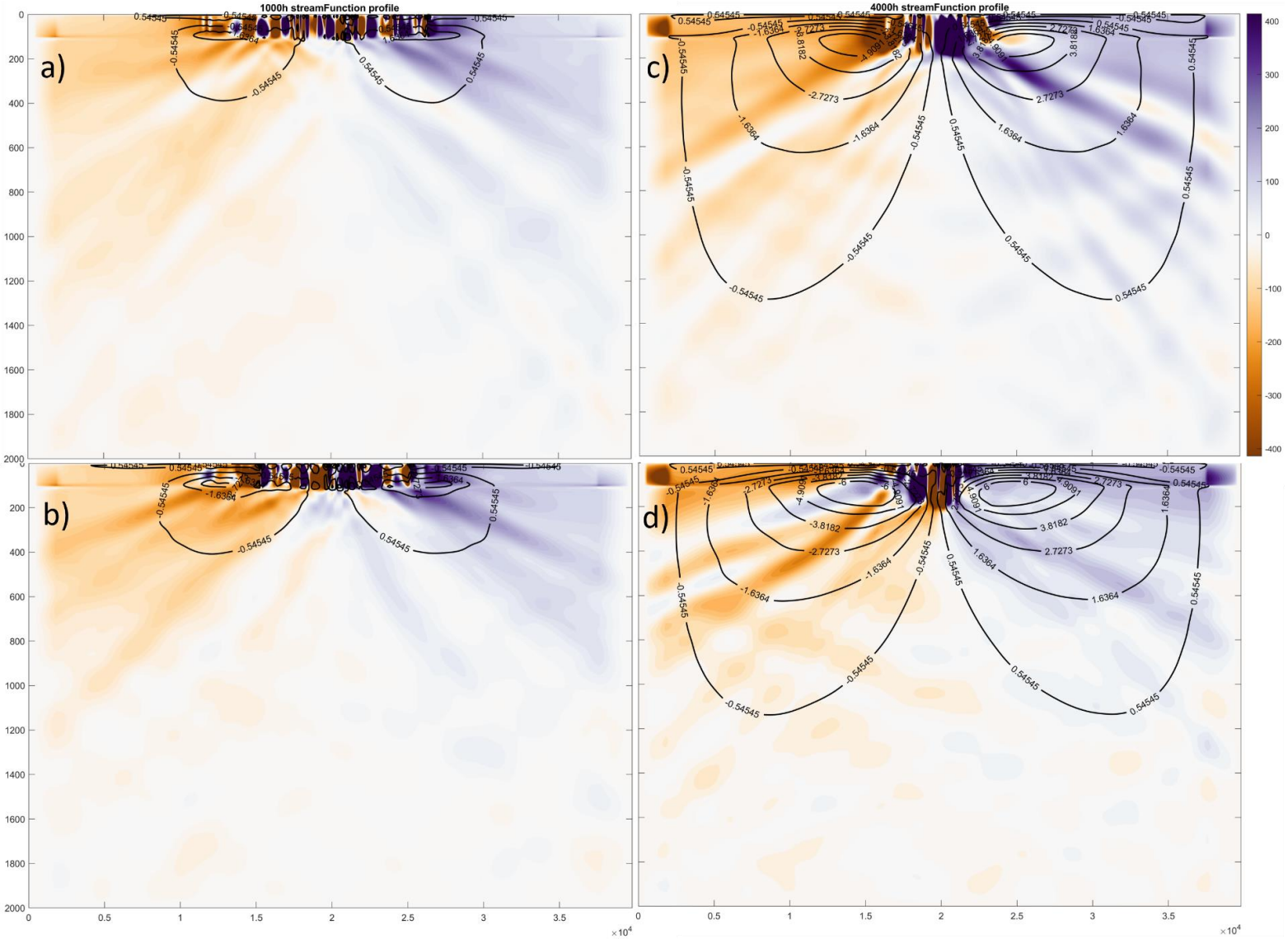

Figure 5.7. Stream function ($cm^2\ s^{-1}$) and zonal velocity ($cm\ s^{-1}$), described by the color-code and the black lines, respectively. Graphs are shown for T=13 h (a and c) and T=19 h (b and d) at 1000 h (a and b) and 4000 h(c and d) of simulation time.

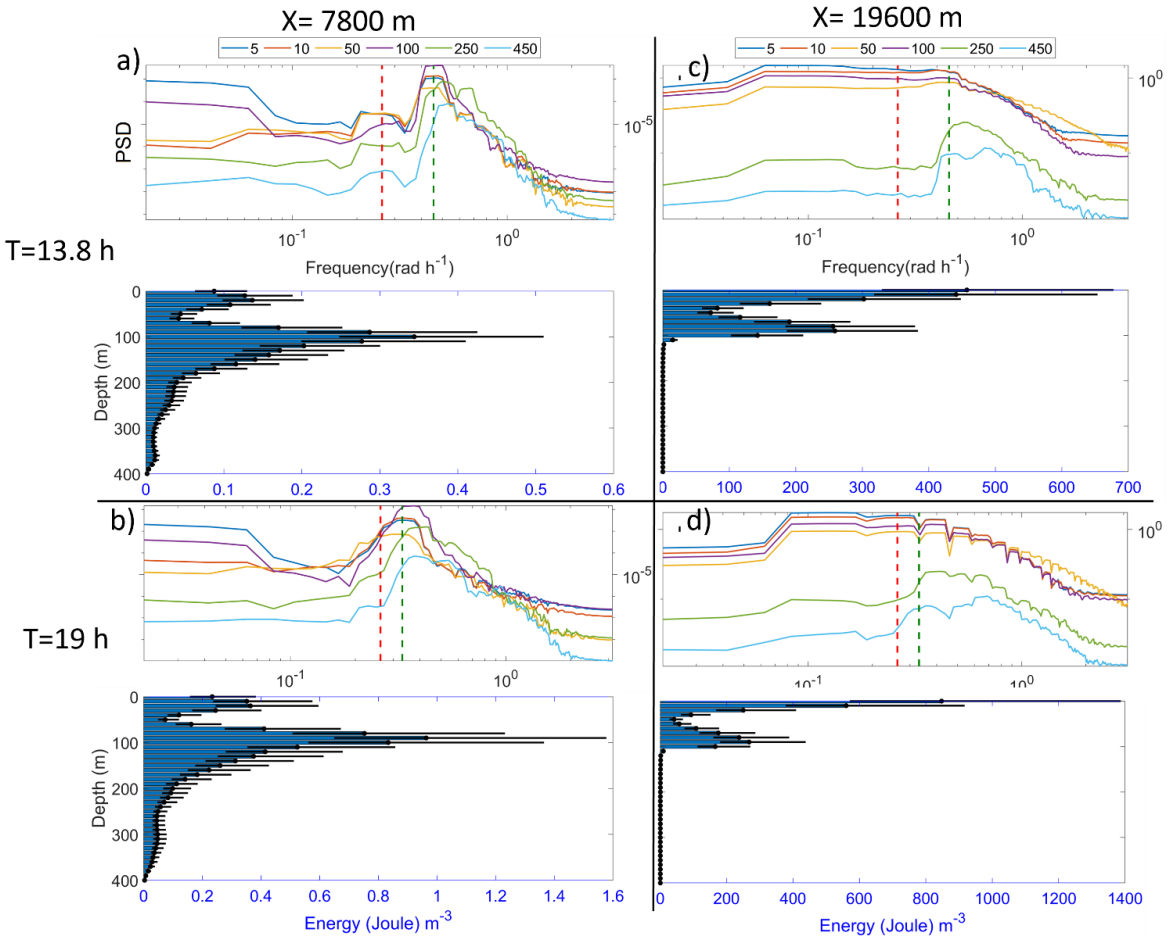

Figure 5.8. Spectral analysis where the Fourier transform is shown in the upper panels and the frequency-integrated energy over the near inertial band is given by the lower panels for T=13.8 h (a and c), and T=19 h(b and d) at the positions marked on the top. The red and green dashed lines indicate the diurnal and near inertial period for each graph.

5.4 Reproduction of mooring results

The vertical profile of the Fourier transformed horizontal velocity in the DHEAT14 numerical experiment (Figure 5.9) consistently produced a strong second-mode vertical structure. Energy in the near-inertial band was enhanced at the lower boundaries of the convective penetration depth and reached magnitudes similar to the near-surface values, as indicated in Figure 5.9b and d. Furthermore, the model reproduced the mooring's winter vertical energy distribution (higher concentration of near-inertial energy at the maximum shear depth) at the borders of the convective zone, as shown in Figure 5.9c and d. The reproduction of mooring data at the edges of the convective zone, instead of the center of the domain suggest that differential heating might be a key factor for explaining the Winter energy pattern discussed in section 4.3.1.

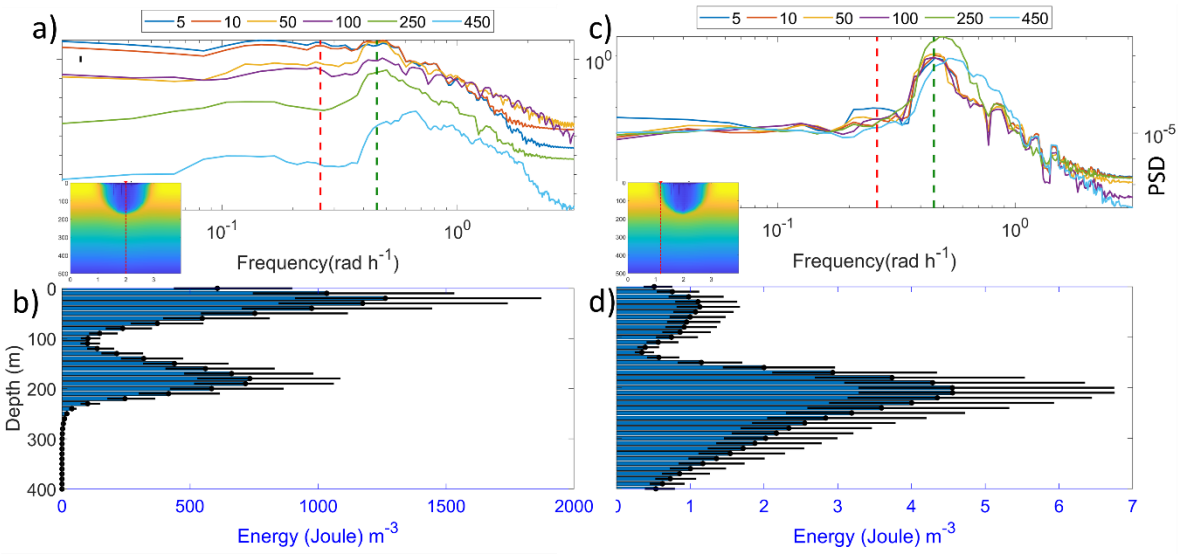

Figure 5.9. Spectral analysis of the horizontal velocity, where the Fourier transform is shown in the upper panels (a) and (c), as well as the frequency-integrated energy over the near-inertial band(b) and (d) are shown for the locations indicated in the down left portion of (a) and (c). The red and green dashed lines indicate the diurnal and near inertial period for each graph.

5.5 Discussion

The results from our modeling experiments evidence the non-linear generation mechanism of near-inertial internal waves from the interaction of the diurnal convective forcing and the semi-diurnal (at high latitudes) wind forcing. This highlights the existence of a previously unknown mode of energy transport from the subsurface to deeper layers, where this energy might enhance mixing by inducing turbulence.

The diverse stratification profiles used in the experiment indicate the dynamics of the Southern Ocean's upper layer to be highly sensitive to the initial stratification of the water column. The depth of the mixed layer between the runs using the stratification schemes described by Equations 5.7 and 5.8 differed by about 200 m, with the discontinuity in the profile 5.8 inhibiting depth increase. The reason for this phenomenon is likely the density balance caused by the pumping of cold water being balanced by being fresher than surrounding waters, increasing the energy necessary to effectively break stratification. An interesting consequence of this is that a heat dominated system takes a long time to fully develop its mixed layer, as opposed to wind systems, where only a few inertial cycles are necessary to develop their mixed layer.

These results bear directly on the proposed sensitivity of modern global energy balance and carbon cycling to changes in Southern Ocean convection (de Lavergne et al., 2014, Skinner et al., 2020) which suggest open ocean convection in the Southern Ocean to be weakening under anthropogenic forcing. De Lavergne et al. (2014) also suggests a decline of open-ocean convection would reduce the production of AABW, with important implications for ocean heat and carbon storage.

Meanwhile, our results indicate that a reduction in convective activity by salinity stratification would also disrupt the propagation of internal waves generated at the upper layer.

Furthermore, Skinner et al. (2020) argues the inability of many numerical ‘hosing’ experiments to reproduce the observed amplitude of Antarctic temperature and CO_2 change across Heinrich stadials could be due to a lack of deep convection in the Southern Ocean in these models, perhaps due to missing sub-grid scale processes, misrepresented atmospheric teleconnections, or possibly due to excess buoyancy being supplied. The author would suggest that accurate projections of future climate-carbon cycle feedbacks are likely to rely on an improved representation of the complex interplay between evolving winds, buoyancy, and mass transport, in the Southern Ocean. As such, we provide a new mechanism which might help generate better fore and hindcasts through the interaction of the diurnal buoyancy forcing and near-inertial shear and waves.

A point that should be addressed in the future is that our model produced unrealistic horizontal speeds at the surface of the convective zone. This might be a consequence of the Arakawa-C gridding over a large horizontal step, since it generates convective cells of horizontal length equal to the grid size. On a higher resolution grid, we expect vertical motion to play a larger hole in the convective cycle of the surface particles.

In conclusion, although simple, the numerical experiments conducted in this chapter successfully produce near-inertial internal waves without any inertial forcing, therefore providing robust evidence of a new mechanism of energy propagation. Although diurnal oscillations cannot propagate at higher latitudes, they were seen to

generate internal waves which can propagate both vertically and horizontally over long distances. Therefore, a method of communication between the Antarctic Surface Water and other masses such as the upper Circumpolar Deep Water (uCDW) is revealed, and it might become a key finding to elucidate the coupling between upper and deeper layers not only in the Southern Ocean but also in high latitude oceans in general.

Chapter 6: Main findings, conclusion, and final remarks

The dynamics involved in the variability of temperature, salinity, and density distributions in the upper layer of the Indo-Pacific sector of the Southern Ocean were studied using Acoustic Doppler Current Profiler and Conductivity Temperature Depth data from an m-TRITON mooring deployed at 60 °S and 140 °E between January 15th and December 19th, 2012, together with hydrographic casts, reanalysis outputs, and satellite imagery. Spectral analysis confirmed that near-inertial internal waves are a major factor transporting energy downwards to the lower boundary of the mixed layer, with 12.5 J m^{-3} or 45% of the mean surface energy being able to reach deeper than the mixed layer depth during one of the analyzed events. During a period of net heat loss from the ocean surface to the atmosphere, most of the energy was concentrated below the maximum shear layer, at around 80 m deep. Internal wave events were found to be linked to scalar diffusivity increases of up to two orders of magnitude. A box model clarified that surface cooling plays the most significant role in mixing surface waters during winter, but it is not enough to explain variability below 100 m depth, where horizontal advection and eddy enhancement are also important in modulating warm water flux. Our results elucidate how wind energy might enhance mixing, even in ice-covered regions, while influencing depths greater than previously thought.

We also find significant correlation (> 0.6) between heat flux and shear when the net heat flux points towards the atmosphere. The spectral signature of shear and velocity were seen to have significant near inertial components, despite its diurnal forcing. We explored the non-linear internal wave generation by building a 2D nonhydrostatic numerical model to simulate the effect of diurnal surface cooling as a

forcing agent for mixed layer convective instability and internal wave generation. Two stratification initialization settings were devised, a top-to-bottom linearly stratified condition and another setting where the linearized stratification is interrupted by a homogeneous 100m deep mixed layer followed by a discontinuity at the base. The model included the Coriolis effect and runs with inertial period T=13.8 h and T=19 h were done to test for resonance. In all scenarios the result was clear: From a starting stratified ocean near-inertial internal waves were generated even though there is not any inertial forcing employed in the model. The propagating internal waves could be seen to have significant energy up to 400 m, and as such, can potentially serve as a connection between the Southern Ocean upper layer variability and the deeper ocean. Additionally, we observed a stronger initial stratification at the base of the mixed layer reduces the convection depth even after 4000 hours of model time.

The significance of these results is that we could observe the contribution of surface heat flux to shear in the mixed layer, a factor often ignored in the current models. Of paramount importance, we have also verified that the energy generated by this shear is well-structured into near-inertial and 6–8-hour period internal waves capable of propagating both horizontally and into deeper layers, where the energy they transport might enhance turbulent mixing.

These results both agree and complement Waterman et al. (2012) findings, which suggest turbulent dissipation in the ocean interior is underpinned by breaking internal waves; either downward-propagating near-inertial waves or upward-propagating high-frequency waves, in the deepest 1-2 km of the water column. We provide evidence of another source of both inertial and high-frequency internal waves: The convective adjustment of the Southern Ocean's upper layer during

winter. In our experiments, high-frequency waves are also seen to be generated at the mixed layer boundary and transport energy downward, contributing to the energy field in the top 2 km of the water column as well.

A point to be addressed in the future is that our model produced unrealistic horizontal speeds at the surface of the convective zone. This might be a consequence of the Arakawa-C gridding over a large horizontal step, as it generates convective cells of horizontal length equal to the grid size. On a higher resolution grid, we expect the surface particles to describe a purely vertical motion inside the convective zone.

The results relating to the numerical experiment described in Chapter 5 represent an interesting addition to the dynamics pertaining to the resonant generation of wind-forced near-inertial motion in a laterally sheared geostrophic flow, as described by Whitt and Thomas (2015). We expand upon their results to also include heat-induced fluxes as a generator of near-inertial energy, and we explore the cases of inertial response when the Rosby radius is not as small as to make the nonlinear advection terms negligible. We verified that in these cases high frequency oscillations are also generated, with significant vertical propagation. Nevertheless, a quantitative estimate for how much of the internal wave field is driven by differential heating remains unexplored. Therefore, as a next step, other heating patterns inside the domain should be tested such as a spatially constant cooling of the entire domain and a heat-flux increasing along the horizontal axis.

7. Acknowledgements

I would like to extend our gratefulness to the Ministry of Education, Culture, Sports, Science and Technology of Japan (MEXT) which provided scholarship to the author so the project could be done and to the scientific cooperation between Japan and Brazil for enabling this exchange to take place.

I am grateful to Dr. Shoichiro Baba, who implemented the m-TRITON mooring system in the Southern Ocean, and the crew of Umitakamaru. The mooring and CTD casts data (Azevedo & Aoki, 2022a, 2022b) are archived and provided by the Arctic Data archive System (ADS), developed by the National Institute of Polar Research (NIPR) at https://ads.nipr.ac.jp/dataset/A20220225-001 and https://ads.nipr.ac.jp/dataset/A20220225-002, respectively. The Ssalto/Duacs altimeter products were produced and distributed by the Copernicus Marine and Environment Monitoring Service (CMEMS) at https://cds.climate.copernicus.eu/cdsapp#!/dataset/satellite-sea-level-global.

Hersbach et al. (2018) ERA5 data was downloaded from the Copernicus Climate Change Service (C3S) Climate Data Store at https://doi.org/10.24381/cds.adbb2d47. The results contain modified Copernicus Climate Change Service information 2020. Neither the European Commission nor ECMWF is responsible for any use that may be made of the Copernicus information or data it contains.

9 References

Abernathey, P. R., Cerovecki, I., Holland, R. P., Newsom E., Mazloff, M., & Talley, D. L. (2016), Water-mass transformation by sea ice in the upper branch of the Southern Ocean overturning. *Nature Geoscience*, *9*, 596–601. doi:10.1038/ngeo2749

Alekseev, G.V., Johannessen, O. M., Korablev, A. A., Ivanov, V. V., Kovalevsky, D. V. (2001), Interannual variability in water masses in the Greenland Sea and adjacent areas Polar Research, 20, 201-208.

Alford, M. H. (2001). Internal Swell Generation: The Spatial Distribution of Energy Flux from the Wind to Mixed Layer Near-Inertial Motions, Journal of Physical Oceanography, 31(8), 2359-2368. Retrieved May 29, 2022, from https://journals.ametsoc.org/view/journals/phoc/31/8/1520-0485_2001_031_2359_isgtsd_2.0.co_2.xml

Alford, M. H. 2003. Redistribution of energy available for ocean mixing by long-range propagation of internal waves. Nature 423:159–163, http://dx.doi.org/10.1038/nature01628.

Alford, M. H., Cronin, M. F., Klymak, J. M. (2012), Annual Cycle and Depth Penetration of Wind-Generated Near-Inertial Internal Waves at Ocean Station Papa in the Northeast Pacific. *Journal of Physical Oceanography*, 42, 889-909. https://doi.org/10.1175/JPO-D-11-092.1

Androsov, A., Rubino, A., Romeiser, R., Sein, D.V. (2005) Open-ocean convection in the Greenland Sea: preconditioning through a mesoscale chimney and detectability in SAR imagery studied with a hierarchy of nested numerical models, *Meteorolische Zeitschrift*, 14, 693-702. doi:10.1127/0941-2948/2005/0078

Bachman, S. D., Taylor, J. R., Adams, K. A., & Hosegood, P. J. (2017), Mesoscale and Submesoscale Effects on Mixed Layer Depth in the Southern Ocean. Journal of *Physical Oceanography, 47*, 2173-2188. doi:10.1175/JPO-D-17-0034.1

Benjamin, T. B. & Feir, J. E. (1967). The Disintegration of wavetrains on deep water. *Journal of Fluid Mechanics*, 27, 417.

Brannigan, L., Lenn, Y.-D., Rippeth, T. P., McDonagh, E., Chereskin, T. K. & Sprintall, J. (2013), Shear at the Base of the Oceanic Mixed Layer Generated by Wind Shear Alignment. *Journal of Physical Oceanography*, 43, 1798-1810. https://doi.org/10.1175/JPO-D-12-0104.1

Buckley, M.W. & Marshall, J. (2016), Observations, inferences, and mechanisms of the Atlantic Meridional Overturning Circulation: a review. Reviews of Geophysics, 54, 5-63, doi:10.1002/2015RG000493

Cessi, P. (1994), A simple box model of stochastically forced thermohaline flow. *Journal of Physical Oceanography*, 24, 1911-1920, doi:10.1175/1520-0485

Chafik, L., & Rossby, T. (2019), Volume,heat, and freshwater divergences in the subpolar North Atlantic suggest the Nordic Seas as key to the state of the meridional overturning circulation. *Geophysical Research Letters*,46,4799–4808. https://doi.org/10.1029/2019GL082110

Cheon, W. G., Park, Y-G., Toggweiler, J. R. & Lee, S-K. (2014), The Relationship of Weddell Polynya and Open-Ocean Deep Convection to the Southern Hemisphere Westerlies. *Journal of Physical Oceanography*, 44, 694-713. https://doi.org/ 10.1175/JPO-D-13-0112.1

Cheon, W. G., Lee, S-K, Gordon, A. L., Liu, Y., Cho, C-B. & Park, J.J. (2015), Replicating the 1970's Weddell Polynya using a coupled ocean-sea ice model with reanalysis surface flux fields. *Journal of Physical Oceanography*, 44, 694-713.

Clarke, R. A. & Gascard, J-C. (1983), The Formation of Labrador Sea Water. Part I: Large-Scale Processes. *Journal of Physical Oceanography*, 13, 1764-1778. https://doi.org/10.1175/1520-0485(1983)013<1764:TFOLSW>2.0.CO;2

Coman, M., Griffiths, R. & Hughes, G. (2006). Sandström's experiments revisited. Journal of Marine Research. 64. 783-796.

Cusack, J. M., Brearley, J. A., Naveira-Garabato, A. C., Smeed, D. A., Polzin, K. L., Velzeboer, N. & Shakespeare, C. J. (2020), Observed Eddy-Internal Wave Interactions in the Southern Ocean. *Journal of Physical Oceanography, 50*, 3043-3062.

Danabasoglu, G., Yeager, S. G., Kwon, Y., Tribbia, J. J., Phillips, A. S. & Hurrell, J. W. (2012), Variability of the Atlantic meridional overturning circulation in CCSM4. *Journal of Climate*, 25, 5153-5172

D'Asaro, E. A. (1985), The energy flux from the wind to near-inertial motion in the surface of the mixed layer. *Journal of Physical Oceanography*, 15, 1043-1059.

de Boyer Montégut, C., Madec, G., Fischer, *A. S.,* Lazar, *A.,* & Iudicone, D. (2004), Mixed layer depth over the global ocean: An examination of profile data and a profile-based climatology, *Journal of Geophysical Research, 109, C12003. doi:*10.1029/2004JC002378.

de Lavergne, C., Palter, J., Galbraith, E., Bernardello, R. & Marinov, I. (2014), Cessation of deep convection in the open Southern Ocean under anthropogenic climate change. *Nature Climate Change* 4, 278–282. https://doi.org/10.1038/nclimate2132

Dong, S., Gille, T. S., & Sprintall J. (2007), An assessment of the Southern Ocean mixed layer heat budget. *Journal of Climate*, *20*(17), 4425–4442. doi:10.1175/JCLI4259.1

Du Plessis, M., Swart, S., Ansorge, I. J., Mahadevan, A., & Thompson, A. F. (2019), Southern Ocean Seasonal Restratification Delayed by Submesoscale Wind-Front Interactions, *Journal of Physical Oceanography, 49*, 1035-1053. doi:10.1175/JPO-D-18-0136.1

Ferreira Azevedo, M., Aoki, S. & Kitade, Y. (2022), Seasonal variation and governing dynamics of the mixed layer in the Indian sector of the Southern Ocean. *Journal of Geophysical Research: Oceans,* 127, e202IJC017838.

Ferreira Azevedo, M., & Aoki, S. (2022b), *mTRITON Mooring data of KARE-17* (1.00) [Dataset]. Arctic Data archive System (ADS), Japan, https://ads.nipr.ac.jp/dataset/A20220225-001

Ferreira Azevedo, M., & Aoki, S. (2022c), *CTD casts data of KARE-17* (1.00) [Dataset]. Arctic Data archive System (ADS), Japan, https://ads.nipr.ac.jp/dataset/A20220225-002

Gargett, A. E. (1984), Vertical eddy diffusivity in the ocean interior. *Journal of Marine Research, 42*, 359–393. doi:10.1357/002224084788502756

Garwood, R.W. (1991), Enhancements to deep turbulent entrainment, Deep Convection and Deep Water Formation in the Oceans, Elsevier Oceanography Series, 57, 197-213, doi:10.1016/S0422-9894(08)70068-0

Gerkema, T., Zimmerman, J. T. F., Maas, L. R. M. & van Haren, H. (2008), Geophysical and astrophysical fluid dynamics beyond the traditional approximation. *Journal of Fluid Mechanics*, 529, 195-219.

Gerkema, T. & Exarchou, E. (2008), Internal-wave properties in weakly stratified layers. *Journal of Marine Research*, 66, 617-644. https://doi.org/10.1357/002224008787536817

Gregg, M. C. (1988), Mixing in the Thermohaline Staircase East of Barbados. In: *Small-Scale Turbulence and Mixing in the Ocean: Proceedings of the 19th International Liege Colloquium on Ocean Hydrodynamics*, 46, 453-470. https://doi.org/10.1016/S0422-9894(08)70564-6

Grimshaw, R. (1975). Nonlinear internal gravity waves and their interaction with the mean wind. *Journal of the Atmospheric Sciences*, 42, 1779-1793

Hersbach, H., Bell, B., Berrisford, P., Hirahara, S., Horányi A., & Muñoz-Sabater J., et al. (2018), *ERA5 hourly data on single levels from 1979 to present* (Accessed on 09-Feb-2021) [Dataset]. Copernicus Climate Change Service (C3S) Climate Data Store (CDS). doi:10.24381/cds.adbb2d47

Heuzé, C., Ridley, J. K., Calvert, D., Stevens, D. P. and Heywood, K. J. (2015), Increasing vertical mixing to reduce Southern Ocean deep convection in NEMO3.4. *Geoscience Model Development,* **8,** 3119-3130.

Hirano, D., Kitade, Y., Nagashima, H., & Matsuyama, M. (2010), Characteristics of observed turbulent mixing across the Antarctic slope front at 140E, East Antarctica. *Journal of Oceanography*, *66*, 95–104. doi:10.1007/s10872-010-0008-x

Hirano, D., Tamura, T., Kusahara, K., Ohshima, I. K., Nichills, W. K., & Ushio, S., et al. (2020), Strong ice-ocean interaction beneath Shirase Glacier Tongue in East Antarctica*. Nature Communications*, *11*, 4221. doi:s41467-020-17527-4

Hogg, A. M., Spence, P., Saenko, O. A., & Downes, S. M. (2017), The energetics of Southern Ocean upwelling. *Journal of Physical Oceanography*, *47*(1), 135–153. doi:10.1175/JPO-D-16-0176.1

Ishihara, Y., & Mizuno K. (2010), JAMSTEC'S m-TRITON: Surface High-Speed Data Transmission. *ARGOS Forum*, 69, 10.

Jena, B., Ravichandran, M. & Turner, J. (2019). Recent reocurrence of large open-ocean polynya on the Maud Rise Seamount. *Geophysical Research Letters*, 46**,** 4320-4329.

Johannessen, O. M., Sandven, S., Johannessen, J. A. (1991), Eddy-Related Winter Convection in the Boreas Basin, Elsevier Oceanography Series, 57, 85-105. https://doi.org/10.1016/S0422-9894(08)70062-X

Johannessen, O.M., Lygre, K., Eldevik, T. (2013), Convective chimneys and plumes in the northern Greenland Sea. *The Nordic Seas: An Integrated Perspective*, American Geophysical Union (AGU), pp. 251-272, 10.1029/158GM17

Johnston, T. M. S., & Rudnick D. L. (2009), Observations of the transition layer. *Journal of Physical Oceanography*, *39*(3), 780–797. doi:10.1175/2008jpo3824.1

Jones, H. & Marshall, J. (1993), Convection with Rotation in a Neutral Ocean: A Study of Open-Ocean Deep Convection. *Journal of Physical Oceanography*, 23, 1009-1039. https://doi.org/10.1175/1520-0485(1993)023<1009:CWRIAN>2.0.CO;2

Kelley, E. D. (1990), Fluxes through diffusive staircases: A new formulation. *Journal of Geophysical Research*, *95*(C3), 3365–3371. doi:10.1029/JC095iC03p03365

Kennicutt, M., Chown, S., & Cassano, J. Polar research: Six priorities for Antarctic science. Nature 512, 23–25 (2014). https://doi.org/10.1038/512023a

Kilbourne, B. F., & Girton, J. B. (2015), Surface boundary layer evolution and near-inertial wind power input. *Journal of Geophysical Research: Oceans, 120*, 7506-7520. doi: 10.1002/2015JC011213

Killworth P.D. (1979), On 'chimney' formations in the ocean. *Journal of Physical Oceanography*, 9, 531-554. https://doi.org/10.1175/1520-0485(1979)009<0531:OFITO>2.0.CO;2

Klinger, B. A., Marshall, J. & Send, U. (1996), Representation of convective plumes by vertical adjustment. *Journal of Geophysical Research Oceans*, 101, 18175-18182. https://doi.org/10.1029/96JC00861

Klostermeyer, J. (1991). Two- and three-dimensional parametric instabilities in finite-amplitude internal gravity waves. *Geophysical & Astrpphysical Fluid Dynamics,* 61, 1-25.

Kostov, Y., Armour, K. C. & Marshall, J. (2014), Impact of the Atlantic meridional overturning circulation on ocean heat storage and transient climate change. *Geophysical Research Letters*, 41, 2108-2116. https://doi.org/10.1002/2013GL058998

Kovalevsky, D.V., Bashmachnikov, I.L. & Alekseev, G.V. (2020), Formation and decay of a deep convective chimney, *Ocean Modeling*, 148, 101583, doi:10.1016/j.ocemod.2020.101583

Kuhlbrodt, T. (2008). On Sandstrom's inferences from his tank experiments: a hundred years later. *Tellus A: Dynamic Meteorology and Oceanography*, 60, 819-836.https://doi.org/10.1111/j.1600-0870.2008.00357.x

Kurtakoti, P., Veneziani, M., Stossel, A. & Weijer, W. Preconditioning and formation of Maud Rise polynyas in a high-resolution Earth system model. *J. Climate*, **31,** 9659-9678 (2018).

LeBlond, P. H., Mysak, L. A. (1978), Waves in the ocean. Elsevier. Journal of Fluid Mechanics, 90(2), 398-400. http://doi.org/10.1017/S002211207923228X

Ledwell, J. R., A. J. Watson, and C. S. Law (1993), Evidence for slow mixing across the pycnocline from an open ocean tracer release experiment, *Nature*, 364(6439), 701–703, https://doi.org/10.1038/364701a0

Ledwell, J. R., A. J. Watson, and C. S. Law (1998), Mixing of a tracer in the pycnocline, *Journal of Geophysical Research*, 103(C10), 21499–21529. https://doi.org/10.1029/98JC01738

Lilly, J. M. & Olhede, S. C. (2012), Generalized Morse wavelets as a superfamily of analytic wavelets. *IEEE Trans. Signal Process.*, 60, 6036-6041.

Lilly, J., M. jLab: A data analysis package for matlab, v.1.7.1, http://www/jmlilly.net/software (2021).

Lombard, P., N., Riley, J., J. (1996). Instability and breakdown of internal gravity waves. I. Linear stability analysis. *Physics of Fluids*, 8, 3271

Lumpkin, R. & Speer, K. (2007), Global Ocean Meridional Overturning. *Journal of Physical Oceanography,* 37, 2550-2562.

Marshall, J. & Schott, F. (1999), Open-ocean convection: Observations, theory, and models. *Reviews of Geophysics*, 37, 1-64.

Maxworthy, T. & Narimousa, S. (1992). Rotating Convection. In: Davis, S.H., Huppert, H.E., Müller, U., Worster, M.G. (eds) Interactive Dynamics of Convection and Solidification. NATO ASI Series, vol 219. Springer, Dordrecht. https://doi.org/10.1007/978-94-011-2809-4_41

Meyer, A., Sloyan, B. M., Polzin, K. L., Phillips, H. E., & Bindoff, N. L. (2015), Mixing variability in the Southern Ocean. *Journal of Physical Oceanography*, *45*(4), 966–987. doi:10.1175/JPO-D-14-0110.1

Meyer, C., Kreft, H., Guralnick, R. & Jetz, W. (2015), Global priorities for an effective information basis of biodiversity distributions. Nature Communications, 6, 8221. https://doi.org/10.1038/ncomms9221

Mikolajewicz, U., Sein, D.V., Jacob, D., Königk, T., Podzun, R., Semmler, T. (2005), Simulating Arctic sea ice variability with a coupled regional atmosphere-ocean-sea ice model. *Meteorolische Zeitschrift*, 14, 793-800.

Mizobata, K., Shimada, K., Aoki, S., & Kitade Y. (2020), The cyclonic eddy train in the Indian Ocean sector of the Southern Ocean as revealed by satellite radar altimeters and in situ measurements. *Journal of Geophysical Research: Oceans*, *125*, e2019JC015994. doi:10.1029/2019JC015994

Monterey, G. I., & Levitus, S. (1997). Seasonal variability of mixed layer depth for the world ocean, NOAA NESDIS Atlas 14,100. *Natl. Oceanic and Atmos. Admin., Silver Spring, MD*.

Moore G.W.K., Våge, K., Pickart, R.S., Renfrew, I.A. (2015), Decreasing intensity of open-ocean convection in the Greenland and Iceland seas**.** *Nature Climate Change*, 5 (9), p. 877, doi:10.1038/nclimate2688

Munk, W. H. (1966), *Abyssal recipes. Deep-Sea Research and Oceanographic Abstracts*, 13, 707-730. https://doi.org/10.1016/0011-7471(66)90602-4

Munk, W. & Wunsch, C. (1998) Abyssal Recipes II: Energetics of Tidal and Wind Mixing. *Deep Sea Research Part I: Oceanographic Research Papers*, 45, 1977-2010. https://doi.org/10.1016/S0967-0637(98)00070-3

Nagurnyi, A.P., Bogorodskii, P.V., Popov, A.V., Svyashchennikov, P.N. (1985), Intense formation of cold bottom waters on the Greenland Sea surface Trans. (Doklady) USSR Academy of Sciences, 284 (2), p. 478

Naveira Garabato, A. C., K. L. Polzin, B. A. King, K. J. Heywood, & M. Visbeck (2004), Widespread intense turbulent mixing in the Southern Ocean, Science, 303, 210 – 213.

Neelin, J.D., Dijkstra, H.A. (1995), Ocean-atmosphere interaction and the tropical climatology. Part I: The dangers of flux correction. *Journal of Climate*, 8, 1325-1342. doi:10.1175/1520-0442

Nikurashin, M. & Ferrari, R. (2013), Overturning circulation driven by breaking internal waves in the deep ocean, Geophysical Research Letters, 40, 3133–3137, https://doi.org/10.1002/grl.50542.

Newman, L., Heil, P., Trebilco, R., Katsumata, K., Constable, A., & van Wijk, E., et al. (2019), Delivering sustained, coordinated and integrated observations of the Southern Ocean for global impact. *Frontiers in Marine Science*, 6, 433. doi:10.3389/fmars.2019.00433

Ohshima, K. I., Fukamachi, Y., Williams, G. D., Nihashi, S., Roquet, F., Kitade, Y., et al. (2013), Antarctic Bottom Water production by intense sea-ice formation in the Cape Darnley polynya, *Nature Geoscience*, *6*, 235–240. doi:10.1038/ngeo1738

Orsi A. H., Whitworth III., T., & Nowlin Jr., W. D. (1995), On the meridional extent and fronts of the Antarctic Circumpolar Current. *Deep Sea Research Part I: Oceanographic research papers*, *42*, 641–673. doi:10.1016/0967-0637(95)00021-W

Percival D. B., & Walden A. T. (1993), Spectral analysis for physical applications: Multitaper and conventional univariate techniques. Cambridge: Cambridge University Press.

Polard, R. T. & Millard, R. C. Comparison between observed and simulated wind-generated inertial oscillations. *Deep Sea Research and Oceanographic Abstracts,* 17, 813-816 https://doi.org/10.1016/0011-7471(70)90043-4

Rahmstorf, S. (1993), A fast and complete convection scheme for ocean models. *Ocean Modelling*, 101, 9-11.

Rintoul, S. R. (1998), On the origin and influence of Adélie Land Bottom Water in Ocean. In Ocean, Ice, and Atmosphere: Interactions at the Antarctic Continental Margin (eds Jacobs, S. S. & Weiss, R. F.). doi:10.1029/AR075p0151

Rintoul, S. R., Sparrow, M., Meredith, M. P., Wadley, V., Speer, K., Hofmann E., et al. (2012), The Southern Ocean observing system: Initial science and implementation strategy. Cambridge: SCAR.

Sallée, J. B., Matear, R. J., Rintoul, S. R. & Lenton, A. (2012), Localized subduction of anthropogenic carbon dioxide in the Southern Hemisphere oceans, *Nature Geoscience*, 5, 579–584, *doi:*10.1038/ngeo1523.

Schulz, E. W., Josey, S. A., & Verein, R. (2012), First air-sea flux mooring measurements in the Southern Ocean. *Geophysical Research Letters*, *39*, L16606. doi:10.1029/2012GL052290

Scinocca, J. F., & Shepherd, T. G. (1992). Nonlinear wave-activity conservation laws and Hamiltonian structure for the two-dimensional anelastic equations. *Journal of Atmospheric Sciences*, 49(1), 5-28. https://doi.org/10.1175/1520-0469(1992)049%3C0005:NWACLA%3E2.0.CO;2

Scott, J. R., Marotzke, J., Stone, P.H. (1999). Interhemispheric thermohaline circulation in a coupled box model. *Journal of Physical Oceanography*, 29, 351-365, doi:10.1175/1520-0485

Sevellec, I., Naveira-Garabato, A. C., Brearley, J. A. & Shee, K. L. (2015), Vertical flow in the Southern Ocean estimated from individual moorings. *Journal of Physical Oceanography*, 45, 2209-2220.

Shimada, K., Aoki, S., & Ohshima, K. I. (2017), Creation of a gridded dataset for the Southern Ocean with a topographic constraint scheme. *Journal of Atmospheric and Oceanic Technology*, *34*(3), 511–532. doi:10.1175/JTECH-D-16-0075.1

Shimada, K., Kitade, Y., Aoki, S., Mizobata, K., Cheng, L., Takahashi, K. T., Makabe, R., Kanda, J. & Odate, T. (2022). Shoaling of abyssal ventilation in the Eastern Indian Sector of the Southern Ocean. *Communications Earth & Environment,* 3, 120. https://doi.org/10.1038/s43247-022-00445-2

Schmittner, A., Oschlies, A., Giraud, X., Eby, M. & Simmons, H. L. (2005), A global model of the marine ecosystem for long-term simulations: Sensitivity to ocean mixing, buoyancy forcing, particle sinking, and dissolved organic matter cycling. *Global Biogeochemical Cycles*, 19, GB3004. http://doi.org/10.1029/2004GB002283

Skinner, L., Menviel, L., Broadfield, L., Gottschalk, J., Greaves, M. (2020), Southern Ocean convection amplified past Antarctic warming and atmospheric CO_2 rise during Heinrich Stadial 4. *Communications Earth & Environment,* 1, 23. https://doi.org/10.1038/s43247-020-00024-3

Sloyan, B. M. (2005), Spatial. variability of mixing in the Southern Ocean, Geophysical Research Letters,32, L18603, https://doi.org/10.1029/2005GL023568

Smith, S. R., Hughes, P. J., & Bourassa, M. A. (2011), A comparison of nine monthly air-sea flux products. *International Journal of Climatology*, *31*, 1002–1027. doi:10.1002/joc.2225

Sohail, T., Gayen, B. and McC.Hogg, A. (2020), The dynamics of mixed layer deepening during open-Ocean convection. *Journal of Physical Oceanography*, 50**,** 1625-1641

Sokolov, S., & Rintoul, S. R. (2002), Structure of Southern Ocean fronts at 140E. *Journal of Marine Systems*, *37*(1–3), 151–184. doi:10.1016/S0924-7963(02)00200-2

Soloviev, A. & Klinger, B. Open Ocean convection. *Encyclopedia of Ocean Sciences*. 218-225 (Academic Press, San Diego, 2008).

Stommel, H. (1961),Thermohaline convection with two stable regimes of flow. *Tellus*, 13, 224-230, doi:10.1111/j.2153-3490.1961.tb00079.x

Stommel H.M., Young W.R. (1993), The average T-S relation of a stochastically forced box model. *Journal of Physical Oceanography*, 23, 151-158, 10.1175/1520-0485(1993)023¡0151:TAROAS¿2.0.CO;2

Sutherland, B., R. (1996). Internal gravity wave radiation into weakly stratified fluid. *Physics of Fluids*, 8, 430-441

Sutherland, B., R. (2001). Finite-amplitude internal wavepacket dispersion and breaking. *Journal of Fluid Mechanics*, 429, 343-380

Sutherland, B. R. (2005), Internal Wave Propagation, *Modern Applied Mathematics* Ed. J. C. Misra, Narosa Press, New Delhi, *372-422*

Taburet, G., Sanchez-Roman, A., Ballarotta, M., Pujol, M-I., Legeais, J-F., Fournier, et al. (2019), DUACS DT2018: 25 years of reprocessed sea level altimetry products. *Ocean Science, 15*, 1207-1224, doi:10.5194/os-15-1207-2019

Talley, L. D. (1999), Some aspects of ocean heat transport by the shallow, intermediate and deep overturning circulations. *Mechanisms of Global Climate Change at Millennial Time Scales,* 112, 1-22.

Talley, L.D., Pickard G.L., Emery W.J., Swift J.H., *(*2011). Descriptive Physical Oceanography: An Introduction (Sixth Edition), Elsevier, Boston, 560 pp.

Tamura, K. T., Ohshima, K. I., & Nihashi, S. (2008). Mapping of sea ice production for Antarctic coastal Polynyas*. Geophysical Research Letters*, *35*, L07606. doi:10.1029/2007GL032903

Tamura, T., Williams, G. D., Fraser, A. D., & Ohshima, K. I. (2012), Potential regime shift in decreased sea ice production after the Mertz Glacier calving. *Nature Communications*, *3*, 826. doi:10.1038/ncomms1820

Thomson, D. J. (1982), Spectrum estimation and harmonic analysis. *Proceedings of the IEEE*, *70*(9), 1055–1096. doi:10.1109/PROC.1982.12433

Trenberth, K. E., Olson, J. G., & Large, W. G. (1989), A global ocean wind stress climatology based on ECMWF analyses. NCAR Technical Note, NCAR/TN-388+STR, 95. University Corporation for Atmospheric Research. doi:10.5065/D6ST7MR9

Toggweiler, J.R. & Samuels, B. (1993). New Radiocarbon Constraints on the Upwelling of Abyssal Water to the Ocean's Surface. In: Heimann, M. (eds) The Global Carbon Cycle. NATO ASI Series, vol 15. Springer, Berlin, Heidelberg. https://doi.org/10.1007/978-3-642-84608-3_14

Toggweiler, J. R. & Samuels, B. (1995) Effect of Drake Passage on the global thermohaline circulation. *Deep-Sea Research*, 42, 477-500. https://doi.org/10.1016/0967-0637(95)00012-U

Toggweiler, J. R. & B. Samuels, 1998: On the ocean's large-scale circulation near the limit of no vertical mixing. J. Phys. Oceanogr., 28, 1832-1852.

https://doi.org/10.1175/1520-0485(1998)028%3C1832:OTOSLS%3E2.0.CO;2

United Nations. (1959, Dec. 01) *The Antarctic Treaty* (402, UNTS 71). https://documents.ats.aq/recatt/att005_e.pdf

Visbeck, M. (2007), Power of pull. *Nature*, 447, 383, doi:10.1038/447383a

Vreugdenhil, C. A., Gayen, B. (2021), Ocean Convection. *Fluids,* 6, 360. doi: 10.3390/fluids6100360

Waterman, S., Naveira-Garabato, A. C., Polzin, K. L. (2013), Internal Waves and Turbulence in the Antarctic Circumpolar Current. *Journal of Physical Oceanography,* 43, 259-282.

Whitt, D. B. & Thomas, L. N. (2015). Resonant Generation and Energetics of Wind-Forced Near-Inertial Motions in a Geostrophic Flow. *Journal of Physical Oceanography*, 45, 181-208. doi: 10.1175/JPO-D-14-0168.1

Williams, G. D., Aoki, S., Jacobs, S. S., Rintoul, S. R., Tamura, T., & Bindoff, N. L. (2010), Antarctic Bottom Water production along the Adélie and George V Land coast, East Antarctica (140-149°E). *Journal of Geophysical Research*, *115*, C04027. doi:10.1029/2009JC005812

Williams, G. D., Herraiz-Borreguero, L., Roquet, F., Tamura, T., Ohshima, K. I., & Fukamachi, Y., et al. (2016), The suppression of Antarctic bottom water formation by melting ice shelves in Prydz Bay. *Nature Communications*, *7*, 12577. doi:10.1038/ncomms12577

Wunsch, C. & Ferrari, R. (2004), Vertical mixing, energy, and the general circulation of the oceans. *Annual Review of Fluid Mechanics*, *36*, 281–314. doi:10.1146/annurev.fluid.36.050802.122121

Yu, L., Zhang, Z., Zhong, S., Zhou, M., Gao, Z., Wu, H., & Sun, B. (2011), An inter-comparison of six latent and sensible heat flux products over the Southern Ocean, *Polar Research*, *30*, 10167. doi:10.3402/polar.v30i0.10167

Zhang, J., Schmitt, R. W., & Huang R. X. (1998), Sensitivity of the GFDL Modular Ocean Model to Parameterization of Double-Diffusive Processes. *Journal of Physical Oceanography*, *28*(4), 589–605. doi:1520-0485(1998)028<0589:SOTGMO>2.0.CO;2

Zickfeld, K., Slawig, T., Rahmstorf, S. (2004), A low-order model for the response of the Atlantic thermohaline circulation to climate change. Ocean Dynamics, 54, 8-26. doi:10.1007/s10236-003-0054-7

Zika, J. D., Sloyan, B. M., McDougall, T. J. (2009), Diagnosing the Southern Ocean Overturning from Tracer Fields. *Journal of Physical Oceanography,* 39, 2926-2940